Perovskites for Nonlinear Optics

Naseem Alsaif

Supervisor: Prof. Noel Healy

School of Mathematics, Statistics and Physics
Newcastle University

This dissertation is submitted for the degree of
Doctor of Philosophy

Physics Month Year

Abstract

Nonlinear optics has been an important field since the invention of the laser and has enabled many advanced technologies, such as telecommunications, quantum technologies and super-resolution imaging. Nonlinear optical effects rely on the characteristic nonlinear response of a material and it is important to identify materials with the right properties for the right applications. Hybrid inorganic-organic perovksites have seen huge successes in the developments of photovoltaic, light emission and detection in the last decade. Their strength as a material for nonlinear optics, particularly in the third-order regime, has been the subject of recent investigation. However, the origin of nonlinearity of these hybrid perovksites remains unclear. In this work, the influence of anion on the nonlinear response of methylammonium lead halides ($MAPbX_3$) was investigated. It is shown that an anion with a larger size leads to a stronger nonlinear response for the same family of materials.

Although hybrid perovskites show strong nonlinear responses, they typically contain lead (Pb), which is toxic and not environmental friendly. Also, these materials possess bandgaps in the visible region, which is excellent for solar applications but could be a disadvantage for nonlinear applications because of the high two-photon absorption. Therefore, it is interesting to investigate materials with strong nonlinear responses and wide bandgaps, while also being environmentally friendly. Metal-free perovskites appear to be excellent alternatives. While this family of materials was originally designed for the interest of ferroelectric applications, there have been works demonstrating their potential in nonlinear applications, for instance, second harmonic generation. In this work, the examination of perovskite for nonlinear optics is extended to include the metal-free material DABCO-NH3-X_3 and MDABCO-NH3-X_3. All of these metal-free perovskites possess bandgaps of about 5 eV, which is significantly higher than that of their hybrid counterparts. The MDABCO-NH3-X_3 variants demonstrated a nonlinear optical response that was an order of magnitude greater than the DABCO-NH3-X_3 materials. It is believed that the introduction of methyl-group induces distortion of the octahedral, which leads to a stronger nonlinear response. A typical way to exploit the third-order nonlinear response of materials is using waveguides, in which the response can be enhanced due to the length of the material. $MAPbBr_3$ and MDABCO-NH_3-I_3 crystals have been grown inside capillaries, in an attempt to form the first generation of optical fibre-like perovskite waveguides. While the transmission losses were quite high at $10\,\mathrm{dB\,cm^{-1}}$, it is noted that this is commensurate with the first generation of semiconductor optical fibres and provides a strong platform for waveguiding perovskite nonlinear optics.

The thesis is dedicated to God Almighty, my creator, my source of strength and my patient especially when my children were away from me throughout this program.

As part of my dissertation, I dedicate it to my family. There is a special feeling of gratitude in my heart for my parents, whose words of encouragement and push for tenacity have inspired me. The support I have received from my brothers and sisters has been invaluable during the difficult PhD period and in general.

In addition, I dedicate this work to my husband, Ali Mobarki, who has encouraged me all the way and ensured that I put everything I have into the work I have begun. My children, Lana and Essa, have suffered greatly from this quest. I am grateful for your help and thank you for being so kind and loving to me.

Last but not least, this thesis is dedicated to my brother Ali Alsaif who passed away. His death occurred before I was awarded my PhD. Although we are not together, I keep you in my thoughts all the time, even when you are not present. Despite the shortness of your life, I will remember you forever. You will always be in my heart. God bless you.

Declaration

I hereby declare that except where specific reference is made to the work of others, the contents of this dissertation are original and have not been submitted in whole or in part for consideration for any other degree or qualification in this, or any other university. This dissertation is my own work and contains nothing which is the outcome of work done in collaboration with others, except as specified in the text and Acknowledgements. This dissertation contains fewer than 65,000 words including appendices, bibliography, footnotes, tables and equations and has fewer than 150 figures.

Naseem Alsaif
Month Year

Acknowledgements

Based on work done at Newcastle University, Perovskite Lab (3.26, Bedson building) and Photonics Lab (E4.21F, Merz court building), this thesis describes the results of the research conducted between September 2019 and September 2022. Success in my life has mainly been thanks to Allah, who eases my work as a PhD student and in my personal life- for which I am extremely thankful. In particular, I would like to express my gratitude to Prof. Noel Healy and Dr Hei Tsui for the excellent supervision, support, advice, and guidance that they provided to me throughout the course of my PhD. Without them, this work would not be possible. My deepest gratitude goes out to my parents, my father Mr. Hamoud Alsaif and my mother Mrs. Zahab Madkhali for the advice and understanding they have provided to me in the all years I have been working on my PhD and taking care of my children. My husband, Mr. Ali Mobarki and my kids, Lana and Essa, are also to be thanked for this. The support I received from them was also greatly appreciated. They encouraged me, helped me, and they cared for me, gently and lovingly. Also, I want to thank my brothers, especially my brother Ali who passed away before I completed my PhD as well as Abdu Alrahman, who was the first to suggest I accept the Saudi Arabian scholarship to study abroad. I am so grateful for my sisters' support and encouragement that there are no words to express what I feel. It is my privilege to express my gratitude to the Jazan University for the funding that has enabled me to pursue my studies at the Department of Mathematics, Statistics, and Physics, University of Newcastle. My dissertation would not have been possible without the encouragement and support I received from my friends throughout my studies. A special thanks goes out to my lab mates and research group for a wonderful time spent together in the lab.

Table of Contents

List of Figures

List of Tables

Chapter 1. Introduction

1.1. introduction

Hybrid halide perovskites have attracted a lot of attention in recent years because of their outstanding performance in photovoltaic, photodetectors, light emitting and laser applications [10] [11] [12] [13] [14]. One distinct advantage of perovskites is their tunable optoelectornic properties. This can be done by modifying the combinations of various cations and anions while retaining the characteristic ABX_3 structure, where typically A is a monovalent cation, B a divalent metal and X a halide. Apart from the success in the linear regime, there has been a growing interest in the field of nonlinear optics. Nonlinear optics is the study of light-matter interactions under high light intensity. Second-order nonlinear effects include second harmonic generation and three-wave mixing while optical Kerr effect and two-photon absorption belongs to the third-order category. The distinction between second-order and third-order nonlinear optical effects is that second-order only occur in non-centrosymmetric structures while third-order can be found in all types of materials. These nonlinear effects have been employed in various technologies, including laser, all-optical switching, and optical limiting. Although several studies have demonstrated strong nonlinear response in hybrid perovskites, [15] [16] [17] [18] [19] [20] [21] there are issues when applying these materials in nonlinear optics. Specifically, the narrow band gap of hybrid perovskites (1.5 - 3 eV) [22] leads to high optical absorption, which restricts their uses in visible and UV regions. A narrow band gap also means a low laser damage threshold, which limits their practicality in nonlinear optics as high intensity light is typically required to operate in this regime.

Another issue with the hybrid perovskite materials is that they are typically lead-based, which is toxic and non-environmental friendly. Therefore, it is reasonable to also look for alternative materials that mitigate such problems.

One potential replacement for hybrid perovskites is metal-free perovskites. This family of materials was first discovered by Ye *et al.* [23]. The metal-free perovskites also have the ABX_3 configuration, only the B site is occupied by NH_4 in this case. For the A site, many organic molecules have been identified to be suitable in the perovskite framework, [23] with the interests in DABCO (*N*-*N*′- diazabicyclo[2.2.2] octonium, $C_6H_{12}N_2$) and its derivative Methyl-DABCO (*N*-methyl-*N*′- diazabicyclo[2.2.2] octonium, $C_7H_{15}N_2$) the highest. To further simplify their long compound names, DNX and MDNX, where X is the halide (I, Br, Cl), will be used to represent DABCO-NH_4X_3 and Methyl-DABCO-NH_4X_3 respectively in the rest of this Thesis. Various aspects of the metal-free perovskites have been studied
[24] [25] [26] [27] [28] [29] [30] [31] and theoretical calculations have predicted these materials possess wide band gaps [32]. Metal-free perovskites pose as a solution to the narrow band gap and toxic issues of hybrid perovskites that limit thier use in NLO.

1.2. Aims and Objectives

Photonics is the technology of generating and harnessing light for technologically advanced applications, such as telecommunications and quantum optics. Such applications are ubiquitous. Silicon photonics is an example of a materials platform that is currently revolutionising photonics. It is the application and study of photonic systems that use silicon as an optical medium. This project aims to develop a new field of research; perovskite photonics, with research primarily focusing on optimising the growth of perovskites for nonlinear optics and the first demonstration of waveguide fabrication. The justification for this work is because the perovskite material systems exhibit optical as well as electrical properties that make them an exciting candidate that can be used to generate, guide, and detect light. With these optical and electronic properties, perovskite is regarded as one of the most interesting and important semiconductors, which will continue to be a focus of intense interest within the field of optoelectronics. Perovskite material can be readily deposited as a film and grown into single crystals and that make them amenable to investigating their optical properties. This project is primarily targeted at measuring nonlinear optical properties of metal and metal-free perovskite films as well as perovskite single crystals, including its nonlinear refractive index and

two-photon absorption coefficient, using the z-scan measurement. This will enable the investigation of a new field of optics – waveguiding perovskites.

1.3. Thesis Outline

Chapter 2 of this thesis introduces perovskites materials (metal halide perovskites including perovskites films and single crystals, and metal-free perovskites) and their applications. This chapter also covers a methodology to fabricate of perovskite thin films and single crystals. In addition, this chapter discusses optical nonlinearity in nonlinear optical materials, self-focusing, two-photon absorption (TPA), and techniques to measure nonlinear refraction. The chapter concludes with a discussion of perovskite optical fibres.

Chapter 3 presents the characterization techniques used in this thesis, In addition a review of the z-scan experimental techniques developed to measure nonlinear refractive index and two photon absorption, including a description of the scan experimental setup and its characterization. This chapter also describes the bespoke z-scan instrument that I built and calibrated for the later experimental work in this thesis.

Chapter 4 discusses the nonlinear behavior of metal halide perovskites. Metal halide Perovskite films are discussed structurally and optically in this chapter, along with single crystals. It investigates the nonlinear behaviour of the the three archetypal lead based perovskites and includes a study of the properties in thin film and single crystal form.

Chapter 5 examines the third-order nonlinear optical properties of metal-free perovskites. In addition, it also studies the role of the methyl group in metal-free perovskites for nonlinear optics. It shows that these materials can be easily deposited via single source evaporation, have wide band gaps, and strong nonlinearities.

Chapter 6 discusses how waveguides can be used to exploit third-order nonlinearities in materials. It shows that, MDABCO-NH3-I3 crystals (MDNI) were grown in capillaries to form MDNI-core fibers. The transmission loss of these materials is about 10 dB/cm, so there have been no nonlinear effects observed. $MAPbBr_3$ fibers have also been attempted, but their length is limited to the millimeter range, which is insufficient to measure the loss.

Chapter 2. Background

2.1. Introduction to perovskites

The perovskite crystal structure was first discovered by Gustav Rose in the Ural Mountains of Russia. It was named in honour of Lev Perovski an esteemed mineralogist of that time [33]. Perovskites can be divided into two basic categories: metal oxides perovskite (ABO_3) and halides perovskite (ABX_3), where X = (I, Br, Cl). Perovskites have been found to be of great interest in a number of applications, as their properties make them useful for the design of device applications such as surfaces acoustic wave signal processors, electrochromic, switching, image storage, filtering, and photochromic applications [34]. Some aspects of the metal-halide perovskite family remain challenging, despite their increasing inclusion in advanced optoelectronic applications (Figure 2.1). Halide perovskites are intrinsically unstable. Perovskites made of halide may undergo chemical and structural changes as a result of humidity [35, 36]. Such instabilities can also degrade device performance over time [37]. Lead is another factor that should be considered when dealing with halide perovskites [38]. Lead is a highly toxic metal with an array of detrimental health effects. In the long run, these toxins can cause irreversible damage to the brain and nervous system when they accumulate in the body for an extended period. Pregnant women and children are particularly susceptible. It is a well-known fact that excessive exposure to lead can even result in death [37]. Therefore, replacing lead without compromising the performance of the device is considered a major challenge in perovskite optoelectronics.

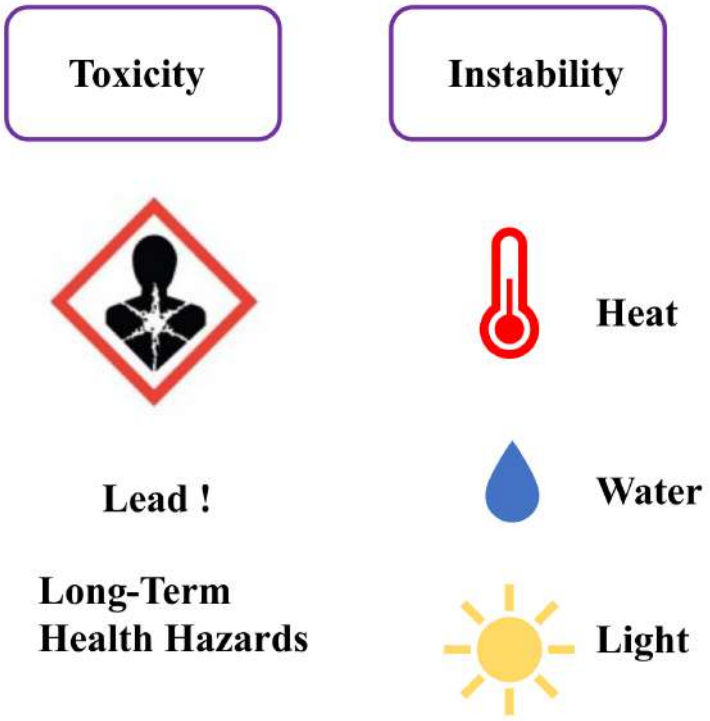

Figure 2.1 A challenge in halide perovskites: adverse effects of lead toxicity and intrinsic instability due to heat, water, and light.

2.2. Metal-halide perovskite

The remarkable optoelectronic properties of metal-halide perovskite materials were discovered in the 1990s when Mitzi et al. demonstrated that they were able to be used to develop thin-film transistors [39, 40] and light-emitting devices (LED). It was later shown that the metal-halide perovskites exhibit attractive electric and optical properties that make them a promising material for solar cells [41]. The halide perovskites can be categorized into two types (i) alkali halide perovskite (ii) organic-inorganic halide perovskite. In alkali halide perovskites, there is a monovalent alkali cation (A) such as Cs, Rb, K, Na, Li, a divalent cation (B) such as (Pb^{2+}, Sn^{2+}, Ge^{2+}), and a halogen anion (X) such as (I^-, Br^-, Cl^- or a mixture). Using organic-inorganic halide perovskites, organic monovalent cations (A) such as ($CH_3NH_3^+$) [1] and cation (B) such as (Pb^{2+}), while X represents anion as (I^-, Br^-, Cl^- or a mixture) [42]. Figure 2.2 shows the typical perovskite lattice structure. Methylammonium lead iodide ($MAPbI_3$) can be viewed as 'the archetypal metal halide perovskite', where the A site is occupied by the organic cation (MA^+), B is occupied by the metal cation Pb^{2+} and X by I^-. At room temperature, $MAPbI_3$ has a black and photoactive tetragonal structure [43]. Indeed the

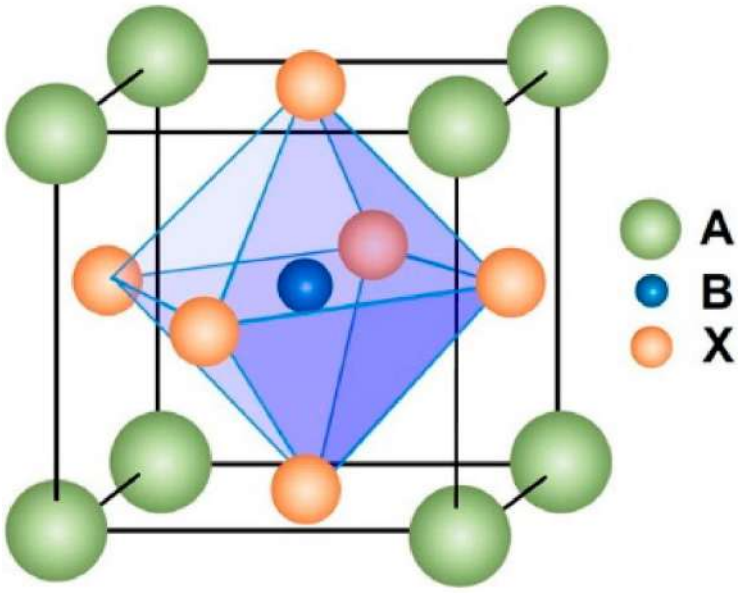

Figure 2.2 The structure of the ABX_3 perovskite shows an octahedral BX_6 [1].

commonly studied perovskite material family is methylammonium lead halide $MAPbX_3$, where X is a halide (I, Br, or Cl). The X-site has the most significant impact on the optical bandgap of $MAPbX_3$, so it is possible to tune its bandgap energy in the range 1.5 to 2.9 eV by partially or completely substituting the halide anion [44]. The transition into a more stable cubic phase arises when smaller-sized Br^- instead of I^- are used. This is also demonstrated by an examination of the crystal structures of $MAPbI_3$ and $MAPbBr_3$, which crystallize in tetragonal and cubic forms, respectively [45].

2.3. Applications of metal-halide perovskites

2.3.1. Solar cells

Perovskite solar cells (PSC) are solar cells where the active absorber and photon-to-electron conversion medium is made with the ABX_3 crystal structure. Metal- halide perovskites materials stand out as the most common compound amongst these light-harvesting active layers, with an efficiency rate starting at 3.6% for $MAPbI_3$ [46]. In 2017, these solar cells became the fastest-advancing solar technology, with an efficiency of 25% with $FAPbI_3$ [47]. Metal-halide perovskite solar cells are particularly attractive for several reasons: strong absorption in the visible spectrum, tunable bandgap, long carrier diffusion lengths, and ease of fabrication. Among the factors that contribute to their success are an easy and low-cost fabrication. Over the

past decade, planar heterojunction solar cells have been tested and developed both in their normal architecture (n-type electron transport layer (ETL) / perovskite / p-type hole transporter (HTL)) as well as in their inverted architecture (HTL / perovskite / ETL) as shown in Figure 2.3.

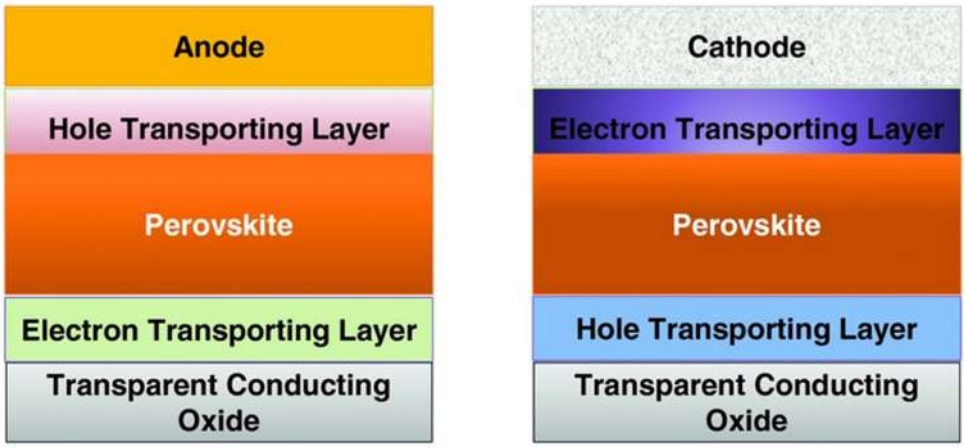

Figure 2.3 Planar vs. inverted heterojunction architectures for perovskite solar cells [2].

2.4. Perovskite film fabrication techniques

Spin-coating involves distributing perovskite solutions onto rotating substrates using centrifugal force [48]. Among the deposition techniques for perovskite thin films, spin-coating is the most popular due to its simplicity and high reliability, as illustrated in Figure 2.4. It is typical for the process to begin by diluting the material in a suitable solvent. This is followed by spreading the solution over the whole surface of the substrate. A high-speed spin is applied to the substrate after spreading the solution. Experiments usually involve depositing a few drops of fluid on a substrate and spinning it at a high speed, usually around 3000 rpm. As a result of centrifugal force, the solution flows out radially. Surface tension and viscous force keep the thin film adhered to the flat substrate. As liquid flows outward and evaporation occurs, thin films are formed. In order to achieve a certain thickness of film, various factors have to be taken into account, including spinning speed, viscosity of solution, spinning time, solution concentration, and surface tension. The spin-coating method is categorized into two categories, namely, one-step spin coating method and two-step spin coating method. Among the main factors that can improve the quality of perovskite films is to control their growth and through controlled post-annealing time.

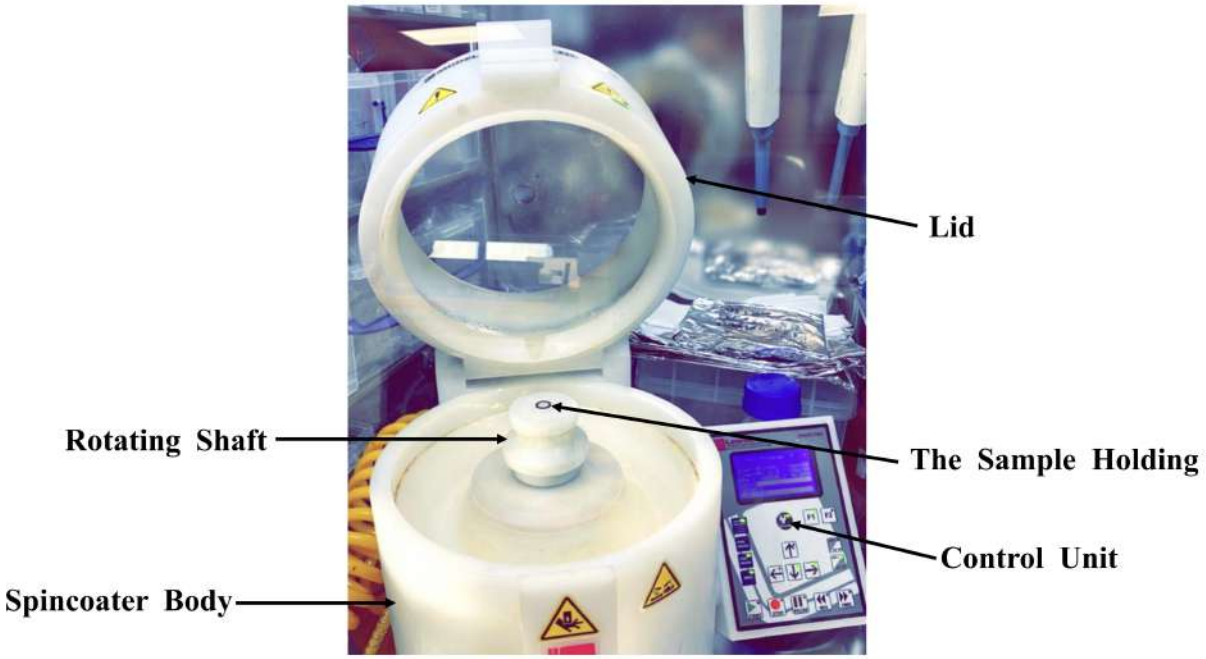

Figure 2.4 A photograph of a spin-coating instrument. The spin-coating process deposits thin films uniformly on flat substrates.

2.4.1. One-step spin coating method

Organic halide salts such as MAX and lead halide salts PbX_2 are mixed and dissolved in a polar solvent like γ-butyrolactone (GBL), N, N-dimethylformamide(DMF), or dimethyl sulfide (DMSO), and isopropanol (IPA) [49, 50], which results in a solution of precursors. All solvents have a high boiling point and a very low vapour pressure at room temperature, making them great solvents to use. Following the spin-coating of the precursor solution over the surface the substrate is annealed. Figure 2.5 illustrates the one-step spin coating method schematic. This method has fewer steps, making it easier to perform, but the resulting layer is not uniform and contains pinholes due to the slow crystallization.

2.4.2. Two-step spin coating method

Organic halides (MAX) and salts of lead halides (PbX_2) are dissolved in polar solvents such as GBL, DMF, DMSO, and IPA. Lead halide solution is spun onto the substrate, and then it is annealed. A spin-coated MAX solution is next deposited on a lead halide surface, followed by an annealing process to obtain the perovskite film. The spinning speed and spinning time are both essential factors during spin-coating of MAX solution over the PbX_2 film [51] in determining the quality of the perovskite layer that is formed. In comparison to the one-step

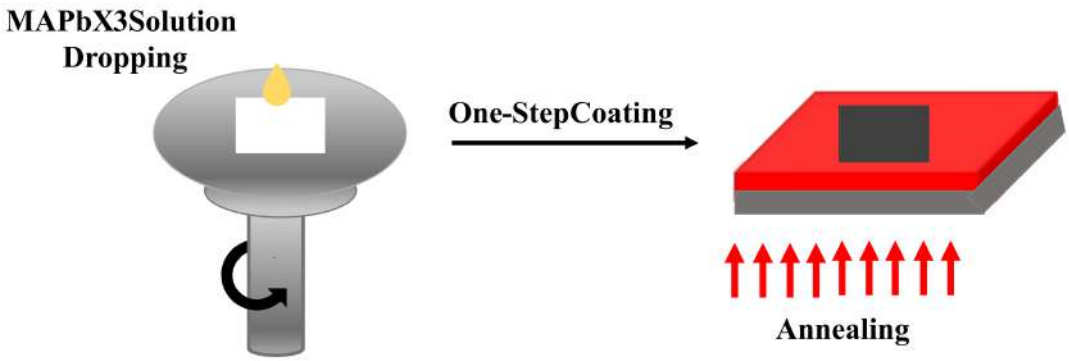

Figure 2.5 Representation of one-step coating method process to prepare perovskitess films.

deposition method, this method produces a better film, but it also has downsides. It is the interrelationship between surface roughness and grain size that poses the primary disadvantage. In conjunction with an increase in grain size, surface roughness will also increase. Figure 2.6 depicts the schematic representation of the two-step spin coating method.

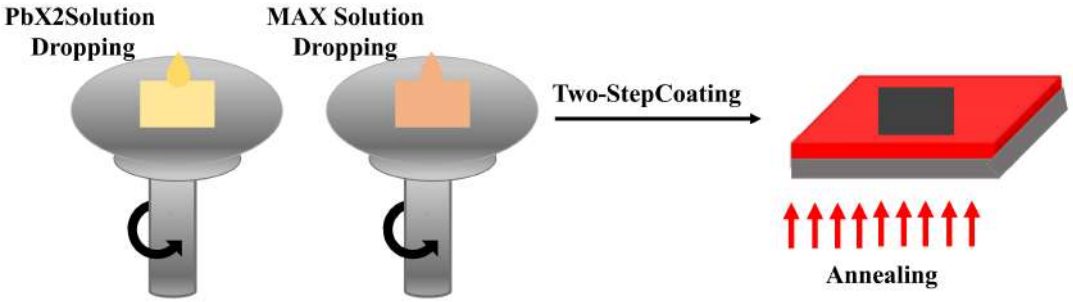

Figure 2.6 Schematic representation of two-step coating procedures for the deposition of $MAPbX_3$ formation film.

The spin-coating method is similar to any other method, since it has both advantages and disadvantages. Its main advantages are that it is effortless and fast. To alter the thickness of the film, it is possible to alter spin coating parameters, such as viscosity, spin time, spin speed, etc. The disadvantage of this method is the amount of material wasted since only $2-5\%$ of materials are used for film production, while the remainder is waste during spinning.

2.4.3. Doctor blade coating

Doctor blade coating is a common technique to produce thin films on large surfaces. With the doctor blade technique, no particular instrument is required. The solution is poured onto the substrate, followed by the swiping of the glass rod at high speed along a linear path as shown in

the schematic diagram Figure 2.7. For a smooth, uniform, and pinhole-free film, it is recommended that the substrate be kept at an elevated temperature during the doctor blade deposition. Heat makes the solvent evaporate faster, which in turn promotes nucleation and crystal growth. This method also has the advantage of allowing the crystallization and thickness of the film to be controlled based on controlling factors such as the concentration of the precursor solution, and the speed of blade movement [52]. Using this technique, low costs can be achieved. In contrast to spin coating techniques, this technique requires considerably less precursor solution [53]. This method has the disadvantage of blade coating quality being inconsistent.

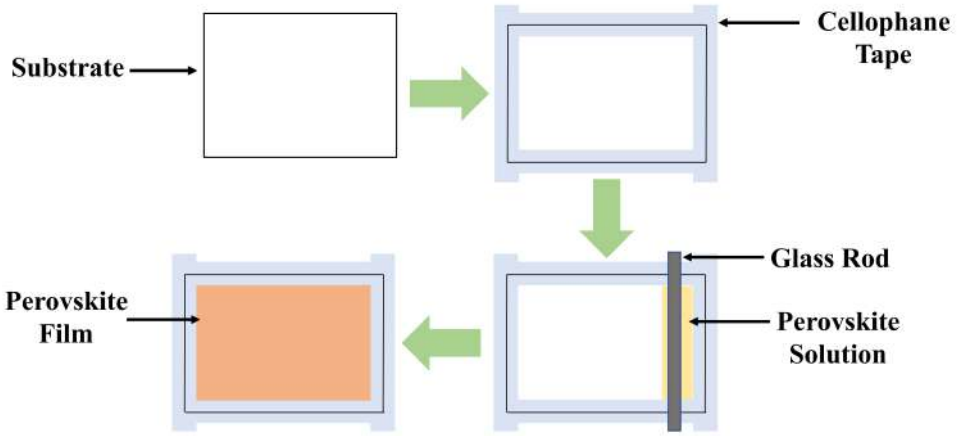

Figure 2.7 Schematic diagram for fabricating perovskites film with doctor blade method.

2.5. Metal-halide perovskites single crystals

The high-performance optoelectronic devices are generally made of lead halide perovskites, which are susceptible to grain boundary defects [54]. It is known that perovskite single crystals have a high carrier lifetime [55] [56] as well as low trap density, which is about 6 orders of magnitude lower than that of polycrystalline perovskites [57]. Having longer carrier diffusion length in single crystals with low trap density and intrinsic grain boundary-free structure, perovskites single crystal offer enhanced environmental stability and can be resulting in a performance boost for optoelectronic devices. These properties of perovskites single crystals will be of great value in advancing our fundamental understanding of their intrinsic properties. There are some methods that were used for growing single crystals of metal halide perovskite, and these methods will be described below.

2.5.1. Metal-halide perovskites single crystal growth

Solution cooling

The solution cooling method is a traditional single crystallization technique. Using a temperature-lowering technique, To grow large single crystals, it is crucial to minimize the number of nuclei. In order to grow large and high-quality single crystals, seed-assisted growth is often used; it entails transferring small crystals to a single crystal precursor and lowering the temperature later. The solution cooling method provides a straight forward and efficient method for growing $MAPbX_3$ as well as $FAPbX_3$ in which the crystals are grown with a decrease in the temperature of the precursor solution. The use of this process is, however, limited due to its high time consumption (typically, it takes two weeks to grow 1 cm sized crystals [58] [59]). Furthermore, for some materials, the rate of the solute solubility in solvents decreases with increasing temperature [60]

Inverse temperature crystallization (ITC) method

Inverse temperature crystallization(ITC) is a method of single crystal crystallization that is strongly dependent on the solution temperature. This is because crystallization takes place via inverse solubility in some organic solvents, so the associated growth process is a balance between dissolution and precipitation. The concentration of free molecules in the solution increases as temperature increases, due to the decrease in bonding energy between molecules in the solution of perovskites. Nucleation and crystal growth occur at some point after the solution reaches supersaturation. At the beginning of the growth process, the surface of the solution is saturated due to the volatilization of the solvent, while the bottom of the solution is unsaturated. Due to convection inside the bottle, as the solvent level drops, the concentration will exceed the solubility of precursors, resulting in the formation of single crystals. This method is suitable to grow single or mixed halide perovskite crystalline materials such as $FAPbX_3$, $MAPbX_3$, and $MA_xFA_{1x}PbI_3$ [61] [62] [63]. Selecting the right solvent is essential for growing highly crystalline single crystals. By simply increasing temperature to induce solution oversaturation, the ITC method provides single crystals in hours. As compared single crystals that are grown using solution cooling typically take a long time to grow and have low yields, which severely

limits their growth rate. Compared to solution cooling, the ITC method is highly effective for growing metal halide perovskites with a much faster growth rate.

Anti-solvent vapor-assisted crystallization (AVC) method

Antisolvent vapor-assisted crystallization (AVC) uses a variety of solvents to produce high-quality crystals based on the solubility of the precursor solution in them [64]. This method involves putting the precursor into a sealed bottle with the antisolvent, and the antisolvent slowly diffuses into the perovskite solution, precipitating crystals [64]. In addition to diffusing anti-solvent, different mixture solvents have different solubilities, influencing crystallization velocity. AVC is a temperature-independent method that allows high-quality crystals to be grown at room temperature, which makes it more suitable for inorganic single crystals like $CsPbX_3$. Unfortunately, the limitations of AVC methods include scalability issues in industry, as well as not as good reproducibility as other methods.

2.6. Perovskites as nonlinear optical materials

The metal-halide perovskites have been found in recent years to be very useful in nonlinear optical applications, particularly their third-order nonlinear response including nonlinear refraction and nonlinear absorption responses, which makes their application to nonlinear optical materials and devices possible [65] [66]. Many reports have described the spectacular nonlinear optical properties of metal- halide perovskites due to their strong light-matter interaction. Table 2.1 shows some nonlinear optical research results for metal- halide perovskites including, their nonlinear refraction and their nonlinear absorption parameters. In this table, wavelengths, pulse durations, and repetition rate frequencies are included since they have an essential influence on the materials' nonlinear refractive and absorption properties. A large dispersion is observed in the nonlinear parameters measured among the different metal-halide perovskite families or even when the same metal-halide perovskite material is measured by more than one author (see table 2.1). Accordingly, the increase in the pulse duration will lead to a greater free charge carrier nonlinearity and a greater thermal nonlinearity; the increase in the repetition rate of the laser may provide an accumulative thermal effect [67]. The very large discrepancy in nonlinear parameter values found in literature is probably a result of not knowing what the

Material	Excitation	n_2 ($m^2 W^{-1}$)	β ($m W^{-1}$)	ref
$MAPbI_3$	40 ps, 530 nm, 10 Hz		-152×10^4	[68]
	40 ns, 532 nm, 1 kHz		-1620 to 22.2 x 10^4	[69]
	40 fs, 800 nm, 1 kHz		0.5×10^4	[70]
	100 fs, 800 nm, 1 kHz		-13.6×10^4	[71]
	3 ns, 888-1554 nm		15.8 - 0.18 x 10^4	[72]
	40 ps, 1064 nm, 10 kHz	37.4×10^{-8}		[68]
	1 ns, 1064 nm, 20 kHz	-0.2 to - 0.3 x 10^{-5}		[66]
	2.8 ps, 1930 nm, 32.3 MHz	1.6×10^{-4}	-460×10^4	[73]
	200 fs, 514 nm, 1 kHz	-0.26 to 48 x 10^{-8}		[69]
	fs, 1030 nm		-1.894×10^4	[74]
	2.8 ps, 1560 nm, 1930 nm	1.6×10^{-12}	-4.6×10^{-6}	[73]
	40 fs, 800 nm		7×10^{-9}	[70]
	100 fs, 800 nm		-13.6×10^4	[71]

standard method is used for measuring nonlinear parameters is, so it is difficult to compare the performance of metal-halide perovskite materials. In addition, In some cases, it is possible for the thickness of the substrate to dominate the measurement when using a thicker substrate than the perovskite film.

Based on these results, it is clear that perovskite materials are 20 times stronger as nonlinear materials than silicon, which is widely known as an excellent material for nonlinear optics [96].

Material	Excitation	n_2 ($m^2 W^{-1}$)	β ($m W^{-1}$)	ref
	30 ps, 1064 nm, 50 Hz	1.37×10^{-12}	23×10^{1}	[75]
	30 ps, 1064 nm, 50 Hz	1.37×10^{-12}	23×10^{1}	[75]
	200 ps, 1028 nm, 250 Hz	18×10^{-11}	186×10^{4}	[69]
	40 ns, 532 nm, 1 kHz	10^{-4}	-260×10^{4}	[69]
	200 fs, 514 nm, 1 kHz	4.8×10^{-7}	22×10^{4}	[69]
	200 fs, 514 nm, 250 Hz	6.9×10^{-7}	18.5×10^{4}	[69]
$CsPbI_3$	1 ns, 1064 nm, 20 kHz	0.3 - 0.8 x 10^{-8}		[76]
	1 ns, 750-925 nm, 1 kHz	0.19×10^{-8}		[75]
	396 fs, 787 nm, 1 kHz	6.75×10^{-11}		[75]
	100 fs, 800 nm, 1000 Hz		0.095×10^{-2}	[77]
	396 fs, 787 nm, 1000 Hz		0.015×10^{-2}	[75]
$EAPbI_3$	800 nm		4.2×10^{2}	[78]
	100 fs, 500 nm, 1 kHz	-320×10^{-5}		[79]
$MAPbBr_3$	40 fs, 800 nm, 1 kHz		5×10^{2}	[70]
	10 ns, 532 nm, 200 Hz	-8.7×10^{-4}	-3.5×10^{7}	[80]
	30 fs, 600 nm, 10 kHz	1.5×10^{-6}		[81]
	40 fs, 800 nm, 1 kHz	0.7×10^{-8}		[70]
	1 ns, 1064 nm, 20 kHz	1.1 - 3.5 x 10^{-5}		[66]
	100 fs, 800 nm, 1 kHz		5.5×10^{4}	[71]
	130 fs, 800 nm, 76 MHz	-4.01×10^{-9}		[82]
	100 fs, 800 nm, 76 MHz		8.2×10^{-9}	[82]
	30 ps, 1064 nm, 50 Hz		9×10^{1}	[83]
	100 ps, 800 nm, 1000 Hz		2.0×10^{-1}	[84]
	68 fs, 800 nm, 1000 Hz		0.0014 - 0.0018 x 10^{-2}	[85]
$CsPbBr_3$	40 fs, 800 nm, 1 kHz		5×10^{2}	[70]
	35 fs, 800 nm, 1 kHz		1.94×10^{2}	[86]
	500 ps, 1060 nm	1.35×10^{-8}		[75]

Material	Excitation	n_2 ($m^2 W^{-1}$)	β ($m W^{-1}$)	ref
	fs, 800 nm, 1 kHz		9.1×10^{-1}	[77]
	800 nm		8.5×10^{-1}	[87]
	100 fs, 800 nm, 1 kHz		9.7×10^{-1}	[88]
	100 fs, 800 nm, 1 kHz	-1.99×10^{-9}	-0.68×10^{1}	[82]
	50 fs, 600 nm, 1 kHz	0.8×10^{-8}		[89]
	50 fs, 600-800 nm, 1 kHz	0.8 to - 1.2 x10^{-8}		[89]
	396 fs, 787 nm, 1 kHz	4.69×10^{-11}	3.22×10^{-1}	[76]
	fs, 750 - 925 nm, 1 kHz	1.35×10^{-8}		[75]
	50 fs, 600 nm, 1 kHz(high intensity)	0.65×10^{-8}		[89]
	50 fs, 600-800 nm, 1 kHz(low intensity)	-0.01 to - 0.18 x10^{-5}		[89]
	130 fs, 800 nm, 76 MHz	-5.18×10^{-9}	-1.71×10^{7}	[82]
	200 fs, 800 nm, 76 MHz	-1.99×10^{-9}	-0.68×10^{7}	[82]
	340 fs, 515 nm, 1 kHz		-0.35×10^{7}	[90]
	70 fs, 800 nm, 1 kHz	10^{-5}	180×10^{-13}	[89]
	70 fs, 600 nm, 1 kHz		95×10^{-2}	[91]
	70 fs, 800 nm, 1 kHz		0.71×10^{-13}	[89]
	30 ps, 1000 nm, 50 Hz		5×10^{1}	[83]
	130 fs, 800 nm, 7.6 Hz	-2.0×10^{-8}		[82]
	10^6 fs, 1064 nm, 2 x 10^4 Hz	0.8 - 1.2 x 10^{-3}		[82]
$FAPbBr_3$	35 fs, 800 nm, 1 kHz		7.6	[92]
	100 fs,800 nm, 1 kHz		0.0042×10^{7}	[78]
	200 fs, 1560 nm, 100 kHZ	1.46×10^{-19}		[93]
$MAPbCl_3$	40 fs, 800 nm, 1 kHz	3.4×10^{-5}	1.5×10^{2}	[70]
	30 ps, 532 nm, 50 Hz		13×10^{1}	[83]

Material	Excitation	n_2 ($m^2 W^{-1}$)	β ($m W^{-1}$)	ref
$CsPbCl_3$	100 fs, 620-630 nm, 76 MHz	-0.46×10^{-9}		[94]
	396 fs, 787 nm, 1 kHz	5.3×10^{-11}	1.36×10^{-1}	[71]
	100 fs, 620 nm, 1 kHz	-4.6×10^{-10}		[95]
	fs, 750-925 nm, 1 kHz	0.33×10^{-8}		[75]
	396 fs, 787 nm, 1000 Hz		0.014×10^{-2}	[76]

Table 2.1 Nonlinear optical properties of perovskite materials.

2.7. Metal-free perovskites

The first metal-free perovskite, piperazinium ammonium chloride hydrate, was reported in 2002 by Bremner et al [97]. Since then, many metal-free perovskites have been developed. The metal-free perovskites also have the ABX_3 configuration (where A and B are cations and X are anions), only the B site is occupied by NH_4^+ in this case as seen in Figure 2.8. For the A site, many organic molecules have been identified to be suitable in the perovskite framework, [23] with strong interests in DABCO (*N*-*N*′- diazabicyclo[2.2.2]octonium, $C_6H_{12}N_2$) and its derivative Methyl-DABCO (*N*-methyl-*N*′- diazabicyclo[2.2.2]octonium, $C_7H_{15}N_2$).
It is particularly interesting that metal-free perovskites are attracting attention lately in the light of their excellent ferroelectric properties that were first reported [23] in 2018 and also because they were predicted to be suitable for second-order nonlinear optics [98] [3].

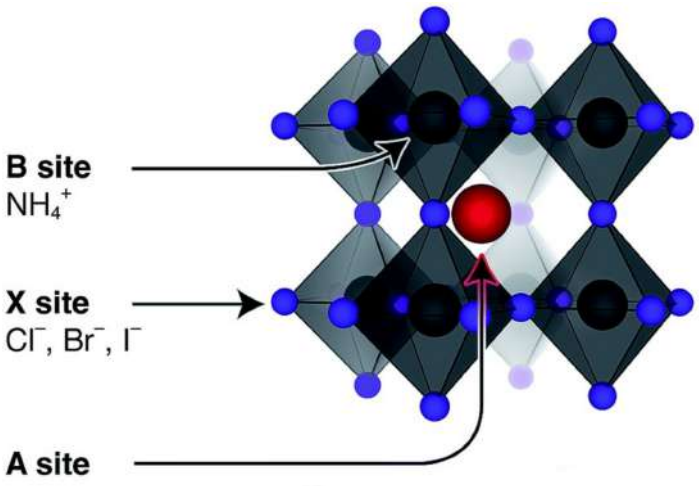

Figure 2.8 The ABX_3 structure of a metal-free perovskite, with A being organic cations (red balls), B being NH_4^+ (grey balls) and X being halides (purple balls) [3].

As these materials are highly soluble in water, they can also form single crystals in water at room temperature. In contrast with metal-halide perovskites, which are processed by toxic solutions, this approach uses less energy and poses fewer risks to human and environmental health. Many methods exist to apply the aqueous metal-free perovskite solution on a substrate, such as slot-die coating, doctor blade coating, and spin coating.

2.8. Potential Applications

2.8.1. Nonlinear optics

According to the minimal optical studies that have been conducted, metal-free perovskites material exhibits a very large band gap, greater than 5 eV, which permits its use in visible and ultraviolet regions [98], in contrast to metal-halide perovskites. Due to the wide band gap of metal-free perovskite materials, they have a high laser-induced damage threshold, which makes them an excellent choice for use in nonlinear optics, as high-intensity light is usually needed to operate within this regime.

2.8.2. Ferroelectrics / Piezoelectrics

Among their many advantages, metal-free perovskite materials also outperform conventional inorganic ferroelectrics. The development of metal-free ferroelectric perovskites with excellent piezoelectric properties might enable the development of even smaller computer chips in the future. The advantage of this technology is that devices such as heart-rate monitors and ultrasound machines can be bent and folded like a piece of paper.

2.8.3. Smart Tags

As a result of the limitations of existing technologies in smart tags, such as chips, packaging, testing, and variable data, a search is being conducted to develop novel biocompatible materials and methods. It is also possible that metal-free perovskites may be developed in this area in the future. A further benefit of these materials is that they have great potential as components in sensor systems, human-computer interaction technology, micro-electromechanical systems, and nanorobots. The utilization of metal-free perovskites as novel functional materials for optoelectronics has excellent potential in the future, primarily because of their excellent

properties, such as lightweight, mechanical flexibility, eco-friendly processing, and excellent optoelectronic properties.

2.9. Optical nonlinearity in perovskites

Nonlinear optical technologies generally take advantage of second-and third-order susceptibilities. Usually, second-order processes are limited to materials that do not have a centrosymmetric crystal structure. Contrary to this, all materials have a third-order nonlinearity, and this is capable of causing phenomena such as two-photon absorption and optical Kerr effect. Most typical media exhibit weak third-order nonlinearities. For most applications, high peak laser intensities are required for significant nonlinearity. Consequently, materials with high optical nonlinearity have been sought after since they are generally more efficient. The silicon-on-insulator platform is a perfect example of this activity. Silicon has a fixed bandgap in the visible region of the electromagnetic spectrum, which is 1.1 eV, so it is not transparent and exhibits strong two-photon absorption in an important window of the near-infrared (near-IR). A new class of materials based on metal-halide perovskite has been proposed for nonlinear optics. $MAPbI_3$, for example, exhibits a large nonlinear response for both films and single crystals in the near-IR transmission window [69] [68] [73] [70]. These materials have a Kerr optical nonlinearity that's orders of magnitude greater than silicon, so they're a natural candidate for nonlinear optics [68]. Similarly to silicon, hybrid halide perovskites exhibit strong two-photon absorption in the near IR but do not transmit visible light.

2.10. Nonlinear optical materials

This field of nonlinear optics is concerned with the analysis of the nonlinear interaction between light and matter when changes in the optical properties of the medium are made due to light-induced changes in the medium [99]. Nonlinear optics materials are in which the polarization density P responds non-linearly to the electric field $\mathbf{E}$ of the light. The non-linearity is typically observed only at very high light intensities. Nonlinear optical materials can be either organic or inorganic in composition. Since the advent of lasers, inorganic materials have been used as optical materials and, consequently, inorganic materials have dominated optical technology over the last 40 years. The study of organic nonlinear optical materials has been

conducted in addition to that of inorganic nonlinear optical materials. The nonlinear optical properties that are exhibited by organic materials can be attributed to their highly mobile electrons, and delocalized electrons, which lead to their fast nonlinear response. A nonlinear optical material is an essential component of nonlinear optics, which is of particular importance in the fields of industrial applications, and information technology. Furthermore, nonlinear optical materials contributes to the development of large-capacity communications, as further incorporation of these materials may provide a device in an all-optical communication system. Nonlinear optical materials have made very little progress over the past 20 years. It could be that the optimization process often involves trial and error, which is time-consuming and resource-intensive, which is one possible reason for the lack of significant progress in nonlinear optical materials over the past twenty years. Low lighting intensities result in no interaction of optical waves in medium, so optical materials display independent properties. Materials with strong nonlinear optical properties exhibit nonlinear optical phenomena such as wavelength conversions, amplifications, and refractive index changes based on optical intensity. The importance of nonlinear optics lies in the ability to understand the nonlinear behaviour of the induced polarization and control as well as analysing its influence on the propagation of light through media. Maxwell equations can be used to explain NLO phenomena as described below.

2.10.1. Mathematical theory of nonlinear optical materials

A Maxwell equation in the phase representation is also referred to as a time-harmonic equation and describes electromagnetic fields in terms of frequency domain. Using this representation, the time-dependent fields are expressed as complex phasors that have a specified frequency associated with them. Maxwell's equations in the phase representation are summarized in the following manner:

Gauss's Law for electric fields:

$$\nabla \cdot \mathbf{E} = \frac{\rho}{\varepsilon_0} \tag{2.1}$$

Gauss's Law for magnetic fields:

$$\nabla \cdot \mathbf{B} = 0 \tag{2.2}$$

Faraday's Law of electromagnetic induction:

$$\nabla \times \mathbf{E} = -j\omega\mathbf{B} \tag{2.3}$$

Ampere's Law with Maxwell's addition:

$$\nabla \times \mathbf{B} = -j\omega\mathbf{D} + \mu_0 J \tag{2.4}$$

Where **E** is electric field, ρ is the charge density, ε_0 is the permittivity of free space, **B** is magnetic field, j is the imaginary unit, ω is the angular frequency, **D** is the electric displacement field, μ_0 is the permeability of free space and J is the current density.
By taking the curl of Faraday's Law and Ampere's Law with Maxwell's addition, we can derive wave equation from Maxwell's equations in the phasor representation.
Taking the curl of Faraday's Law, we get:

$$\nabla \times (\nabla \times \mathbf{E}) = -j\omega(\nabla \times \mathbf{B}) \tag{2.5}$$

Using the vector identity

$$\nabla \times (\nabla \times \mathbf{E}) = \nabla(\nabla \cdot \mathbf{E}) - \nabla^2\mathbf{E} \tag{2.6}$$

, and applying Gauss's Law for electric fields, we get:

$$\nabla(\nabla \cdot \mathbf{E}) - \nabla^2\mathbf{E} = -j\omega(\nabla \times \mathbf{B}) \tag{2.7}$$

Since $\nabla \cdot \mathbf{B} = 0$, the equation simplifies to:

$$\nabla^2\mathbf{E} + k^2\mathbf{E} = 0 \tag{2.8}$$

This equation represents the wave equation for a electric field in the phasor representation.
In this equation $k = \omega$ /v is the wave number, and v is the phase velocity. Equation 2.8 is the wave equation for the electric field in the phasor representation.

Similarly, taking the curl of Equation 2.4, we get:

$$\nabla \times (\nabla \times \mathbf{B}) = j\omega(\nabla \times \mathbf{D}) + \mu_0(\nabla \times J) \tag{2.9}$$

Using the vector identity

$$\nabla \times (\nabla \times \mathbf{B}) = \nabla(\nabla \cdot \mathbf{B}) - \nabla^2\mathbf{B} \tag{2.10}$$

, and applying Gauss's Law for magnetic fields, we get:

$$\nabla(\nabla \cdot \mathbf{B}) - \nabla^2\mathbf{B} = j\omega(\nabla \times \mathbf{D}) + \mu_0(\nabla \times J) \tag{2.11}$$

As a result, the equation can be simplified as follows:

$$\nabla^2\mathbf{B} + k^2\mathbf{B} = -j\omega(\nabla \times \mathbf{D}) - \mu_0(\nabla \times J) \tag{2.12}$$

The Equation 2.12 can be rewritten as follows by using Maxwell's equations in the phasor representation (Gauss's Law for electric fields:$\nabla \cdot \mathbf{D} = \rho$ and Gauss's Law for magnetic fields: $\nabla \cdot J$= - ($\frac{\partial \rho}{\partial t}$)):

$$\nabla^2\mathbf{B} + k^2\mathbf{B} = j\omega\varepsilon_0\frac{\partial \mathbf{E}}{\partial t} - \mu_0\frac{\partial J}{\partial t} \tag{2.13}$$

This equation represents the wave equation for a magnetic field in the phasor representation. The Equations 2.8 and 2.13 describe how electromagnetic waves propagate through space in the frequency domain.

To derive the basic inhomogeneous wave equation in a nonlinear medium from Maxwell's equations in phasor representation, we start with the Equations 2.8 and 2.13.

In a nonlinear medium, the electric field and magnetic field are related to the electric displacement field **D** and magnetic flux density **S** as follows:

$$\mathbf{D} + \varepsilon_0\mathbf{E} + P(\mathbf{E}) \tag{2.14}$$

$$\mathbf{S} = \mu_0\mathbf{H} + M(\mathbf{S}) \tag{2.15}$$

Where $P(\mathbf{E})$ is the polarization vector and $M(\mathbf{S})$ is the magnetization vector.

Using these relations, we can rewrite the Equations 2.13 as:

$$\nabla^2\mathbf{B} + k^2\mathbf{B} = j\omega\varepsilon_0\frac{\partial(\varepsilon_0\mathbf{E} + P(\mathbf{E}))}{\partial t} - \mu_0\frac{\partial J}{\partial t} \tag{2.16}$$

As a result of expanding the time derivatives and rearranging terms, we obtain:

$$\nabla^2\mathbf{B} + k^2\mathbf{B} = j\omega\varepsilon_0(\varepsilon_0\frac{\partial\mathbf{E}}{\partial t} + \frac{\partial P(\mathbf{E})}{\partial t}) - \mu_0\frac{\partial J}{\partial t} \tag{2.17}$$

Now, we can substitute the Equation 2.8 for $\nabla^2\mathbf{E}$ into this expression:

$$-\nabla^2\mathbf{E} + k^2\mathbf{E} = 0 \tag{2.18}$$

When we multiply this equation by -$j\omega\varepsilon_0$ and rearrange the terms, we get:

$$j\omega\varepsilon_0\nabla^2\mathbf{E} - k^2 j\omega\varepsilon_0\mathbf{E} = 0 \tag{2.19}$$

Now, we can use the relation $\nabla\times(\nabla\times\mathbf{E}) = -j\omega(\nabla\times\mathbf{B})$ to rewrite this equation:

$$\nabla(\nabla\cdot\mathbf{E}) - \nabla^2\mathbf{E} = -j\omega(\nabla\times\mathbf{B}) \tag{2.20}$$

Substituting the expressions for $\nabla\cdot\mathbf{E}$ and $\nabla\times\mathbf{B}$ from the given equations, we obtain:

$$\nabla\frac{\rho}{\varepsilon_0} - \nabla^2\mathbf{E} = -j\omega(j\omega\varepsilon_0\frac{\partial(\varepsilon_0\mathbf{E} + P(\mathbf{E}))}{\partial t} - \mu_0(\frac{\partial J}{\partial t})) \tag{2.21}$$

We can simplify further by saying:

$$\nabla(\frac{\rho}{\varepsilon_0}) - \nabla^2\mathbf{E} = \omega^2\varepsilon_0^2\mathbf{E} + \omega^2\varepsilon_0\frac{\partial P(\mathbf{E})}{\partial t} - j\omega\mu_0\frac{\partial J}{\partial t} \tag{2.22}$$

This equation can be combined with the equation for the magnetic field to get the equation for inhomogeneous waves equation in a nonlinear medium in the frequency domain:

$$\nabla^2\mathbf{E} - \omega^2\varepsilon_0^2\mathbf{E} = -\nabla(\frac{\rho}{\varepsilon_0}) + \omega^2\varepsilon_0\frac{\partial P(\mathbf{E})}{\partial t} - j\omega\mu_0\frac{\partial J}{\partial t} - k^2\mathbf{B} \tag{2.23}$$

Using the inverse Fourier transform, we can transform electromagnetic waves propagating in a nonlinear medium from the frequency domain to the time domain.
Starting with the Equation:

$$\omega^2\mathbf{E} - \omega^2\varepsilon_0^2\mathbf{E} = -\nabla(\frac{\rho}{\varepsilon_0}) - (\omega^2\varepsilon_0 + j\omega^2)P(\mathbf{E}) - \omega^2 k(\mathbf{B}) \tag{2.24}$$

, Let's consider the terms involving the angular frequency ω. We can rewrite these terms as:

$$-\omega^2\varepsilon_0^2\mathbf{E} - (\omega^2\varepsilon_0 + j\omega^2)P(\mathbf{E}) = -\nabla(\frac{\rho}{\varepsilon_0}) - \omega^2 k(\mathbf{B}) - \nabla^2\mathbf{E} \tag{2.25}$$

To proceed, we denote the Fourier transform of a variable X with respect to time X'(ω). and its inverse Fourier transform as X(t). By applying the inverse Fourier transform to both sides of the equation, we get:

$$\nabla^2\mathbf{E}(t) - \varepsilon_0^2\frac{d^2\mathbf{E}(t)}{dt^2} - \varepsilon_0\frac{d^2\mathbf{E}(t)}{dt^2} = -\nabla(\frac{\rho(t)}{\varepsilon_0}) - k(\mathbf{B}(t)) - \nabla^2\mathbf{E}(t) \tag{2.26}$$

Further Simplification leads to:

$$\frac{d^2\mathbf{E}(t)}{dt^2} - \varepsilon_0\frac{d^2\mathbf{E}(t)}{dt^2} = -\nabla(\frac{\rho(t)}{\varepsilon_0}) - k(\mathbf{B}(t)) \tag{2.27}$$

Equation 2.27 describes the transformation of the inhomogeneous wave equation in a nonlinear medium from the frequency domain to the time domain.

2.11. Self-focusing

One of the most important nonlinear optical phenomena is self-focusing. Self-focusing occurs when intense electromagnetic radiation changes the refractive index of materials as it travels through them [100]. Depending on the intensity of the electric field, a medium with higher refractive index functions as a focusing lens for an electromagnetic beam [101]. With a decrease in the beam radius which passes through a nonlinear medium, the focusing lens' strength increases, and optical intensities become even higher, enhancing self-focusing further. The self-focusing mechanism relies upon a Kerr nonlinearity with a positive refractive index. As a result of this case, the optical intensity of the beam on the beam axis will be the highest and the

optical intensity outside the beam axis will be the lowest, causing an effective increase in refractive index within the inner beam region. During the passage of the wave through the nonlinear medium, the peak intensity of the self-focused region keeps on increasing until self-defocusing effects occur. These effects occur when a medium's refractive index is negative, which means the beam axis refractive index is reduced.

Assuming a laser beam with a Gaussian intensity distribution incident to the nonlinear medium has a higher intensity in its centre. Within the material, the laser beam induces a refractive index variation, with the center of the laser beam having a higher refractive index than the periphery. As a result, the material acts as a positive lens, causing the beam to come to a focus within the medium. This effect is shown in Figure 2.9.

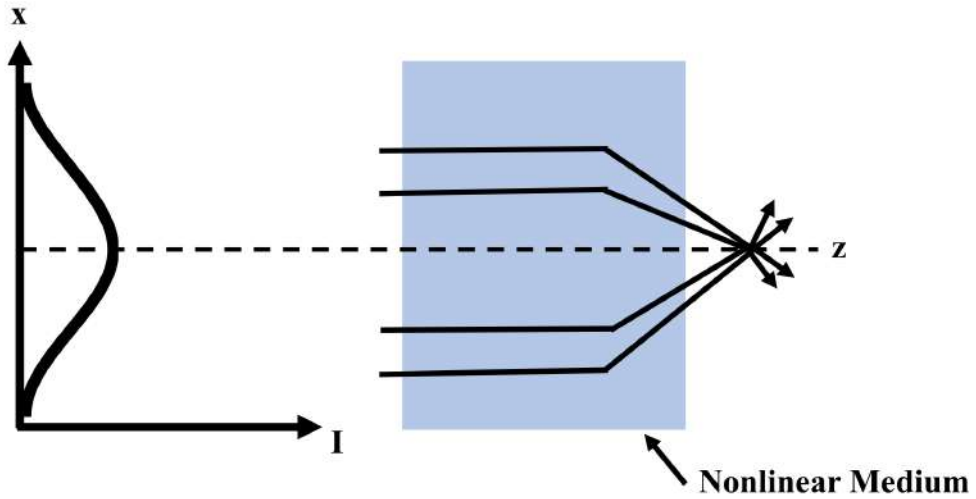

Figure 2.9 Self-focusing of the beam with Gaussian intensity definition.

2.12. Two-photon absorption (TPA)

Nonlinear absorption effects are very common phenomena that refer to the change in the transmittance of a medium as a function of optical beam intensity. Two-photon absorption (TPA) is defined as two photons having the same or different frequencies to excite an atom or molecule from one ground energy level to a higher excited level, as shown in Figure 2.10.

At sufficiently high intensity, the probability of a medium absorbing more than one photon before relaxing to the ground state is greatly enhanced. The basic theory of TPA was formulated by Goppert-Mayer [102]. In the general case, two situations are possible for TPA. In the first one, two photons from the same optical field of frequency ω are absorbed to make the resonant

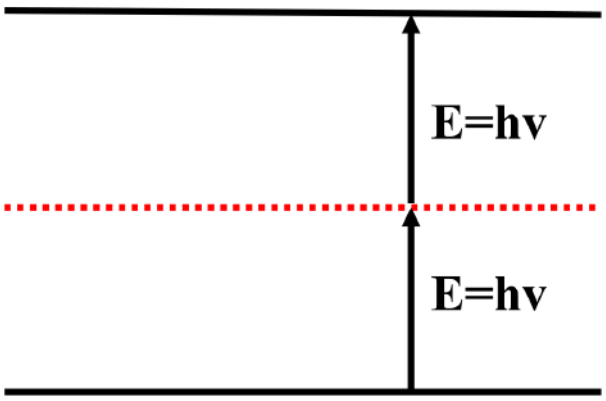

Figure 2.10 Schematic of two-photon absorption.

transition at 2ω. In the second case, two optical fields of frequency, ω and ω', are present, and one photon from each field is absorbed, making an overall transition at approximately $\omega + \omega'$. Here, we are interested in the first situation, which is the single beam case.

2.13. Techniques to measure nonlinear properties

There are several techniques capable of measuring the third-order nonlinear optical properties of materials for example optical Kerr Effect, four wave-mixing, and *z*-scan [103] [104].

2.13.1. Kerr Effect

An optical effect known as the Kerr effect can occur when light propagates through crystals and glasses and in other media such as gases. There are two different forms of the Kerr effect, and these will be explained in the following sections.

Kerr electro-optic Effect (DC Kerr Effect)

Suppose two electrodes apply slowly varying electric fields to a material, such as glass. When a light beam passes through glass, it may undergo a polarization-dependent change in the optical phase, an amount proportional to the square of the applied voltage, i.e., to the square of the electric field strength. A material that is not naturally birefringent can be made birefringent by adding polarization dependence to it. A piece of glass that is considered could then be used as a waveplate that is electrically controllable. In the case of an electric field strength applied over a

path of length L, the field-induced phase change is

$$\Delta\Phi = \frac{2\pi}{\lambda}\Delta n = 2\pi K E^2 \tag{2.28}$$

Where Δn is the difference in refractive index between two directions of polarization parallel and perpendicular to the electric field direction, K represents the Kerr constant of the material, and E represents the strength of the applied electric field.

Optical Kerr Effect (AC Kerr Effect)

The optical Kerr effect occurs when the electric field is generated by light itself. A consequence of this is a variation in the index of refraction where the change is proportional to the local irradiance of the light [101]. The refractive index of the material, when irradiated by the high-intensity light beam, is modified by:

$$\Delta n = n_2 I \tag{2.29}$$

This equation consists of the nonlinear index n_2 and the optical intensity I, proportional to the modulus squared of the electric field strength. The optical Kerr effect only becomes evident when very intense beams, such as those from lasers, are used.

2.13.2. Four-wave mixing

Four-wave mixing (FWM) represents one of the phenomena in third-order nonlinear optical processes in which two or three photons of different wavelengths interact to produce two or one photons with new wavelengths. Four-wave mixing has been one of the most used techniques for characterising nonlinear optical materials [105] [106] [99] and is still widely employed. Semiconductors are among the materials which have been studied most extensively using FWM [107] [108] particularly semiconductor optical amplifiers [109] [110] [111]. FWM can be used with various geometries in addition to degenerate four wave-mixing (DFWM) and nondegenerate four wave-mixing (NDFWM). When two of the components possess the same wavelength, the process is called DFWM [103], While in NDFWM, four components with different wavelengths interact with each other and lead to sum frequency generation or different

frequency generation. Although this wave mixing technique is sensitive to nonlinear optical effects, it requires a complex experimental setup. Precise control of beam angles is crucial in this kind of experiment and the data analysis is complicated.
z-scan technique is used in this thesis as the standard method due to its simplicity and sensitivity, and it is described in great detail in the next chapter.

2.14. Perovskite optical fibre

An optical signal is transmitted over an optical fibre-based on the total internal reflection principle. According to this principle, electromagnetic waves are trapped inside high-refractive-index cores surrounded by lower-index cladding and propagate through fibres. In 1970, the first optical fibre was manufactured, and since then researchers have been working on improving guiding properties and reducing propagation losses. In addition to reducing transmission losses, dispersion control and non-linear effects also became challenges.
The fabrication of optical fibres has been successful with several semiconductor materials, such as silicon [112], germanium [113], III-V compounds [114], and II-VI compounds [115]. Optical fibres made from perovskite crystals have many advantages in high-speed all-fibre optoelectronic applications. The integration of a light source into all-fibre optical networks can be enabled by direct bandgap low-loss single-crystal perovskite optical fibres. Moreover, single-crystal perovskite optical fibres are promising platforms for nonlinear optics and detectors based on the reported optoelectronic and nonlinear optical properties [116] [117] [117].

2.15. properties of optical fibres

2.15.1. Total internal reflection

Consider the propagation of light within an optical fibre: suppose a ray of light travels through a medium with a high refractive index (n_1) and is at a θ_i angle to the normal at the interface, then it encounters a medium with a lower index of refraction (n_2). Consequently, some light will be reflected back and refracted into the second medium, at an angle θ_r to the normal, where θ_r is greater than θ_i. Based on Snell's law of refraction, the incidence angle θ_i and refraction angle θ_r

are related to one another and to the medium's refractive indices:

$$n_1 sin\theta_i = n_2 sin\theta_r \tag{2.30}$$

An angle of incidence less than 90° should result when the angle of refraction approaches 90° and the refracted light emerges parallel to the interface between the two mediums. Incidence angle are now called critical angles, θ_c, as shown in Figure 2.11 b. From Equation 2.30 the value of the critical angle is given by:

$$sin\theta_c = \frac{n_2}{n_1} \tag{2.31}$$

Whenever light is incident from a higher index medium onto a lower index medium at the interface between two mediums of different refractive indices, the incidence angles of the incident light are larger than the critical angle. As a result, the light is completely reflected back into the original medium and the total internal reflection occurs as shown in Figure2.11 c. Optical fibre typically has a cylindrical symmetry of the core-cladding interface, which causes light that is reflected interface to continue to reflect at the first interface, therefore staying trapped in the fibre.

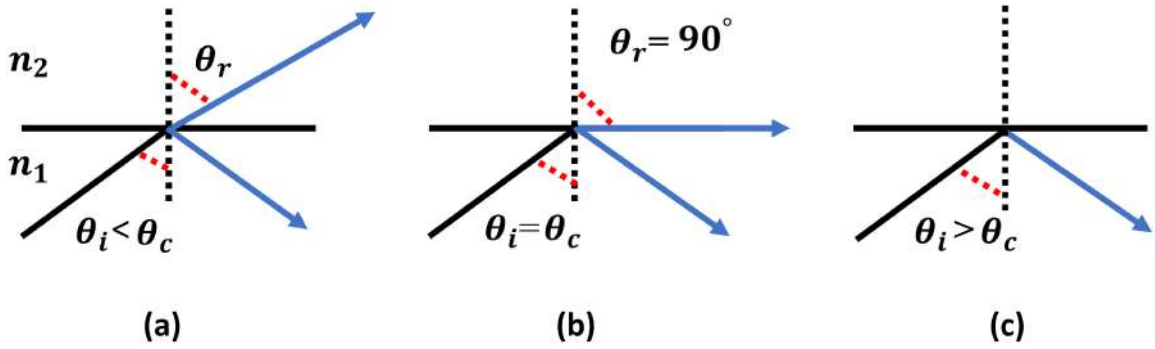

Figure 2.11 An illustration of the total internal reflection mechanism.

2.15.2. Numerical aperture (NA)

The numerical aperture (NA) refers to a fibre's ability to collect incident light rays inside the core of the fibre. When light is incident at an angle θ_i to the fibre axis, it illumines the fibre core. This angle is less than that of the fibre's acceptance angle θ_a as shown in Figure 2.12 . During light beam propagation in the optical fibre, the optical fibre core has a refractive index of n_1,

which is slightly higher than the cladding's refractive index of n_2, while the ray comes from the media (air) with a refractive index of n_0. According to Snell's law:

$$n_0 sin\theta_i = n_1 sin\theta_r \tag{2.32}$$

In regard to the right-angled triangle ABC shown in Figure 2.12 , we can conclude the following:

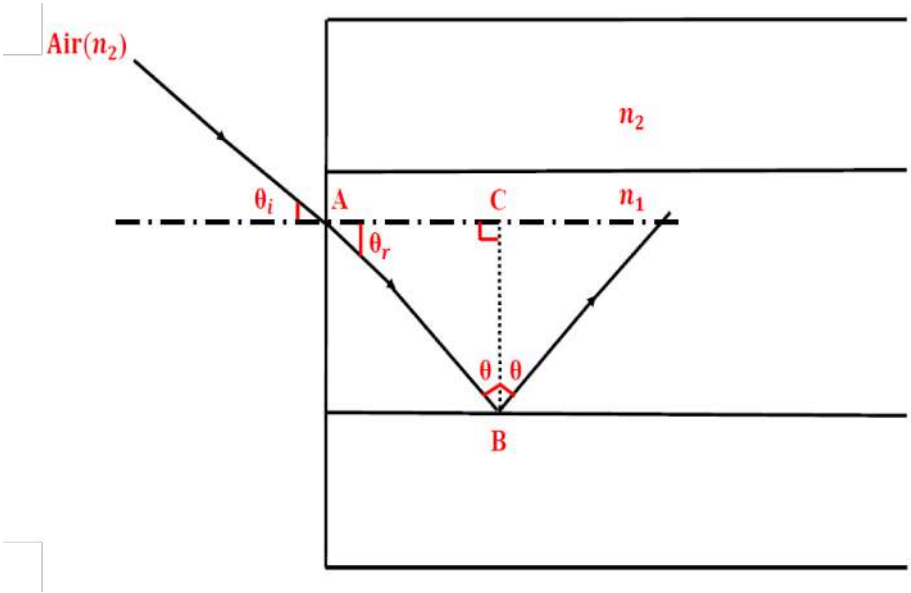

Figure 2.12 Light beams launched into optical fibres in the air with the incident angle at less than their acceptance angles.

$$\theta = \frac{\pi}{2} - \theta_r \tag{2.33}$$

At the interface of the core and cladding, θ value exceeds the critical angle. Therefore, Equation 2.32 becomes:

$$n_0 sin\theta_i = n_1 sin(\frac{\pi}{2} - \theta) \tag{2.34}$$

$$n_0 sin\theta_i = n_1 cos\theta \tag{2.35}$$

According to the trigonometric relation $\sin^2\theta + \cos^2\theta = 1$, Equation 2.35 can be written with the following form:

$$n_0 sin\theta_i = n_1 (1 - sin^2\theta)^{1/2} \tag{2.36}$$

θ becomes equal to the critical angle θ_c at the core-cladding interface when total internal reflection is considered and is given by the following Equation:

$$sin\theta_c = \frac{n_2}{n_1} \tag{2.37}$$

The acceptance angle for the optical fibre θ_a also becomes incident angle θ_i in this limit case. Combining these limiting cases into Equation 2.36 gives:

$$n_0 sin\theta_a = n_1(1 - sin^2\theta_c)^{1/2} \tag{2.38}$$

$$n_0 sin\theta_a = (n_1^2 - n_2^2)^{1/2} \tag{2.39}$$

Equation 2.39 has been established as a fundamental foundation for the determination of one of the most important parameters of optical fibre, the numerical aperture (NA).
Therefore, the NA is defined as follows:

$$NA = n_0 sin\theta_a = \sqrt{(n_{core})^2 - (n_{cladding})^2} \tag{2.40}$$

This parameter is important because it determines how effectively a fibre guides light, and therefore how resistant it is to bend-induced losses. In comparison to the cladding, a higher numerical aperture is associated with a higher core index. However, increasing NA causes higher scattering loss.

2.16. Phase and group velocity

There are always points of constant phase within electromagnetic waves. This constant phase point forms a wavefront for plane waves. During propagation of monochromatic lightwaves along a waveguide in the z-axis, the points of constant phase travel at a velocity v_p given by

$$v_p = \frac{\omega}{\beta} \tag{2.41}$$

In this equation, ω is the angular frequency of the electromagnetic wave, and β is typically used to represent the propagation constant. When a group of waves with similar frequencies

propagate together, their resultant is usually referred to as a wave packet. Figure 2.13 illustrates an example of how such a wave packet is formed when two waves propagating at slightly different frequencies combine and form a wave packet resulting from such a combination. The wave packet travels at group velocity v_g, which is given by the formula:

$$v_g = \frac{d\omega}{dk} \tag{2.42}$$

Where k is the wave vector.

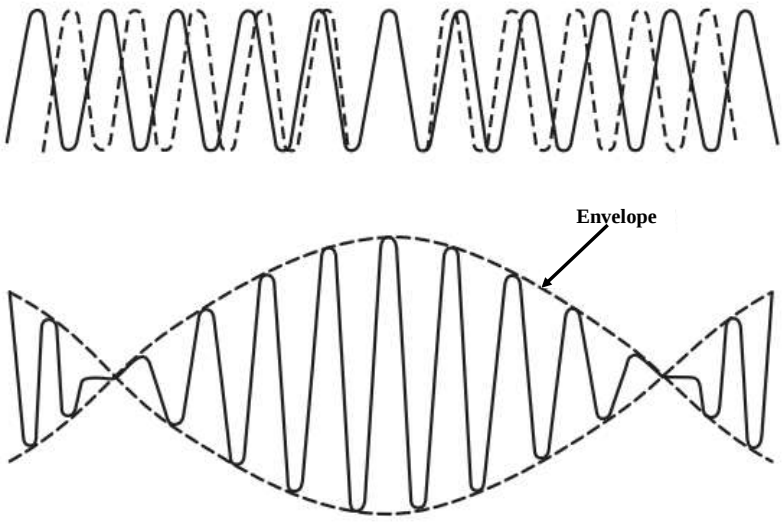

Figure 2.13 Two waves with nearly equal frequencies are combined to form a wave packet, which travels at v_g group velocity [4].

2.16.1. Fibre modes

A light ray transmitting through a fibre is propagated as electromagnetic waves as it travels through it. Across the length of the fibre, electrical and magnetic fields form patterns called modes of transmission.

Electric fields in core modes have three non-zero vector components (E_x, E_y, E_z). Transverse fields are almost exclusively contained in E_x or E_y for Maxwell equations solutions. Therefore, these modes are termed "LP" modes since the solutions are almost linearly polarized. Within the dielectric cylinder, TE (where $E_z = 0$) and TM (where $H_z = 0$) modes are obtained similarly to linearly polarized. It is important to note, however, that the cylindrical waveguide is bounded in two dimensions instead of one. Thus two integers, l and m, are necessary in order to specify the

modes. LP modes are denoted by the mode subscripts, l and m, which are dependent on the intensity profile of the electric field for a particular LP mode. TE_{lm} and TM_{lm} are the modes for cylindrical waveguides. The optic fibres can categorize into two types based on their modes.

Multimode-mode

Among the fibre types available, multi-mode fibre was the first to be manufactured and commercialized. The characteristics of a multi-mode fibre can be described by considering the path taken by light rays when propagating through it. A multi-mode fibre, as the name implies, allows for the simultaneous transmission of several modes through the fibre at the same time. So, short or medium distances can be covered with higher bandwidth. Nonetheless, data transmission can be unclear and incomplete on longer cable runs due to multiple paths of light. The use of multi-mode is therefore generally limited to applications that require short distances, such as data centres. The number of guided modes is influenced by wavelength and refractive index.

Single-mode

Single-mode fibres propagate light only in the fundamental mode, so modal dispersion is not possible in them. Essentially, for this reason, as well as the fact that they may have lower propagation losses, single-mode fibres are used for long-distance data transmission and are usually used for outdoor applications over shorter distances. The core diameter of a fibre with a single-mode characteristic is usually relatively small; the single-mode core radius is usually a few microns, making coupling light into the core more difficult. The fibre core diameter, numerical aperture, and light wavelength are three variables that can determine how many modes can be propagated inside a fibre. These variables can be compiled into the normalized frequency parameter, known as the V-number.

$$V = \frac{2\pi}{\lambda} a \sqrt{(n_c^2 - n_l^2)} = \frac{2\pi a}{\lambda} NA \tag{2.43}$$

Core radius is defined by a, wavelength by λ, and core and cladding refractive index by n_c and n_l.

For single-mode-only guidance in a cylindrical optical fibre, the V-number must be less than 2.405.

2.16.2. Fibre profiles

Fibre cables can be classified based on their index profiles. The index profile describes the value of the refractive index of the material across the core diameter. Step index fibres and graded index fibres are two basic types of index profiles.

Step-index fibre

In step-index fibre, the refractive index profile (RIP) comprises a core refractive index higher(n_c) than cladding refractive index(n_l), and total internal reflection is the principle of operation. This is because RIP for step-index fibre makes a change as they proceed towards the cladding interface, as shown in Figure 2.14. Compared with multimode step-index fibres, single-mode step-index fibres have the distinct advantage of low intermodal dispersion due to the fact that only one mode is transmitted, whereas, with multimode step-index fibres, considerable dispersion may result from different group velocities of the propagating modes. It is because of this limitation that multimode step-index fibres aren't able to achieve the same maximum bandwidth as single-mode fibres, particularly when compared with them.

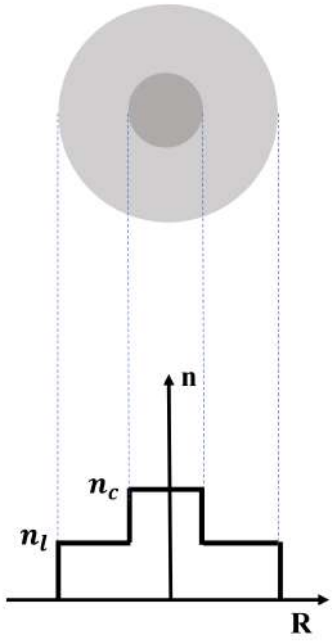

Figure 2.14 A cross-sectional diagram of a step-index fibre with a refractive index profile.

The following are some characteristics of the LP core mode behaviour in step-index fibres. For any particular mode LP_{lm}, the E-field distribution remains unchanged as it propagates through the fibre.

Graded-index fibre

A graded-index fibre does not have a uniform refractive index throughout its core. It continuously decreases from the centre to the interface of the cladding. Consequently, at its outer edge, light travels faster than at its centre. Based on geometric optics, the gradual reduction in the refractive index of a core with respect to its center creates a pattern of refraction of light rays due to the fact that the light is directly incident on a large number of interfaces that are both high and low in refractive index. Graded-index fibres have prabolic refractive index profiles, as shown in Figure 2.15. As can be seen in the figure, the light beams seem to follow curved paths as they travel through the core of the fibre. In comparison with multimode step-index fibres, multimode graded-index fibres exhibit very little intermodal dispersion, which can be attributed to the refractive index profile of these fibres. Graded-index fibres have much higher bandwidths than step-index fibres, but they still come below single-mode fibres. The main application for graded-index fibres is in medium-range communications, such as local area networks.

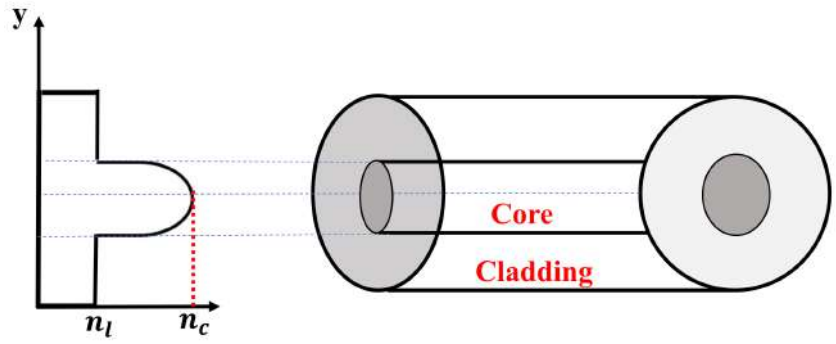

Figure 2.15 A cross-sectional diagram of a Graded-index fibre with a refractive index profile.

2.16.3. Dispersion

The phenomenon of dispersion occurs when different frequencies of waves propagate at different speeds. Due to this, the waveform disperses as it travels through the medium. In optics, dispersion is often characterized by the change in refractive index with wavelength. This

variation in the speed of light with wavelength leads to the separation of colors when passing through refractive surfaces or a prism.
Furthermore, dispersion can have implications for signal transmission. It can cause distortion in data signals. In communication systems, because different frequencies of the signal may experience different delays and arrive at the receiver at different times. This can affect the quality and accuracy of the transmitted information.

Model dispersion in multi-mode fibres

Since the core of multi-mode fibres has a much larger diameter, it can guide many different light modes. Modes enter the fibre from different angles and therefore travel through the fibre at different paths as a result. Depending on how far rays propagate through the fibre, they arrive at the fibre's end at different times. Consequently, the light pulse spreads out over time, so the signals overlap so severely that they are no longer distinguishable. Due to the limited number of modes that can be carried through a single-mode fibre, model dispersion is not an issue in single-mode fibres.

Material dispersion

This type of dispersion occurs in transparent materials, such as water or glass, where the speed of light changes with wavelength. This leads to different wavelengths of light traveling at various speeds through the medium, resulting in dispersion.

Waveguide dispersion

Waveguides, which are structures used to guide wave propagation, can also exhibit dispersion. This can occur due to the geometry and structure of the waveguide, causing different frequencies to propagate at various speeds.

2.16.4. Fibre Losses

During propagation in a fibre, transmission losses cause a significant amount of power loss and hence the signal attenuation. Since losses affect not only the transmission of information but also the possibility of observing nonlinear processes, which is dependent on power density.

2.16.5. Transmission Loss (Attenuation)

Transmission Loss (Attenuation) A fibre's attenuation is the loss of light power or signal strength as light pulses propagate along its length. Fibre attenuation is primarily caused by absorption and scattering losses. Depending on the material that makes up the fibre, absorption can occur, and scattering can occur due to structural imperfections within the fibre. Attenuation losses can be expressed in decibels per meter (dB/m) at a particular wavelength.
As a result of attenuation, power is lost along the fibre, so the output power is lower than that of the input power. Let the input optical power is P_0 at ($z = 0$).
In this case, the power at distance z is as follows:

$$P(z) = P_0 exp(-\alpha z) \tag{2.44}$$

Where α is the attenuation constant. By dividing both sides by $p_{(0)}$ and taking Ln, we get the following result:

$$Ln[\frac{P_z}{P_0}] = -\alpha z \tag{2.45}$$

$$\alpha = \frac{1}{z} Ln[\frac{P_0}{P_z}] \tag{2.46}$$

$$\alpha(dB/km) = 10\frac{1}{z}\log(\frac{P_0}{P_z}) \tag{2.47}$$

Chapter 3. Material Characterisation Techniques

One of the key tenets of this thesis is to investigate the optical nonlinearities of perovskites materials such as the metal-halide perovskites $MAPbX_3$ (X = I, Br, Cl) and metal-free perovskites DNX and MDNX, where X is the halide (I, Br, Cl). It is the goal of the present chapter to provide detailed information about all the experimental techniques available for the analysis of experimental materials used in this research. Owing to the number of different fabrication processes that will be investigated in this thesis, materials structure, crystal structure, and surface morphology will be affected, ultimately leading to different optical properties. Thus, detailed characterization of the materials is essential. The materials characterization techniques used are thermogravimetric analysis, differential scanning calorimetry, atomic force microscopy and X-ray diffraction. The techniques used to characterize the optical properties of experimental materials are UV-Vis spectroscopy for linear optical properties and the z-scan method for measuring third-order nonlinearities. Each of these techniques is summarised in this chapter and the important information that they provide is put into context for this work. For the z-scan method, a bespoke purpose-built instrument was designed and built. The design parameters and methodology will be described in detail including a full description of the calibration of the instrument.

3.1. Thermogravimetric analysis

Thermogravimetric analysis (TGA) is a destructive experimental technique that can be used to determine a material's thermal stability. The thermal stability of a material refers to the propensity of its structure to remain unchanged as a function of time [118].
TGA measures how a material's mass changes with time or temperature. These mass changes are indicative of processes such as phase changes, decomposition, degradation, sublimation, vaporization, desorption, oxidation, and reduction. During sample heating, volatile gaseous

products are the first to appear. Consequently, the original sample's mass gradually decreases. From the Figure 3.1 the horizontal portion indicates the region where there is no mass change and the material is thermally stable. It can seen that calcium carbonate $CaCO_3$ is thermally stable up to 660 °C. After that The graph declines indicating a weight loss when increase the temperature, as decomposition of $CaCO_3$ to CaO with the elimination of CO_2 occurs in the temperature range 660 and 840 °C.

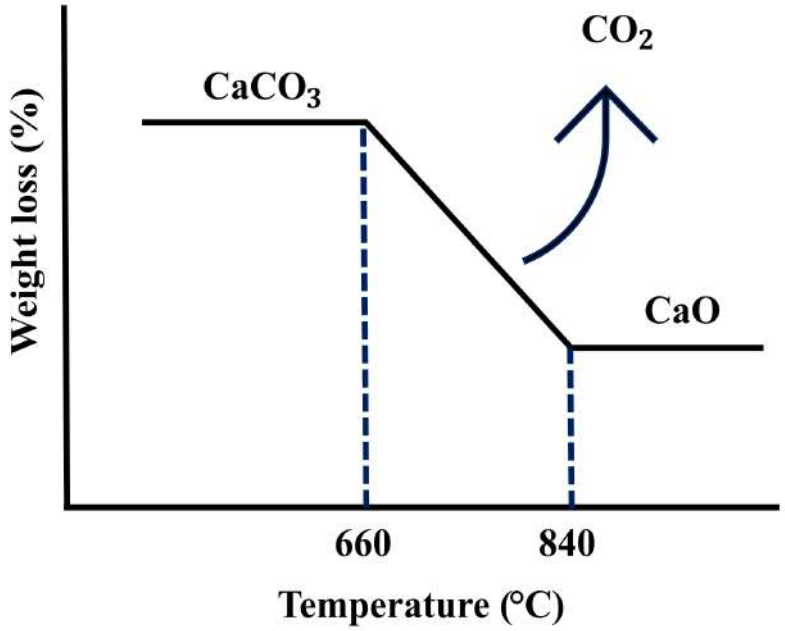

Figure 3.1 An example of a TGA characteristic curve of a thermal reaction of $CaCO_3$ to illustrate the fundamental principles of the TGA technique [5].

3.2. Differential scanning calorimetry

Differential scanning calorimetry (DSC) is a technique used in thermal analysis to determine how much heat is flowing into or out of a sample as a function of a sample's temperature or time. The sample is subject to a controlled temperature program during the measurement. DSC is an extremely efficient and powerful technique for the thermal properties of solid materials such as the melting and degradation temperatures. DSC curves are created by plotting heat flow ($W\,g^{-1}$) against sample temperature (°C) as shown in Figure 3.2. Several transitions can be identified from the DSC thermogram: glass transition temperatures (T_g), crystallization temperatures (T_c), melting temperatures (T_m), and degradation temperatures (T_d), which are all determined from low to high temperatures. There is a small change in the slope of the DSC curve when T_g is

detected. Exothermic peak T_c is observed in the curve when temperature increases sufficient to restructure the sample's structure when a sufficient amount of energy is applied. At a higher temperature, the system has received so much energy that it has gained enough energy to cause a large enough separation between molecules, which successfully breaks the intermolecular interactions that hold the molecules together, leading to the sample melting at T_m. Degradation and oxidative decomposition processes occur at T_d due to the further addition of energy at high temperatures. In this work, the DSC curve is used to determine phase transition temperature T_c so that the appropriate temperature range can be determined.

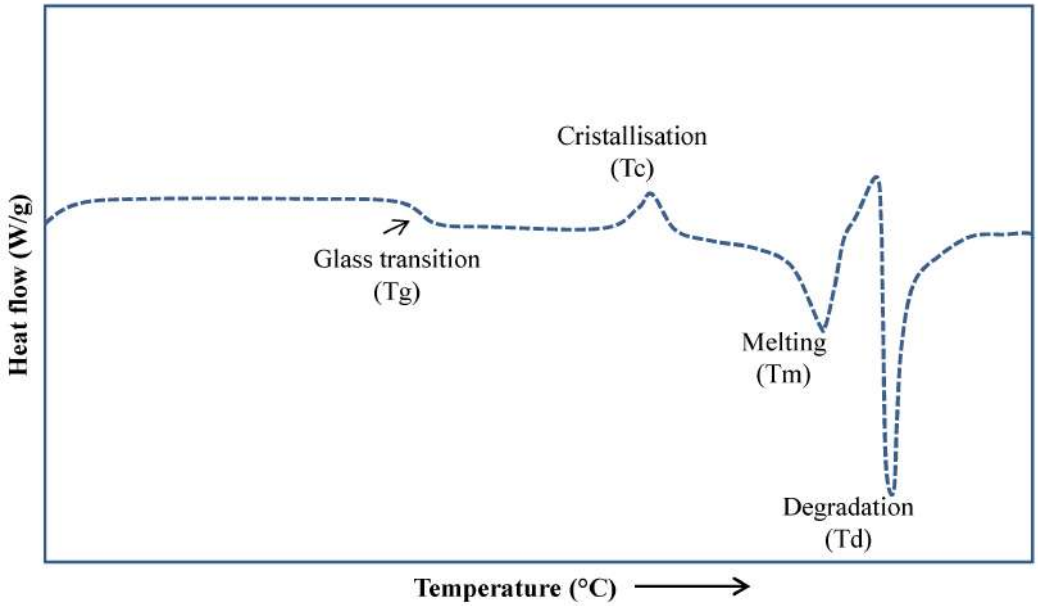

Figure 3.2 An illustration of differential scanning calorimetry (DSC) thermograms for the determination of thermal transitions in semicrystalline materials [6].

3.3. Atomic force microscopy

The atomic force microscope (AFM) was initially developed as an extension of the scanning tunnelling microscope (STM) and was designed to investigate non-conductive materials. The instrument is now the most commonly used to determine the surface topography of materials in extremely high resolution, i.e., at the nano-scale. A high-resolution image is created by scanning a small probe with an atomically sharp tip across the sample. The features on the sample's surface are detected by the displacement of a laser beam that is reflected from the back of the probe (cantilever) when it is deflected, see Figure 3.3.

AFM can be operated with three different modes: contact mode, tapping mode, and non-contact mode. In contact mode, the system keeps the distance between the cantilever tip and sample constant and records the change in position in the z-direction while scanning the sample across the xy-plane. The cantilever oscillates close to the surface of the sample when operated in non-contact mode. It oscillates at a fixed frequency and with a small amplitude, but it does not make contact with the sample's surface. In a tapping mode, the cantilever oscillates with an amplitude ranging from 20 nm to 100 nm with a frequency just above its resonance frequency. As the probe tip sweeps across the surface of the sample during scanning, it gently taps it. In interacting with the sample surface, damping occurs, resulting in a change in the tip oscillation. The photodetector is used to measure the change in the tip oscillation. The voltage applied to a piezo tube scanner is adjusted by using a feedback signal, allowing the height of the stage to be changed automatically to keep the set force [119].

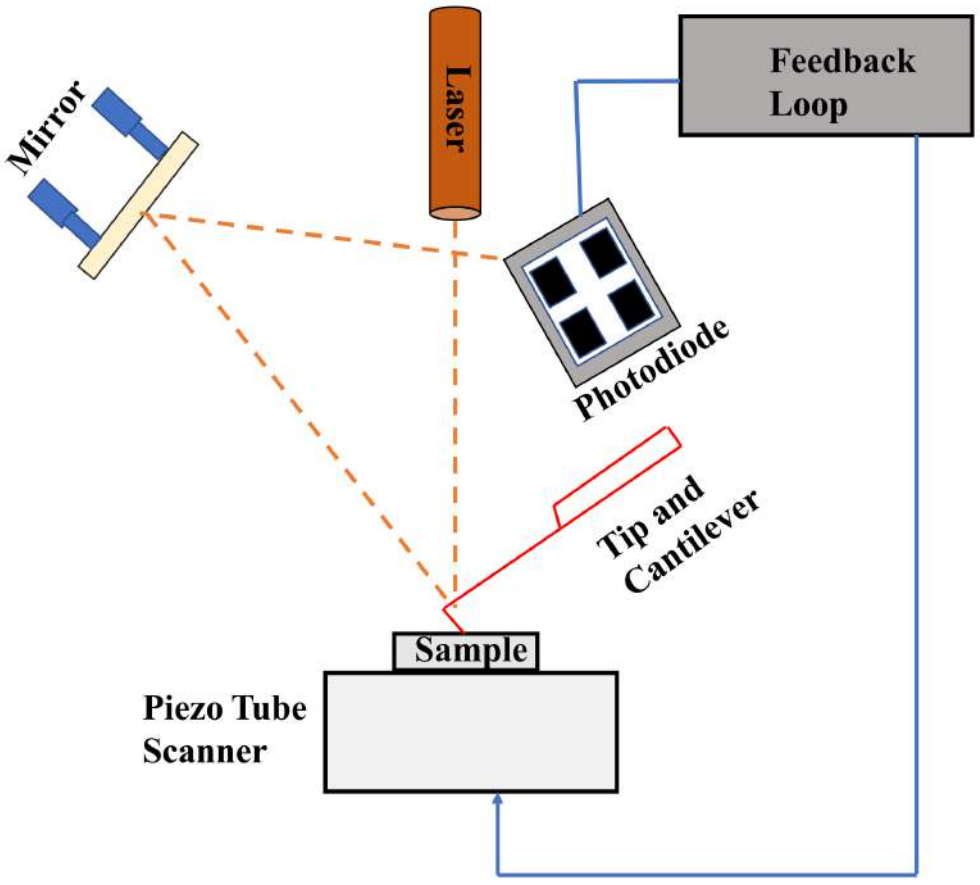

Figure 3.3 A schematic diagram of AFM. Showing atomic force micrscope princile

In order to obtain high-quality images using AFM, there are several parameters that can be controlled. One of the parameters that is typically controlled is the set point, which is one of the factors that determines how much force can be maintained between the surface of the sample and the tip during the measurement. Additionally, the scanning speed can be controlled as a second parameter. This refers to how fast the tip moves over the sample surface. Furthermore, there are other factors that contribute to the quality of AFM images, such as the image rotation angle [119].

AFM can be used to obtain three types of data while scanning: height, amplitude, and phase. In order to determine the level of roughness and morphology of a surface, height is used. In addition to identifying heights and shapes, amplitude signals can also provide useful feedback during the process of acquiring images. The phase signal gives information on how homogeneous the material is mechanically [119].

To interpret and present the data obtained during an AFM measurement with high degrees of accuracy, it is usually necessary to perform data processing before the results are interpreted. A common part of data processing is image “levelling” and “flattening” [119]. Generally, data levelling is the first processing operation carried out on the data, and it is almost always required. The method of applying data levelling is to add a constant to the scan line in order to ensure the minimum height of the image is zero. Almost all AFM data require data flattening to remove the inevitable artefacts resulting from the acquisition process (sample tilt, scanner bow, line, etc.) and correct the curvature distortion of the background image. By fitting a polynomial to each scan line and subtracting the polynomial shape from each scan line, causing the line to flatten.

It is relatively straightforward to acquire and process AFM images, but artefacts can cause results to appear to be misleading. There are several possible causes of artefacts such as electronic noise (high-frequency oscillations or repeating patterns), broken tip (when scanning a flat surface at a high scan speed), interference (discrepancies between laser reflections off the cantilever and part of the surface), and sample contamination (by fingerprints, oil, etc.). The most common types of artefacts that might occur during scanning, such as repeated features, streaks, and sheared images, are fixed by adjusting the scan parameters, slowing down the scanning speed, and even replacing the tip [120]. Figure 3.4 shows an example of an AFM

image as acquired and the same image post-processed to allow for accurate measurement of quantities such as rms roughness.

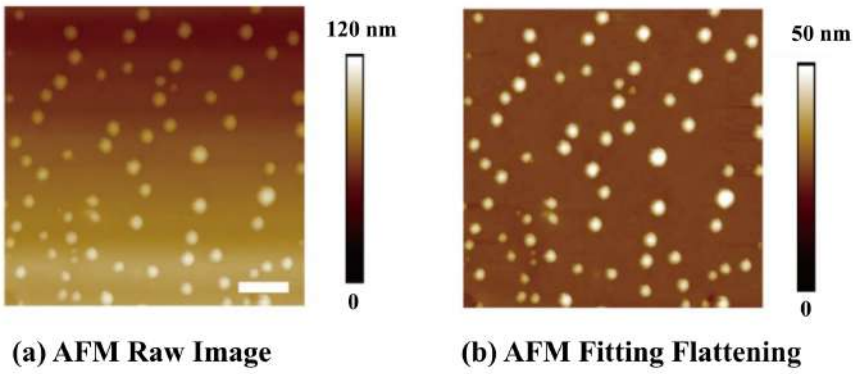

Figure 3.4 a) An AFM image of nanobubbles as acquired, b) a post-processed image [7].

The work in this thesis was supported by using an XE-150 model from Park Systems equipped with a NuNano NuScout 350 tip to characterize the surface morphology in non-contact mode.

3.4. X-ray diffraction

The X-ray diffraction (XRD) difractogram of a material provides information about its crystal structure. Diffraction of X-rays occurs when they strike a material and are coherently scattered by the material's crystalographic planes. X-ray diffractograms records scattering angles of incident X-rays, which are related to the Bravais lattice group and the size of the crystal unit cell. This coherent scattering occurs because of the wavelength of an X-ray is comparable to the spacing between atoms in a crystal.

The reciprocal space concept explains diffraction from a crystal. Through Fourier transformation, the Bravais lattice can be interpreted as a reciprocal lattice. Equations 3.1a and 3.1b can represent lattice vectors both in real space (r) and reciprocal space (r^*). Equation 3.1c describes the relationship between these vectors in real and reciprocal space, where the reciprocal lattice vector is perpendicular to two of the real lattice axes.

$$r = n_1 a_1 + n_2 a_2 + n_3 a_3 \tag{3.1a}$$

$$r^* = n_1 a_1^* + n_2 a_2^* + n_3 a_3^* \tag{3.1b}$$

$$a_1^* = \frac{1}{a_1'} a_2^* = \frac{1}{a_2'} a_3^* = \frac{1}{a_3} \tag{3.1c}$$

Where the n_i are any integers, and a_i, a_i^* linearly independent primitive translation vectors that are characteristic of the lattice in real and reciprocal space respectively. Bragg's law describes X-ray diffraction in crystals. Let us suppose that two parallel monochromatic X-rays with wavelength λ are incident on two parallel planes separated by a distance of d_{hkl} at an incident angle θ. Two waves are scattered by atoms, which leave the crystal under the same angle θ as they entered , see Figure 3.5. A constructive interference occurs when the phase of the diffracted

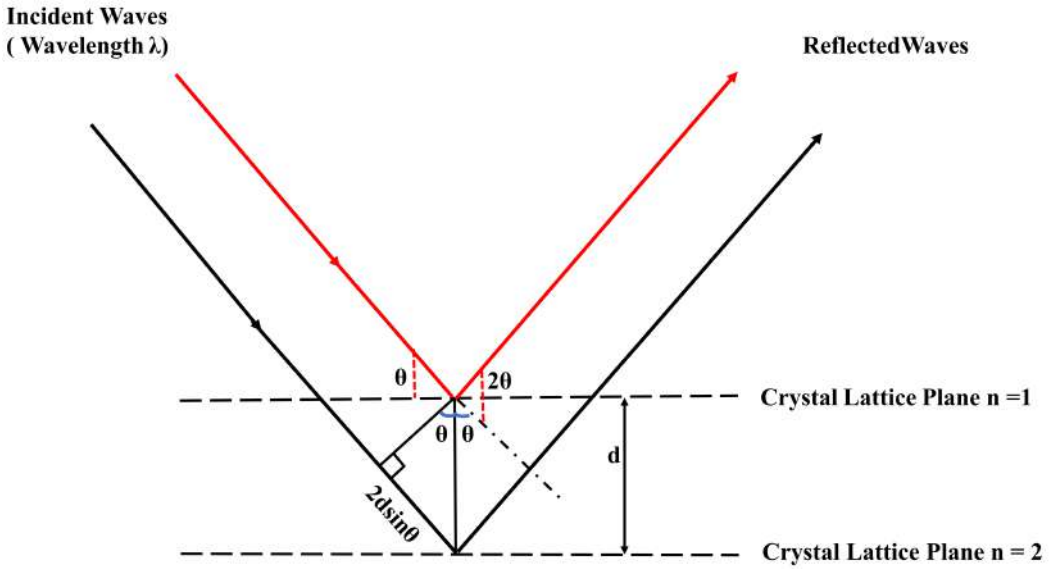

Figure 3.5 Diagram demonstrating Bragg's Law. Two beams of characteristic X-rays travel in constructive interference and parallel to each other toward the sample material at an angle θ.

waves remains the same and their path differences equal integral multiples of the wavelength, which is equal to $2d_{hkl} \sin\theta$. Therefore, Bragg's law can be defined as follows:

$$n\lambda = 2d_{hkl} \sin\theta. \tag{3.2}$$

Where n is the order of reflection of a particular crystal plane, λ is the wavelength of the radiation, d_{hkl} is the interplanar spacing between the Miller indices of the hkl planes, and θ is the angle of incidence beam. Considering n and λ as known variables, the distance d can be calculated. Bragg's law describes the relationship between diffraction angle and interplanar spacing d_{hkl}. In order to determine the direction of the plane, we can use an equation which

relates the distance between two planes to the lattice parameters a, b, and c and to the Miller indices h, k, and l, as follows:

$$d_{hkl} = (\frac{h^2}{a^2} + \frac{k^2}{b^2} + \frac{l^2}{c^2})^{-1/2}. \tag{3.3}$$

According to Bragg's law, atom diffraction only occurs at corner unit cells. Nevertheless, atoms can scatter waves at any other position in a unit cell, such as in the centre (body-centered) or the centre of the faces (face-centered). In doing so, waves become out of phase. For example, in the case of the body-centered cubic crystal structure, the sum of h, k and l should be even numbers and the h, k, and l should all be even or odd numbers in case of diffraction by the face-centered cubic structure. Consequently, Bragg's law becomes a necessary condition which must be met for diffraction to occur, but it is not sufficient for the process to occur. Hence, the structure of the crystal determines greatly the reflection planes, as a result.

X-rays can be generated by directing a high energy electron at a metal target within a vacuum tube. A metal's ground state electrons are excited by an incident electron beam, leaving holes in the orbital. When excited electrons revert to the ground state, X-rays are emitted. During the process of filling up a hole created in the K-shell with an electron from the L-shell, the energy changes give rise to the characteristic K_α X-ray with a fixed wavelength. As shown in Figure 3.6, the goniometer is the component that can be rotated around different axes, permitting the sample to be scanned in different directions and providing various reciprocal lattice points that satisfy Bragg's condition. The XRD technique is used in this work to identify material phases in the experimental materials.

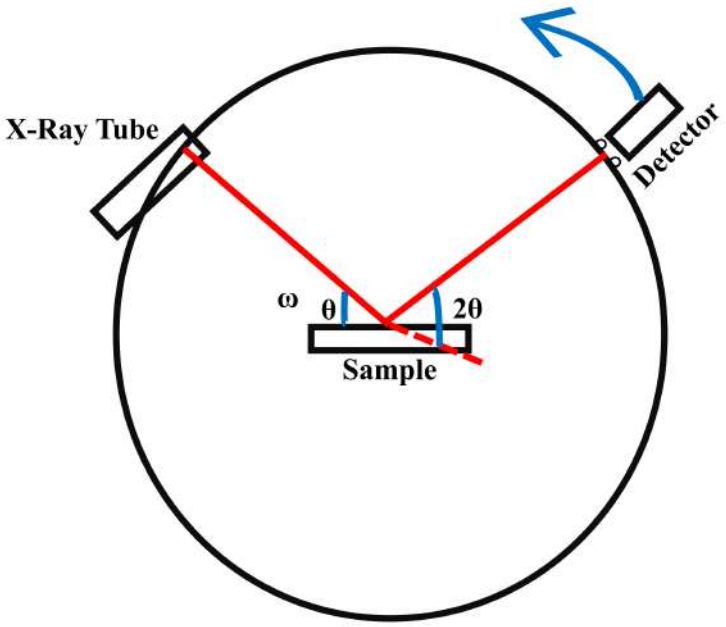

Figure 3.6 A scematic of the core components in an X-ray diffractometer.

3.5. UV-visible spectroscopy

The UV-Vis spectroscope measures the absorption or reflection of light by a sample in relation to its wavelength. The light source used for both absorption and reflectance measurements is typically a deuterium and halogen lamp that can generate light with a range of wavelengths between 190 nm to 1200 nm, corresponding to 6.53 eV and 1.03 eV respectively.

The basic principle behind the absorption of light pertains to its interaction with matter. When light is absorbed by matter, electrons are excited from the ground state to a higher energy state. The strength of absorption is determined by the density of energy states in an equivalent transition.

The components of the spectroscope are a light source, a chamber to hold the cuvette or solid sample, detectors such as photodiodes to detect the light transmitted, and analysis software.

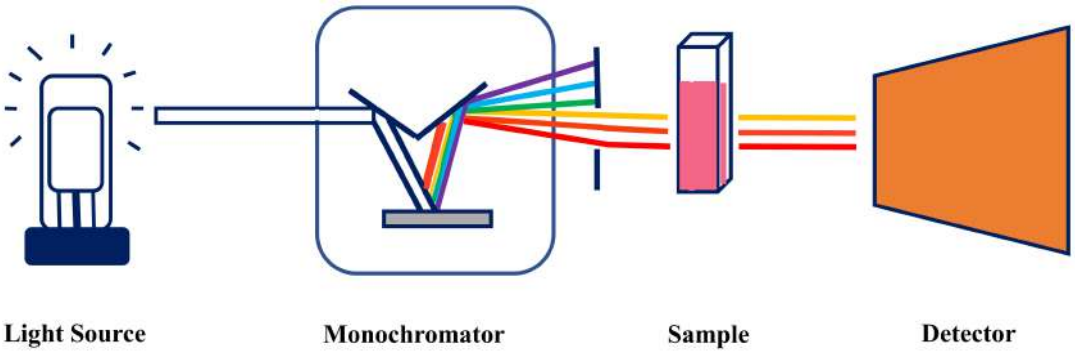

Figure 3.7 A diagram showing the components of UV-Vis with a single monochromator light source.

The transmitted light (Transmittance (T)) is measured as a function of wavelength by the detector. It is possible to directly convert the transmittance to the absorbance by using Equation 3.4.

$$Abs = log\frac{1}{T} \tag{3.4}$$

In order to obtain the absorption coefficient (α, $\mathrm{eV\,cm^{-1}}$) directly as a function of energy, it is necessary to consider the thickness of the film. The value of E_g can usually be determined from Tauc plot [121, 122], in the Tauc method, the energy-dependent absorption coefficient α can be expressed as

$$\alpha hv = A(hv - E_g)^n \tag{3.5}$$

Where h is the Planck constant, v is the photon's frequency, (hv is the photon energy (eV)), A is constant and n determines the characteristics of electron transition in a semiconductor, for direct and indirect allowed transitions, n =1/2 and 2 respectively. A diffuse reflectance spectrum is usually used to determine band gap energy. By applying a Kubelka-Munk function ($F(R_\infty)$) as shown in Equation 3.6, it was found that measured reflectance spectra could be converted into corresponding absorption spectra based on the theory of P. Kubelka and F. Munk published in 1931 [123].

$$F(R_\infty) = \frac{K}{S} = \frac{(1-R_\infty)^2}{2R_\infty} \tag{3.6}$$

The reflectance of an infinitely thick specimen can be given by $R_\infty = R_{sample}$ / $R_{reference}$, K and S correspond to its absorption and scattering coefficients respectively [124]. By substituting $F(R_\infty)$ for α, Equation 3.5 results in the following.

$$F(R_\infty)hv = A(hv - E_g)^n \tag{3.7}$$

Figure 3.8 shows a plot of a Tauc adjusted reflectance spectrum (as calculated with the equation 3.5) of a semiconductor (an indirect band gap semiconductor) plotted against the photon energy. It shows a steep linear increase in light absorption as the energy increases which is characteristic of semiconductors. An estimate of the band gap energy is given by the x-axis intersection point of the linear fit of the Tauc plot. It is possible to apply this method to all semiconductor materials that exhibit negligible absorbance below the band gap energy. However,

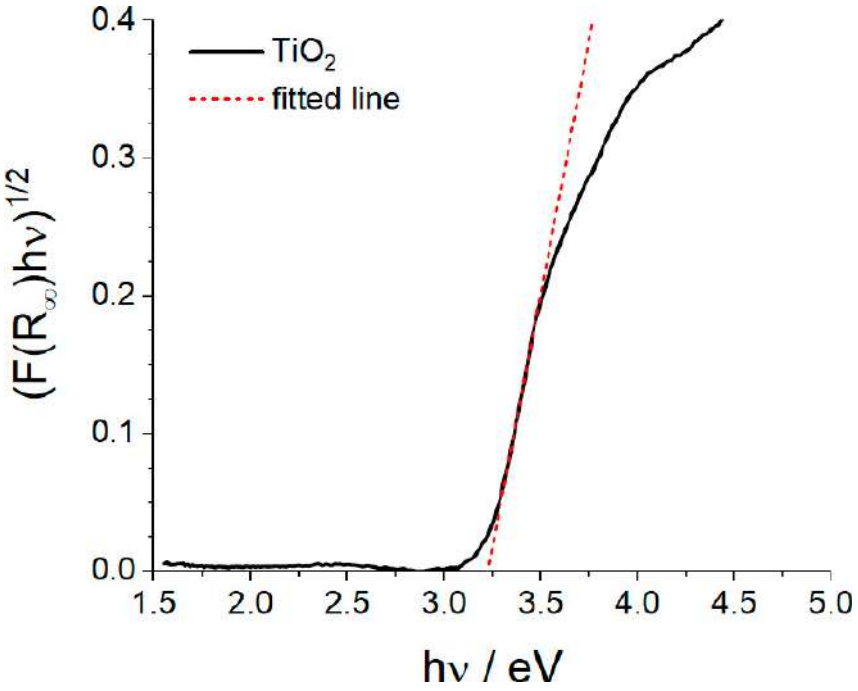

Figure 3.8 Shows the Tauc plots. Linear fits were extrapolated to the x-axis intercept from the plot to find the band gap energy values for each material [8].

if this method is applied to bulk materials or surface-modified materials with considerable absorbance at energies below E_g, the results may be considerably distorted. It is possible that all these modifications may introduce intraband gap states that can be observed in the absorption spectrum as additional broadband, also called the Urbach tail [8]. Its presence influences the Tauc plot, making it necessary to consider it when calculating the band gap energy. Directly applying the Tauc method to such a situation would result in an inaccurate estimation of E_g. In this study, UV-vis is used to identify band gap energies in experimental materials based on Tauc plots.

In the optical region, interference fringes of the transmission spectrum can be used to determine the thickness and linear refractive index. Suppose we have a film with thickness d, complex linear refractive index $n+ki$, and is deposited on a transparent substrate that has a thickness of several orders of magnitude greater than d and has an index of refraction n_s. When light passes through the film and the substrate wave interference occurs. In the case of consistent thickness d, interference effects produce a fringe spectrum shown in Figure 3.9, which can be used to calculate the optical constants of the film. The envelopes in Figure 3.9 illustrate how the maxima and minima transmissions(T_M, T_m) can be obtained as continuous functions of wavelength λ; therefore, thickness and refractive index can be calculated for each particular wavelength. The four major spectra regions are transparent, weak, medium, and strong. Through multiple

reflections, n and s determine the transmission in the transparent region ($\alpha = 0$). In the weak region of the spectrum, (α) tends to be small, which slightly reduces the transmission of light. The medium region has higher absorption coefficients and transmission decreases due to the effects of (α). By contrast, the transmission dramatically decreases in the region of high absorption almost solely due to the influence of (α). Whenever n is calculated in weak or medium transmission areas, it is necessary to obtain both the maxima and minima transmission values at at different wavelengths. An actual spectrum may not provide a reliable way of reading transmittance values from it, so the transmission values should be read from the curves of T_M and T_m at each wavelength. A sample's thickness can be determined by Equation 3.8, in which n_A and n_B denote the linear refractive indices at two adjacent maxima (or minima) at λ_1 and λ_2.

$$d = \frac{\lambda_1 \lambda_2}{2(\lambda_1 n_B - \lambda_2 n_A)} \tag{3.8}$$

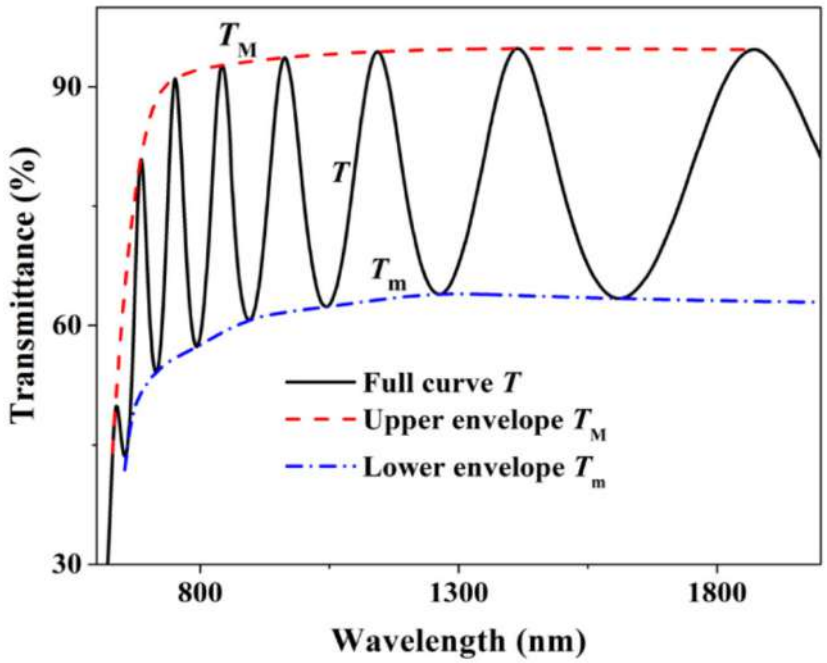

Figure 3.9 Transmission spectrum of α-S_i:H thin film on a glass substrate with upper and lower tangent envelopes [9].

3.6. z-scan technique

Sheik-Bahae et al. developed a nonlinear optical measurement technique, z-scan, based on the spatial distortion of a beam as the material is passed through its focus. This experiment requires

a single beam and is capable of measuring nonlinear refractive index and two-photon absorption simultaneously, and its simplicity makes it the most widely used technique today.

3.6.1. Principles

z-scan measurement, as its name suggests, is performed by moving the sample along the z-direction of a focused beam and measuring the intensity change of the transmitted beam. A typical z-scan setup is shown in Figure 3.10, where a neutral density filter is used to control the laser intensity and detectors to measure the incident beam power and transmitted powers. One of the detectors has a small aperture in front (closed aperture) and is sensitive to the signal containing information about nonlinear refraction and multi-photon absorption while the one without an aperture (open aperture) measures multi-photon absorption only.

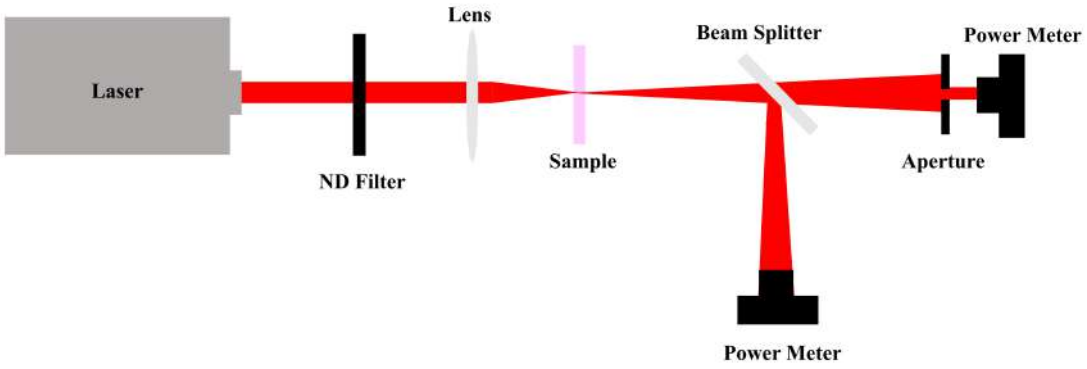

Figure 3.10 Schematic diagram of the experimental z-scan measurements.

Calculating the beam power transmitted through the aperture with radius r can be done by integrating the field strength $E(r,t)$ that passes through the aperture, Equation 3.9:

$$P_r(\phi_0(t)) = c\varepsilon_0 n_0 \pi \int_0^r |E_a(r,t)|^2 r dr. \tag{3.9}$$

Where c is the speed of light in free space, ε_0 is the permittivity of the vacuum, and n_0 is the refractive index. The phase change due to the self-action of the Gaussian beam is determined as:

$$\Delta\phi_0(t) = k\Delta n_2 L_{eff} \tag{3.10}$$

Where k is wave vector $k = 2\pi/\lambda$, $L_{eff} = (1-\exp(-L\alpha))/\alpha$, L_{eff} is effective sample thickness, L is the length of the material, α is linear absorption coefficient, Δn_2 is the change of

the refractive index $\Delta n_2 = n_2 I$. The transmission of the aperture is determined by the Equation 3.11:

$$T(z) = \frac{\int_{-\infty}^{\infty} P_r(\Delta\phi_0(t))dt}{S\int_{-\infty}^{\infty} P_i(t)dt} \tag{3.11}$$

Where $P_i(t) = \pi\omega_0^2 I_0(t)/2$ is the initial beam power incident on the material,
$S = 1 - \exp(-2r^2/w^2)$ is the linear transmission through the aperture, w the beam radius at the aperture in the linear propagation mode (in the absence of non-linearity), r is the aperture radius. In the open-aperture configuration $(S = 1)$, the transmission of the pulses with a Gaussian envelope is described by the Equation 3.12:

$$T(z, S = 1) = \frac{1}{\sqrt{\pi} q_0(z,0)} \int_{-\infty}^{\infty} ln(1 + q_0(z,0)\exp(-t^2))dt \tag{3.12}$$

Where $q_0(z,t) = \beta I_0(t) Leff/(1 + \frac{z^2}{z_0^2})$, z_0 is the diffraction length of an incident beam,
$I_0(t) = I(t, r = 0)$ is the instantaneous intensity of the pulse at the beam axis. If$|q_0| < 1$, the transmission can be represented as a series 3.13:

$$T(z, S = 1) = \sum_{m=0}^{\infty} \frac{[-q_0(z,0)]^m}{(m+1)^{3/2}} \tag{3.13}$$

If in this expression only the first two terms are taken, then one can obtain a simplified expression for $T_{open(z)}$ with an open aperture as 3.14:

$$T_{open(z)} = 1 - \frac{\beta I_0 L}{2\sqrt{2}(1 + x^2)} \tag{3.14}$$

For a closed aperture, the $T_{closed(z)}$ expression as:

$$T_{closed(z)} = 1 + \frac{4x(\Delta\phi_0)(1 - S)^{0.25}}{(1 + x^2)(9 + x^2)} \tag{3.15}$$

Where $x = z/z_0$, z_0 is the Rayleigh length.

Figure 3.11 is shows the a typical dependence of the transmittance as a function of position (z). In the thin medium approximation, for the Gaussian beam, the transmittance difference ΔT between the peak and the valley $n_2 < 0$ is given by the following Equation [125]:

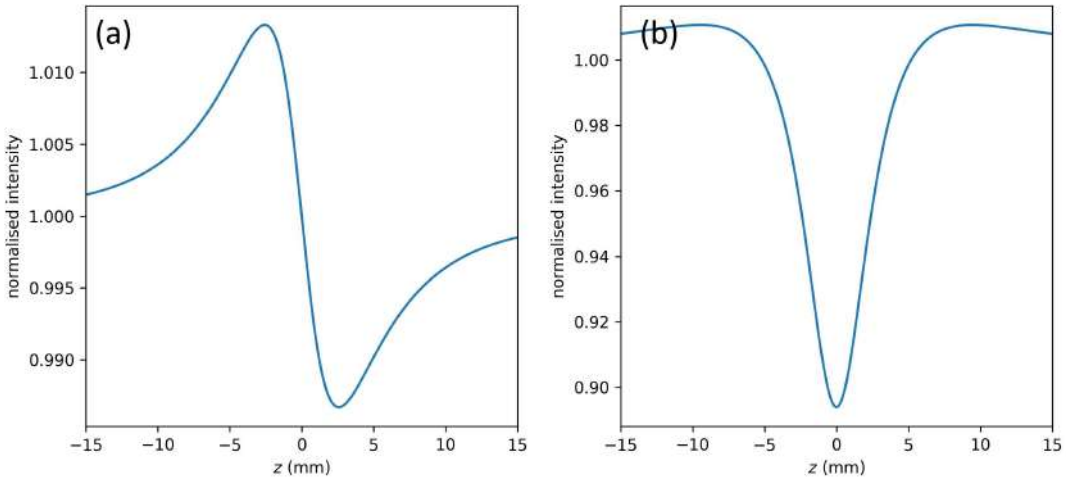

Figure 3.11 A typical result of a thin sample in z-scan measurement in a) the closed-aperture, b) the open-aperture configurations.

$$\Delta T = 0.406(1-S)^{0.25}|\Delta\phi_0| \tag{3.16}$$

Where ΔT is the transmittance energy difference between the peak and the valley, and $\Delta\phi_0$ is the nonlinear phase shift at focuse $(z=0)$.

The nonlinear refractive index and two-photon absorption coefficient can be extracted by fitting the experimental data with Equation 3.14 and 3.15.

3.6.2. Experimental setup and conditions

The z-scan setup is comprised of various components, a laser, a neutral density filter, a translation stage, two mirrors, two apertures, two beamsplitters and three power meters.

A 1060 nm laser (Spirit One, Spectra Physics) operating at 300 fs and 1 kHz is used for the measurement. The choice of wavelength depends on the material of interest and/or the spectral range that it is intended to be used in. In the case of studying the nonlinear optical properties at the resonant condition, the wavelength needs to match the bandgap energy of material, while a longer wavelength corresponding with less than half of the bandgap is desirable in the case of the non-resonant condition, in order to avoid two-photon absorption. 1060 nm is sufficiently long and suitable for most of the materials in this study. On some occasions where a shorter wavelength is needed, a 530 nm laser can be produced via a second harmonic generator. The pulse duration and repetition rate are kept short and low for the measurement. This is to avoid the thermal-optic effect induced by the laser, which would also lead to a similar shape of z-scan

trace as the nonlinear effect originating from bound electrons. The laser power, pulse duration and repetition rate can be controlled by software provided by the laser manufacturer. A continuously variable neutral density filter wheel is employed to further fine-tune the laser power, as the range between the power required for inducing nonlinear response and the power that causes optical damage could be small.

An aperture with a diameter of 3 mm ($d_{aperture}$), setting the beam input diameter to the lens, is placed behind the neutral density filter. The laser beam at this stage is split, with about 92% of the power continuing to the sample and 8% is directed to a reference power meter. This power meter is used to monitor the beam stability and the incident power throughout the measurement (P_{avg}). The reference power meter data can be used for background subtraction if there is any fluctuation in the laser power, which would also be visible in the z-scan traces.

As the laser beam follows the beam path, it reaches a convex lens, which focuses the beam onto the sample. Considering one of the assumptions of z-scan that the sample thickness is smaller than the Rayleigh length, a lens with a focal length of 75 mm is chosen as it yields a Rayleigh length of ≈ 1.6 mm (at 1060 nm), which is sufficiently long for both thin film and single crystal samples studied in this thesis. Depending on the wavelength (λ), a spot diameter (ω_o)and Rayleigh length (Z_R) can be calculated from the attributes of the lens and the laser intensity (I) can also be calculated by considering the pulse duration ($freq$) and repetition rate (τ). The intensity is a crucial information when extracting the third-order nonlinear refractive index and two-photon absorption coefficient. The following equation can be used to calculate the beam waist in a Gaussian beam:

$$2\omega_o = \frac{4\lambda f}{\pi d_{aperture}} \tag{3.17}$$

Where ω_0 is the minimum waist radius(smallest spot size) of the laser beam, f is the focal length of the lens and $d_{aperture}$ is the aperture diameter. This equation assumes a diffraction-limited Gaussian beam and is commonly used in laser optics and beam focusing application

In the equation below, the Rayleigh length (Z_R) of a laser beam is a parameter in optics that describes the distance over which a laser beam remains approximately collimated or focused.

$$Z_R = \frac{\pi \omega_o^2}{\lambda} \tag{3.18}$$

In laser systems, the following equation is commonly used to characterize and analyze power levels:

$$P_{peak} = \frac{P_{avg}}{\tau freq} \tag{3.19}$$

Where P_{peak} is the peak optical power of a light pulse or maximum power achieved during each pulse, $freq$ is the pulse duration, which is the time taken for each individual pulse, P_{avg} is the average power of the reference power meter, and τ is the repetition rat, which represent the number of pulses per unit time.

The intensity of a laser beam can be defined as the power per unit area delivered by the incident laser beam and can be calculated by applying the following equation:

$$I = \frac{P_{peak}}{\pi \omega_o^2} \tag{3.20}$$

The z-scan is done by moving the sample back and forth across the focal point of a laser beam, therefore a translation stage (Thorlabs DDS100/M) is employed for such motion. This motorised stage allows precise positioning control in µm scale with a traveling range of 10 cm. As the peak-to-valley distance is typically 1.7 times of the Rayleigh length [126], a scan range of 5 times of the Rayleigh length (with a step size of 0.2 mm) is chosen for the measurements in this study.

As the laser beam passes through the sample, the transmission power is split into two beams and measured by two power meters. The one without an aperture is called the open aperture scan. The measurement from this power meter is sensitive to the two-photon absorption. The one with a small aperture in front results in a closed aperture trace. This aperture acts as a spatial filter, and therefore the closed aperture trace is sensitive to both the nonlinear refractive and absorption. The motion and the data requisition from the three power meters are controlled by custom-built software.

Laser alignment is crucial in almost all optical systems. For the z-scan setup, this can be done by manoeuvring the two mirrors to direct the beam through the two apertures and achieve the maximum power available at the power meter with a closed aperture. To ensure the setup is

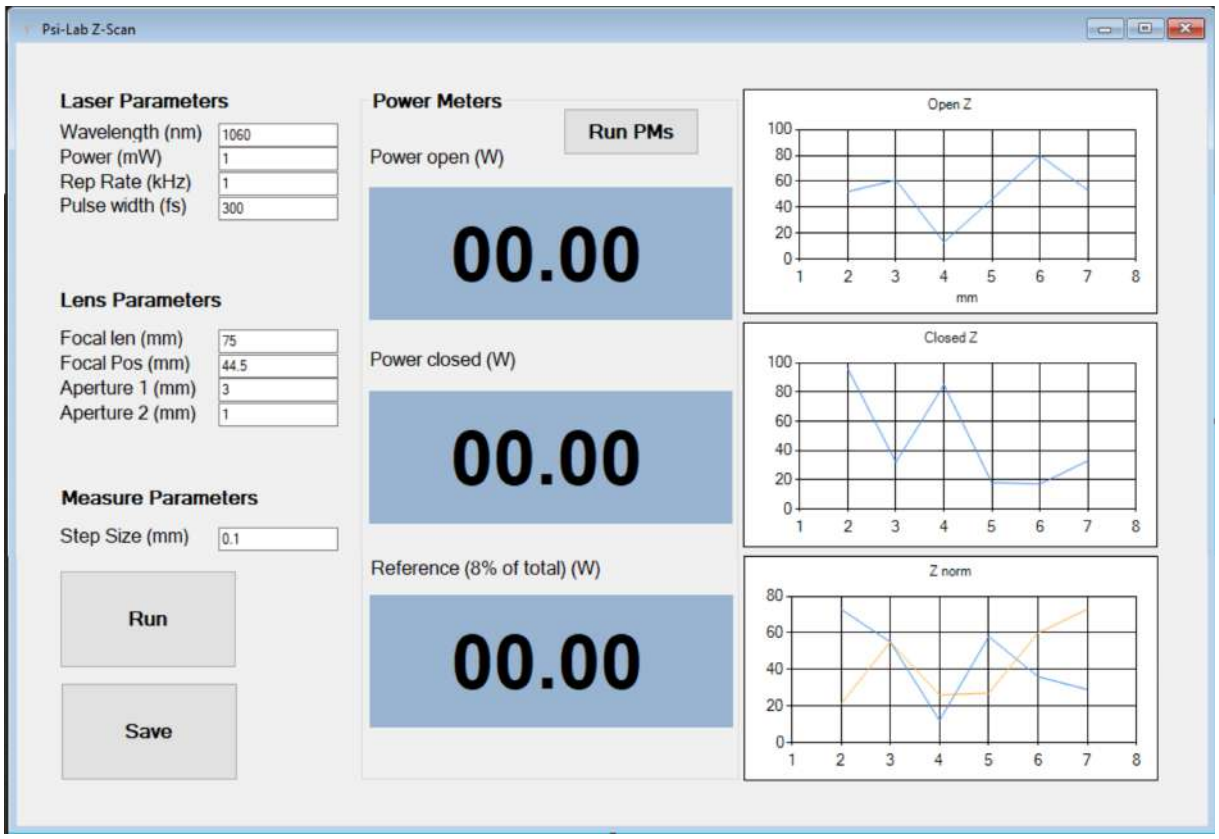

Figure 3.12 Software image displaying measurement parameters.

functioning and aligned properly, calibration of the setup is done using a microscope slide. A typical measurement of a microscope slide is presented in Figure 3.13. From this closed aperture trace, a nonlinear refractive index of $\approx 1 \times 10^{-20}\,\mathrm{m\,W^{-2}}$ can be extracted and it is close to the reported values in the literature [127], which indicates the setup is performing as expected. Since third-order nonlinear effects can be found in all materials, the response of substrate could overlay the material under study in the case of thin films, especially under high intensity. Therefore, it is equally important to understand the characteristics of the substrate. All thin film samples prepared for this thesis were deposited on a thin borosilicate coverslip glass ($\approx$ 0.15 mm thick), in order to minimise the response from the substrate.

3.6.3. Variations of z-scan

Several variations of z-scan have also been developed to serve different purposes [104]. For example, a two-colour z-scan (TC z-scan) was developed to measure non-degenerate third-order susceptibilities. This technique relies on the cross-phase modulation effect, in which the focusing and defocusing effect of a weaker beam is induced by a stronger beam with different colour [128] [129].

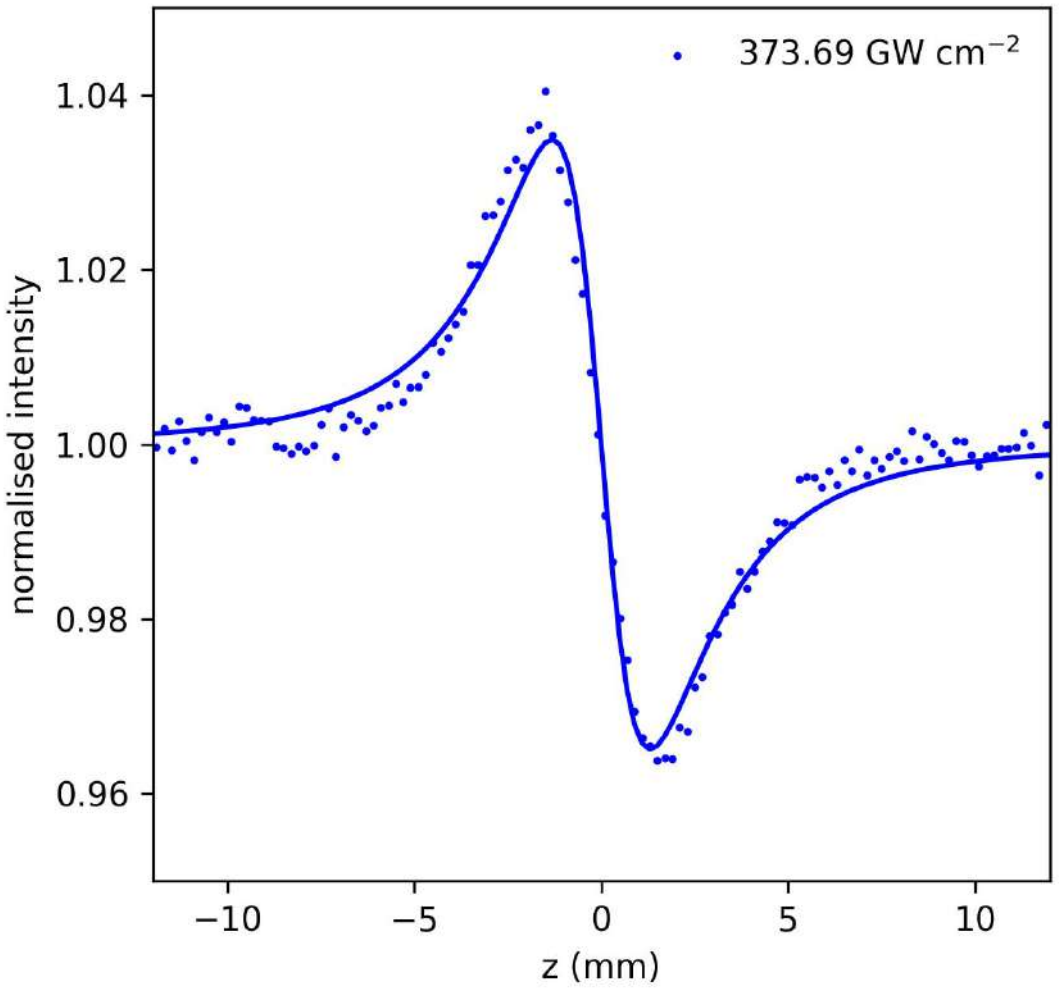

Figure 3.13 A typical result of a microscope slide in z-scan measurement in the closed-aperture configuration.

Another notable variation is reflection z-scan (Rz-scan). Since z-scan measures the intensity change of the transmitted beam, the sample needs to be transparent at the wavelength under study. In the case of the sample with a highly reflective surface or absorptive nature, using the reflection beam is an effective way to measure the nonlinear refractive index [130].

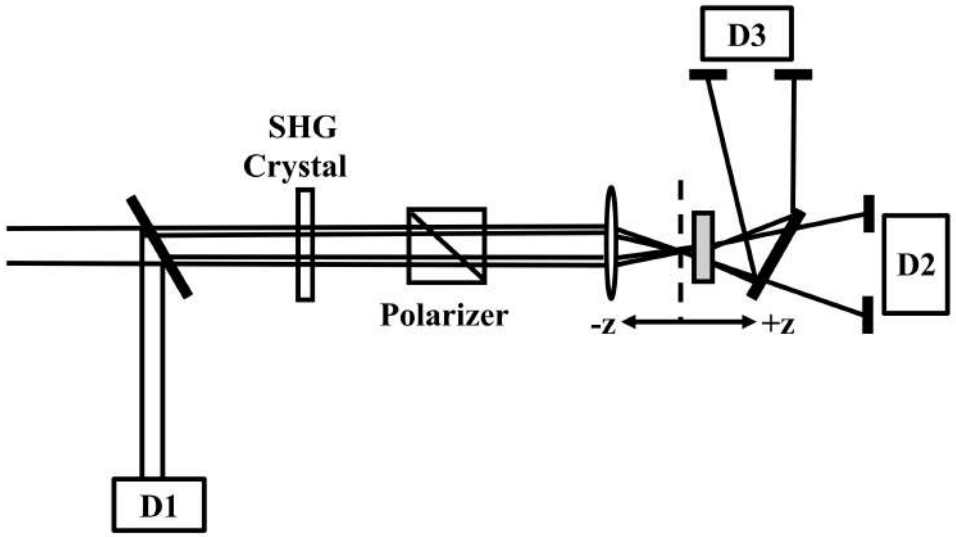

Figure 3.14 Configuration of a two-colour z-scan for measurement of nondegenerate nonlinearities.

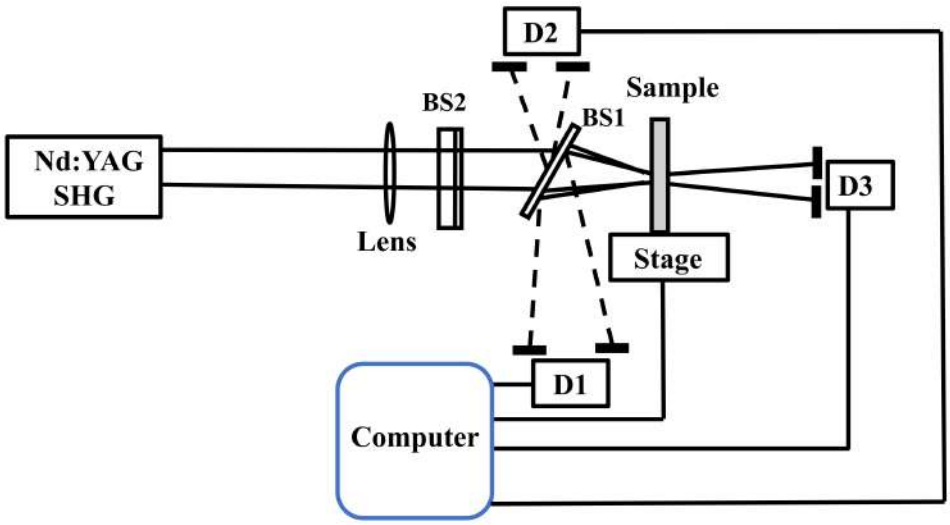

Figure 3.15 Experimental set-up for reflection z-scan techniques for measurements of optical properties of surfaces.

Chapter 4. Third-order nonlinear response of metal-halide perovskites films and single crystal

4.1. Introduction

The goal of this chapter is to investigate the third-order nonlinear response of metal-halide perovskite films and single crystal $MAPbX_3$ (X = I, Br, Cl), including their nonlinear refractive index and two-photon absorption coefficient. The literature indicates that the nonlinear optical properties of these materials are exceptionally high which makes them very attractive for the development of optical photonic devices. However, as stated in Chapter 2, the current literature in this field has many contradicting results with many orders of magnitude variations of the nonlinear refractive indices of each perovskite. This is likely to be a result of the measurement's sensitivity to instrumental and sample preparation errors. For example, using a substrate that is much thicker than the perovskite film can result in the measurement being dominated by the substrate or using laser parameters that allow heating of the sample can mean that the thermo-optic refractive index is being measured. In this chapter, a careful study of these materials is undertaken in order to address the issues in the literature and benchmark the materials for comparison and application in subsequent chapters. In order to minimise many of the pitfalls of the *z*-scan measurement, it was important to prepare samples that were of sufficient optical quality to produce high-quality results. For the fabrication of metal-halide perovskite films, a well-established one-step spin coating method was used. Optical quality single crystal growth is far more challenging as the surfaces of the crystal are often 'stepped' and scatter light precluding *z*-scan measurement. The inverse temperature crystallization (ITC) process was adopted, and a number of growing configurations were investigated in order to produce high optical quality single crystals.

4.2. Metal-halide perovskites thin films

This section details the preparation, characterisation, and z-scan measurement of thin films and single crystal of the metal-halide perovskites, $MAPbX_3$ (X = I, Br, Cl).

4.2.1. Precursor solution

Using well-established recipes, a precursor solution was made for each perovskite. The powders used to prepare these include PbI, PbBr, PbCl, MAI, MABr, and MACl. Lead Iodide (PbI_2, 99.99%), Lead Bromide ($PbBr_2$, 98.99%), and Lead Chloride ($PbCI_2$, 99.5%) were purchased from Tokyo Chemical Industry (TCI). Methylammonium iodide (MAI, 98%), Methylammonium bromide (MABr, 98%), and Mthylammonium chloride (MACl, 98%) were purchased from GreatCell Solar. A high-boiling point solvent is typically used to dissolve the precursor materials, such as γ-butyrolactone (GBL), N,N-dimethylformamide (DMF, 99.8%, extra dry), dimethyl sulfoxide (DMSO, 99.7%, extra dry). These solvents were purchased from Fisher Scientific.

4.2.2. Substrate preparation

In order to produce repeatable, uniform, and defect-free films for z-scan measurement, it is critically important to ensure that the substrate is clean and free from contamination. The substrates used for these experiments were borosilicate glass with a thickness of 150 µm and a length and width of 20 mm. The thin nature of these substrates was chosen to eliminate signal from the substrate during z-scan measurement. The substrates were cleaned with a 2% solution of Hellmanex in water and brushed with a coarse bristle brush. They were then sequentially rinsed with deionized water, acetone and ethanol and dried with compressed air. Using DI water helps to remove dust or other grain particles, acetone dissolves grease and organic particles, and it is water-soluble. The following ethanol cleaning process was used for removing the acetone solvent which contains organic particles. Finally, the substrate was treated in a plasma cleaner for 15 minutes to remove possible contaminants from the surface before the perovskite deposition.

4.2.3. One-step spin coating method

Each metal-halide perovskite thin film was produced using the well-established one-step spin coating method that was developed for prototyping solar cells. This protocol is amenable to the production of optical quality films and is described here.

$MAPI_3$

$MAPbI_3$ film was prepared as one-step solution process following a slightly modified procedure of that reported by [131]. The synthesized MAI 0.795 g was mixed with PbI_2 2.305 g in γ-Butyrolactone (GBL) 5 mL. The solution was stirred at 100 °C until dissolved; filtered using a 0.45 µL polytetrafluoroethylene (PTFE) filter to produce a crystal clear solution.
The substrate was loaded onto the vacuum chuck on the spin coater and was set spinning at 1000 rpm. A 50 µL of the $MAPbI_3$ solution was dropped onto the substrate and let spinning for 10 s before being sped up to 4000 rpm for 30 s. 300 µL of chlorobenzene (CB) was added and the substrate was let spin for a further 20 s to crystallise the perovskite. The coated substrate was removed from the vacuum chuck and dried at 100 °C for 10 min in a glovebox.

$MAPbBr_3$

$MAPbBr_3$ films were produced in a similar manner. A mixture of MABr 0.56 g and $PbBr_2$ 1.835 g was dissolved in 5 mL of N,N-dimethyl formamide (DMF) at room temperature; then, filtered with a 0.45 µL PTFE filter.
The substrate was loaded onto the vacuum chuck on the spin coater and was set spinning at 4000 rpm and 60 µL of the perovskite solution was drop cast onto the substrate and let spin for 10 s before increasing the rotation to 6000 rpm for 30 s. To crystallise the $MAPbBr_3$, 300 µL of CB was added and spun for 20 s. Finally, the samples were placed on a hot plate for annealing at 80 °C for 10 min in the glovebox.

$MAPbCl_3$

$MAPbCl_3$ solution was prepared by mixing MACl 0.34 g and $PbCl_2$ 1.39 g in a ratio (1:3) of N,N-dimethyl formamide and dimethyl sulfoxide (DMF:DMSO). $MAPbCl_3$ solution was stirred at 80 °C until dissolved; filtered using a 0.45 µL PTFE filter to produce crystal clear solution.

The substrate was loaded onto the vacuum chuck on the spin coater and was set spinning at 4000 rpm and 60 µL of perovskite solution was dropped onto the substrate and let spin for 10 s before increasing the rotation to 6000 rpm for a further 30 s. The perovskite was crystallised by adding 300 µL of CB and continuing the spinning for 20 s. Finally, the samples were placed on a hot plate for annealing at 80 °C for 10 min in glovebox.

4.3. Results and discussion of metal-halide perovskite thin films

4.3.1. Structural characterizations

Atomic force microscopy(AFM)

In optics measurements, including the *z*-scan, the optical quality of the material's surface is very important in order to limit surface scattering effects. This is particularly important for the *z*-scan technique as the variation in beam size as a function of position means that the scattering also varies as a function of position. The surface quality of the metal-halide perovskite films of $MAPbI_3$, $MAPbBr_3$, and $MAPbCl_3$ prepared via the spin coating protocols described in (4.2.3) were measured using an AFM. AFM measurements were performed in non-contact mode. Figure 4.1(a) shows a post-processed rendering of the $MAPbI_3$ and a surface roughness with a root mean square (RMS) of around 14 nm was determined. Figures 4.1 shows similar images for (b) $MAPbBr_3$ and (c) $MAPbCl_3$, whith each sample having a RMS roughness of 20 nm and 25 nm respectively. These results indicate that $MAPbI_3$ had a smoother surface than the other films, this may be the result of the $MAPbI_3$ film being dried at high annealing temperature (100 °C) as compared to other films that were annealed at 80 °C. The evaporation rate of organic and halide components is faster at higher annealing temperatures, resulting in uniform crystal and smooth surfaces. A statistical histogram composed of the post-processed image determined a mean grain size of 50 for the $MAPbI_3$, 83 for the $MAPbBr_3$, and 107 nm for the $MAPbCl_3$ as shown in Figure 4.3. In the light of these results, we can consider this information as the information that will set us on the right path to make a better optical measurement device. The annealing temperature typically controls the grain size and surface roughness of metal-halide perovskite films; as the annealing temperature increases, the grain size and surface roughness increase [132] [133]. In each instance, the samples had a mirror-like surface, as shown in Figure 4.2 and the surface roughness was at a level that negates the effect of scattering errors in

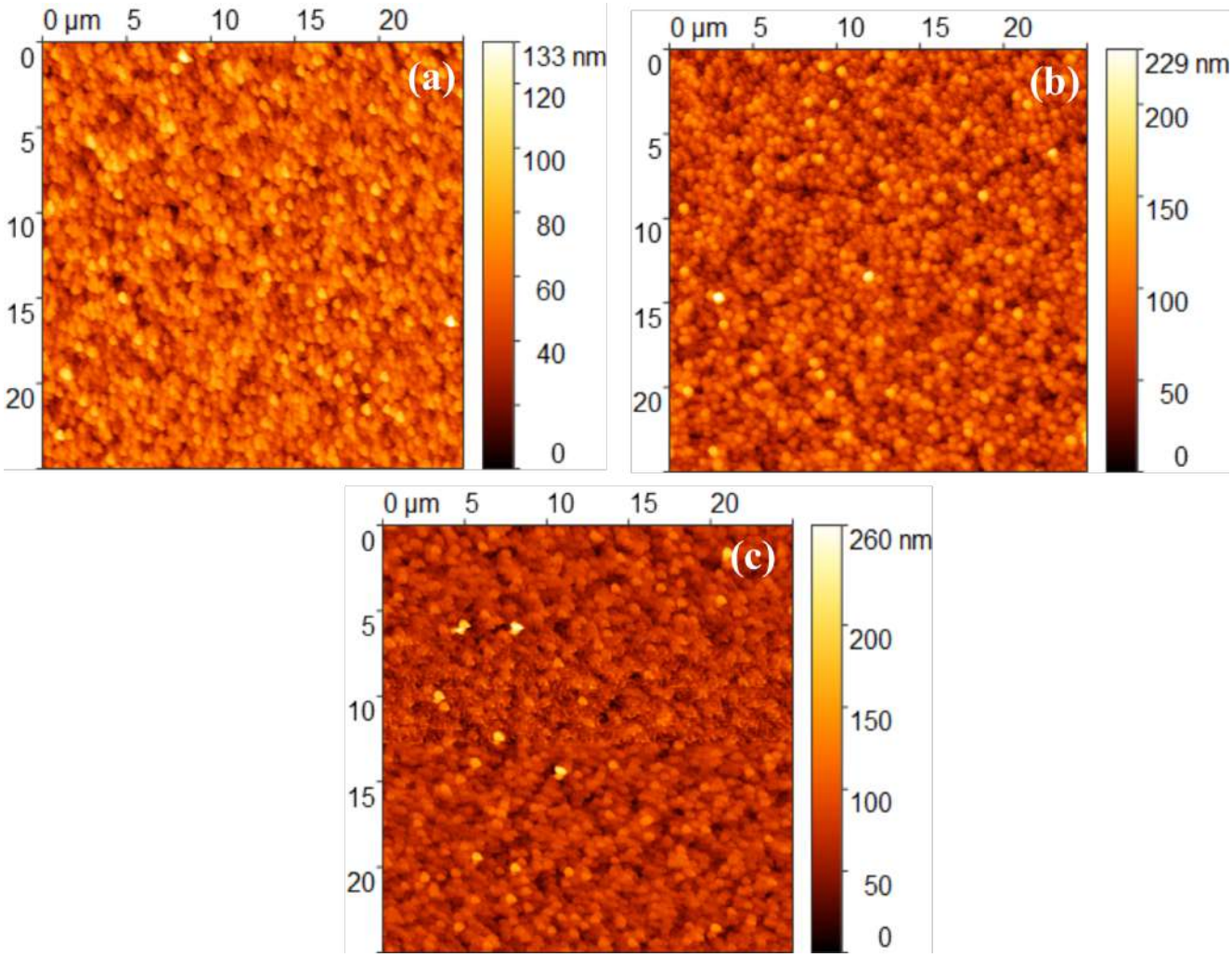

Figure 4.1 AFM images for metal-halide perovskites films a) $MAPbI_3$, b) $MAPbBr_3$, and c) $MAPbCl_3$ were deposited to a thickness of 500 nm.

the z-scan measurement. The AFM was also used to confirm the thickness of the deposited perovskite layers and each was $\sim$500 nm.

X-ray diffraction (XRD)

Each of the metal-halide perovskite films had its crystal structure measured using XRD. The measurements were undertaken using a Bruker D8 Advance diffractometer operating in the coupled $\theta/2\theta$ regime. The source of the X-rays is a copper (Cu) anode long fine focus ceramic X-ray tube. The X-ray tube is operated at a voltage of 40 kV and a current of 40 mA at a wavelength of 1.5406 Å. The mirror optic is used to produce a parallel beam of monochromatic X-ray radiation of dimensions up to 0.3 mm by 11 mm. The data has been compared with the standard database to confirm the crystal structure, all of the XRD peaks for the $MAPbX_3$ films correspond to the cubic phase (space group Pm-3m, COD ID # 7225287, COD ID # 4516751,

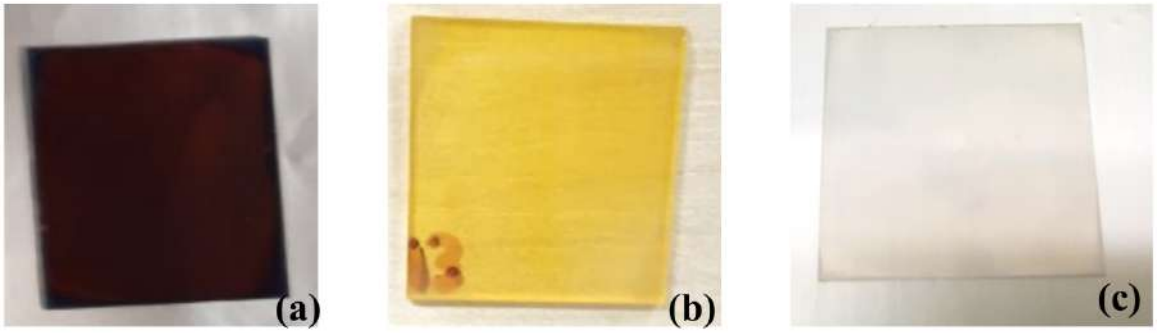

Figure 4.2 metal-halide perovskites films with highly reflective surfaces: a) $MAPbI_3$; b) $MAPbBr_3$; and c) $MAPbCl_3$.

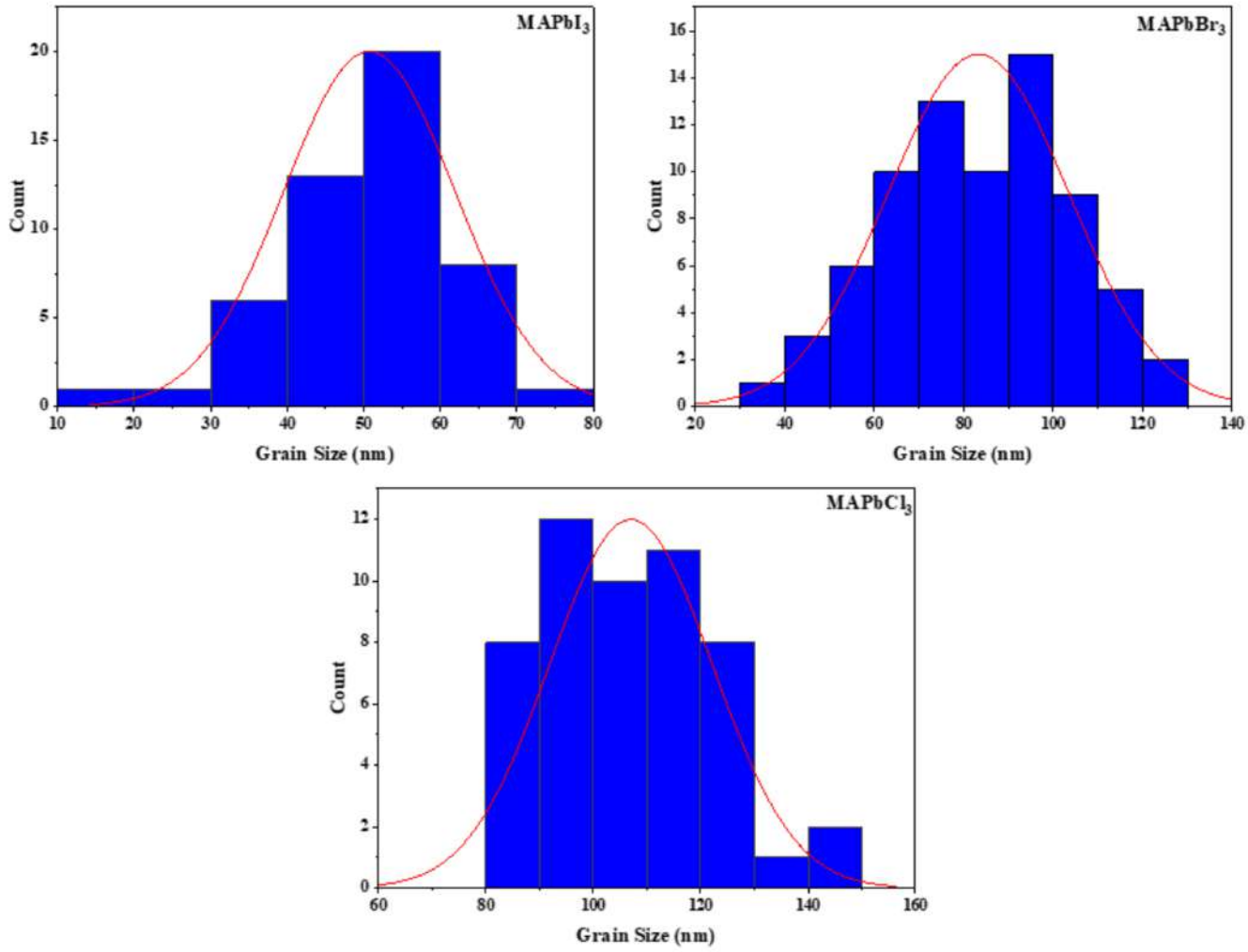

Figure 4.3 Grain Size distribution histogram of $MAPbI_3$; $MAPbBr_3$; and $MAPbCl_3$.

COD ID # 7231905) as shown in Figure 4.4 for (a) $MAPbI_3$, (b) $MAPbBr_3$, and (c) $MAPbCl_3$. The diffraction patterns show that no Pb(I_2, Br_2, Cl_2) phases, that can arise in spin coated $MAPbX_3$ film, were present indicating that the $MAPbX_3$ film were indeed representative of the desired phase. The full width at half maximum (FWHM) of the (100) plane for $MAPbI_3$ was 0.1713 µm indicating that the film was highly crystaline and low the in defects and microstrain that can occur in thin film samples. The FWHM for the $MAPbBr_3$ and $MAPbCl_3$ films were 0.261 µm and 0.364 µm, respectively, indicating similar film quality.

Furthermore, the lattice parameter was determined for each sample(a). In simple cubic crystal (SC), the lattice parameters are equal ($a = b = c$). Equation 3.3 was used to calculate lattice parameters. The calculated lattice parameters were a = 6.271 Å, 5.932 Å, and 5.686 Å for $MAPbI_3$, $MAPbBr_3$, and $MAPbCl_3$, respectively. The values for a and the interplanar spacings were compared to the literature [134], and, indeed, they are in agreement; indicating that the materials are of high crystalline quality and of the one desired phase.

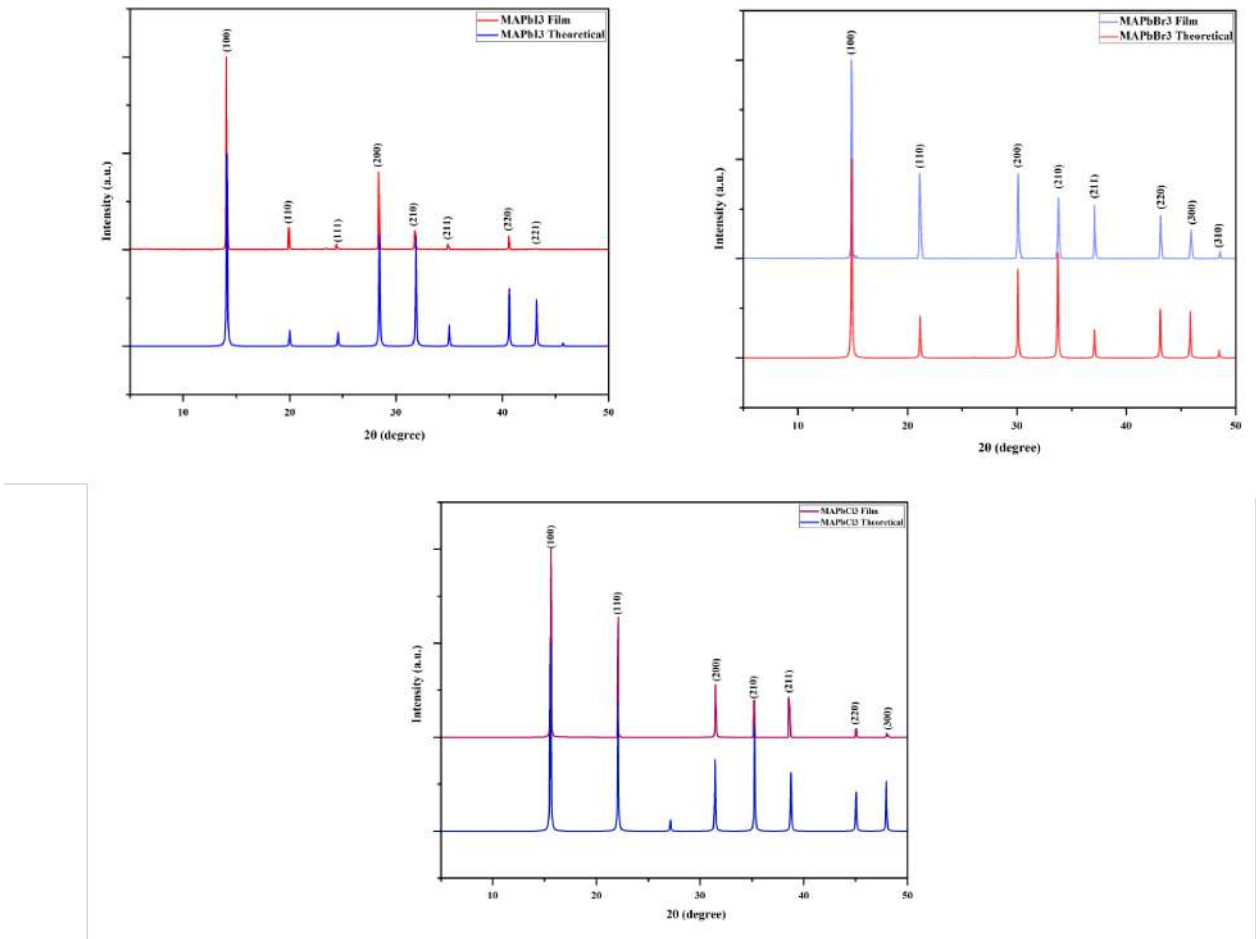

Figure 4.4 Diffraction patterns for (a) $MAPbI_3$, (b) $MAPbBr_3$, and (c) $MAPbCl_3$.

Interplanar distance d(Å) of $MAPbI_3$		
Plane (*hkl*)	2θ(°) Experimental	d(Å) Experimental
(100)	14.08	6.28
(110)	20.03	4.43
(111)	24.57	3.62
(200)	28.41	3.14
(210)	31.81	2.81
(211)	35.06	2.56
(220)	40.61	2.22
(221)	43.41	2.08

Table 4.1 Calculated X-ray diffraction parameters of cubic $MAPbI_3$.

Interplanar distance d(Å) of $MAPbBr_3$		
Plane (*hkl*)	2θ(°) Experimental	d(Å) Experimental
(100)	14.88	5.95
(110)	21.14	4.19
(200)	30.12	2.96
(210)	33.85	2.64
(211)	37.08	2.42
(220)	43.24	2.09
(300)	45.76	1.98
(310)	48.48	1.88

Table 4.2 Calculated X-ray diffraction parameters of cubic $MAPbBr_3$

Interplanar distance d(Å) of $MAPbCl_3$		
Plane (*hkl*)	2θ(°) Experimental	d(Å) Experimental
(100)	15.59	5.68
(110)	22.15	4.01
(200)	31.53	2.83
(210)	35.26	2.54
(211)	38.76	2.32
(220)	45.05	2.01
(300)	47.98	1.89

Table 4.3 Calculated X-ray diffraction parameters of cubic $MAPbCl_3$

4.3.2. Optical characterizations

z-scan measurements

The z-scan instrument developed and calibrated in Chapter 3 was used to measure the accurate determination of the third-order nonlinear optical properties of the metal-halide perovskite films. The z-scan process allows for both the nonlinear absorption, β, and refraction, n_2, of the films to be measured simultaneously. In the first instance, the closed aperture method was used to measure the real part of the nonlinear refractive index (n_2). The open-aperture configuration measures just the nonlinear absorption of the sample β. Through plasma dispersion and thermal lensing, this absorption can change the refractive index of the material. In this work, the repetition rate of the laser was set at 1 kHz, and the pulse duration was set to 300 fs. Closed and open aperture z-scan measurements were taken of the $MAPbI_3$, $MAPbBr_3$, and $MAPbCl_3$. The closed aperture measurements are presented in Figure 4.5, and it is obvious that the $MAPbI_3$ sample show the 'valley-peak' signal while $MAPbB_3$ and $MAPbCl_3$ samples show the 'peak-valley' signal that is typical of nonlinear refraction. This flipping of the sign of the nonlinear refractive index is expected as the bandgap energy of the $MAPbI_3$ (1.5 eV) is close to the energy of a photon of the laser source (1.2 eV). The nonlinear refractive index can be extracted by fitting the z-scan trace with Equation 4.1 [135] [136]. Here z is the scan distance from the focal point, z_0 the Rayleigh length of the focusing lens, S the aperture transmittance (S = 0.13 for closed aperture, S = 1 for open aperture), L_{eff} the effective sample thickness, I_0 the intensity at the focus, and λ the incident wavelength (1060 nm). The fittings are also shown in Figure 4.5 and the values returned for the n_2 were $5.8 \times 10^{-17}\,m^2\,W^{-1}$ for the $MAPbI_3$, $3.8 \times 10^{-17}\,m^2\,W^{-1}$ for the $MAPbBr_3$ and $5.8 \times 10^{-18}\,m^2\,W^{-1}$ for the $MAPbCl_3$, which is an order of magnitude greater for the $MAPbI_3$ (Table 4.4). When considering these materials, the nonlinear refractive index of $MAPbI_3$ is about 2 times higher than that of $MAPbBr_3$, while it is about 10 times higher than $MAPbCl_3$ (Table 4.4). Under high intensity conditions, it is thought that electrons of a larger anion are more susceptible to being affected by incident lasers and therefore respond more strongly. The traces obtained from the open-aperture z-scan show a strong nonlinear absorption coefficient of $MAPbI_3$ and $MAPbBr_3$ (Table 4.4). The two photon absorption of $MAPbI_3$ is about 10 times higher than that of $MAPbBr_3$, while the $MAPbCl_3$ sample shows no evidence of multiphoton absorption, and the β was effectively zero the sample.

Materials	n_2 ($m^2 W^{-1}$)	β ($m W^{-1}$)	FOM_{nl}	Band gap (eV)	ref
$MAPI_3$	5.8×10^{-17}	1.2×10^{-9}	0.05	1.5	[139]
$MAPBr_3$	3.8×10^{-17}	5.3×10^{-10}	0.35	2.18	[140]
$MAPCl_3$	5.8×10^{-18}	1×10^{-13}	>54	2.9	[139]

Table 4.4 Optical properties of metal-halide perovskites films

This is expected, as $MAPbCl_3$ films have a band gap of 2.9 eV, they have a higher band gap than $MAPbI_3$ and $MAPbBr_3$ which means that no two-photon absorption at the corresponding energy of the laser wavelength 1.17 eV.

The values of nonlinear refractive index and two-photon absorption presented here differ from those published in literature [69] [73] [68] [66] [70] [82]. The discrepancies in the results in the literature are likely owing to poor choice in laser parameters chosen that allow sample heating resulting in the measurement of thermo-optics nonlinear properties. To avoid thermal effects on nonlinear response, our measurements were performed at low powers and in the femtoseconds regime. Additionally, the substrate was thinner than the perovskite film (150 µm) which allowed us to obtain accurate results from the perovskite film instead of the substrate.

The efficiency of nonlinear refraction is reduced when the nonlinear absorption is strong. Thus, a material's potential for nonlinear applications depends on the balance between both parameters. The nonlinear figure of merit FOM_{nl} can be used to compare different materials for nonlinear applications at a particular wavelength. It is given by Equation 4.2 [137] [138]. The FOM_{nl} values for the materials the $MAPbI_3$, $MAPBr_3$, and $MAPbCl_3$ are presented in Table 4.4. $MAPbCl_3$ materials have the greatest value of FOM_{nl} as it has the widest-band-gap. The detection limit was used for the upper limit of the nonlinear absorption for this material.

$$T = 1 - \frac{8\pi}{\lambda\sqrt{2}} \frac{(z/z_0)(1-S)^{0.25} L_{eff} n_2 I_0}{(1+(z/z_0)^2)(9+(z/z_0)^2)} + \frac{1}{2\sqrt{2}} \frac{\beta L_{eff} I_0 (z/z_0)^2}{(1+(z/z_0)^2)(9+(z/z_0)^2)} \tag{4.1}$$

$$FOM_{nl} = \frac{n_2}{\beta\lambda} \tag{4.2}$$

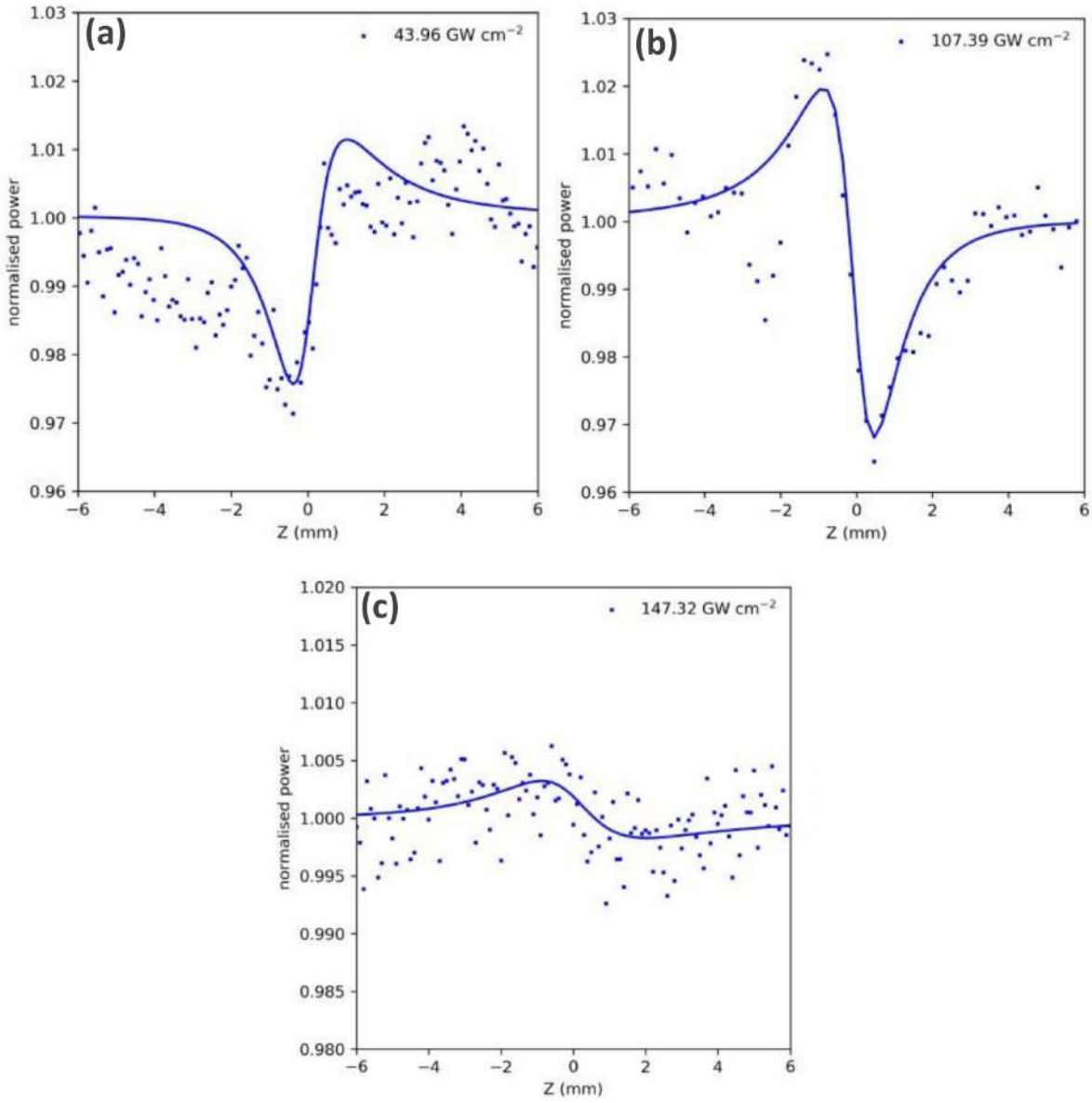

Figure 4.5 Closed-aperture z-scan of (a) $MAPbI_3$, (b) $MAPbBr_3$ and (c) $MAPbCl_3$.

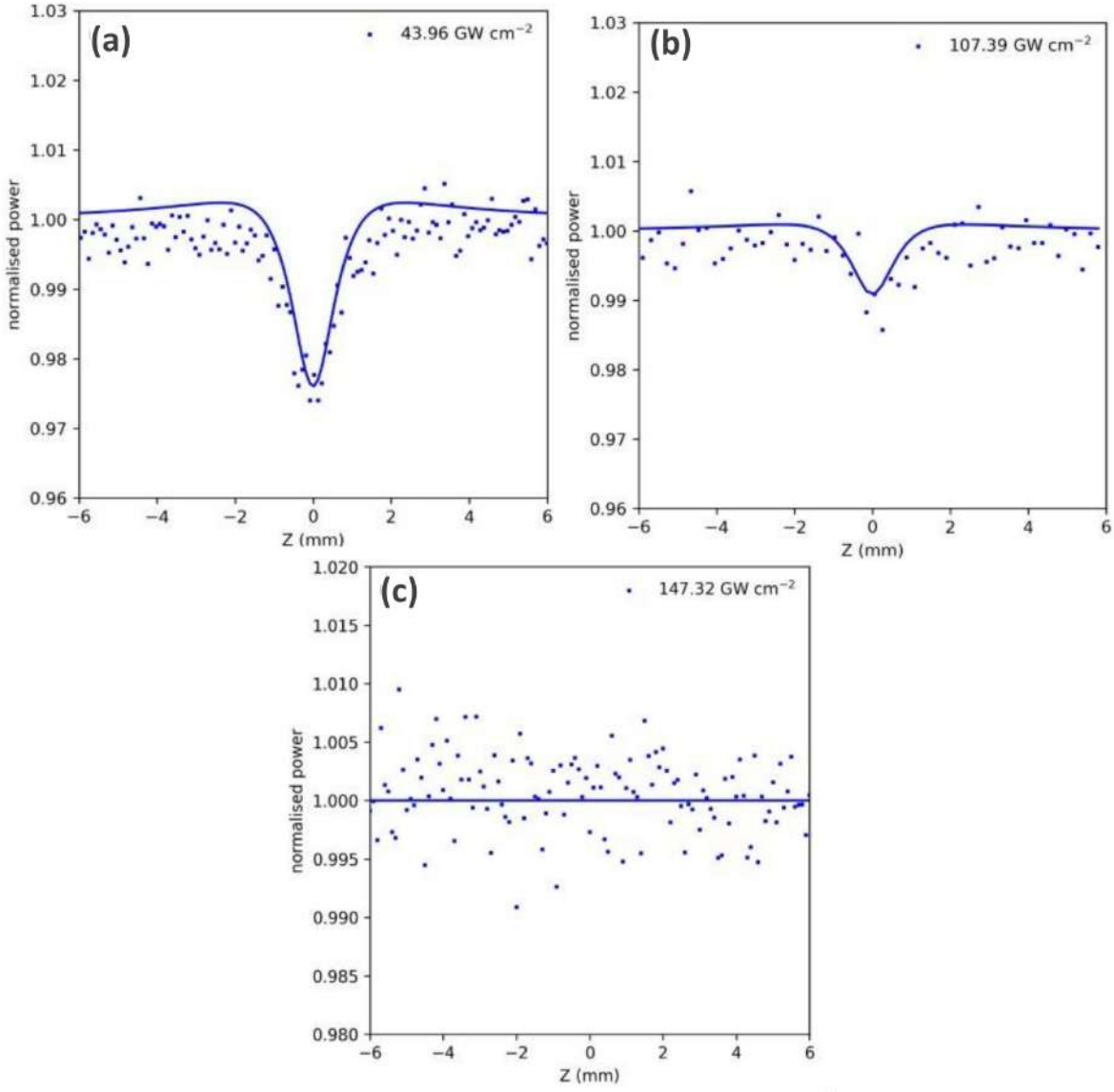

Figure 4.6 Open-aperture *z*-scan of (a) $MAPbI_3$, (b) $MAPbBr_3$, and (c) $MAPbCl_3$.

4.4. Metal-halide perovskites single crystal

Perovskite single crystals with remarkable photoelectric and optoelectronic properties have been hailed as a possible replacement for silicon due to their low defect density and absence of grain boundaries [55] [141] [57]. Single crystals have excellent properties, such as high carrier mobility [142], long carrier diffusion lengths, and long carrier lifetimes [55] [57] [143], which make them more suitable for solar cells [143], photodetectors (PDs) [144], light emitting diodes (LEDs), and lasers [145] [146]. With these properties, $MAPbX_3$ single crystals are highly desirable for optoelectronic applications compared to polycrystalline thin films. In addition, metal-halide single crystals are preferred for nonlinear optical applications as they typically have sharper band-edges and have minimal scattering losses when transmitting light. In the following sections, a number of methods are used to produce single crystals that are amenable for nonlinear optics applications.

4.4.1. Inverse temperature crystallization (ITC)

The $MAPbX_3$ perovskites exhibit inverse temperature solubility behaviour in certain solvents, so this novel phenomenon in metal-halide perovskites enabled the rapid growth of high-quality size and shape-controlled single crystal of $MAPbX_3$ at a rate that is an order of magnitude faster than that achieved by other growth methods within the literature [55] [147] [148] [149]. Following the procedure outlined in [61] [150] single crystals of the $MAPbX_3$ (X= I, Br, Cl) were grown and these are shown in Figure 4.7.

ITC growth of $MAPbI_3$

The synthesized MAI (1.59 g) was mixed with PbI_2 (4.61 g) in GBL (10 mL). The solution was stirred at 100 °C until totally dissolved and became transparent; filtered using a (0.45 µL) PTFE filter to produce clear solution; placed in a new vial and kept in an oil bath at 110 °C until $MAPbI_3$ single crystal formed. $MAPbI_3$ perovskite single crystals were removed from the vials after they formed and dried on both sides using cleanroom wipes and a nitrogen gun.

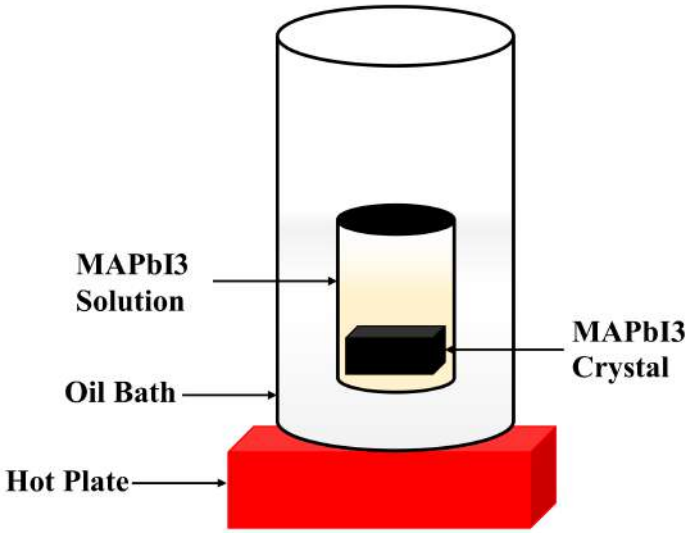

Figure 4.7 Schematic representation of the ITC apparatus in which the crystallization vial is immersed within a heating bath. The solution is heated and kept at an elevated temperature (95 °C, 80 °C, and 60 °C for $MAPbI_3$, $MAPbBr_3$, and $MAPbCl_3$) to initiate the crystallization.

ITC growth of $MAPbBr_3$

A mixture of MABr (1.12 g) and $PbBr_2$ (3.67 g) was dissolved in 10 mL of DMF at room temperatur until totally dissolved and became transparent; then, filtered with a (0.45 µL) PTFE filter; placed in a new vial and kept in an oil bath at 80 °C untill $MAPbBr_3$ single crystal formed. The single crystals of $MAPbBr_3$ perovskite were removed from the vials after they had formed and dried on both sides with cleanroom wipes and a nitrogen gun.

ITC growth of $MAPbCl_3$

To prepare $MAPbCl_3$ single crystal, 0.2228 g of MACl was added to 3.3 mL of DMSO:DMF (1:1) solution; put the mixture in an ultrasonic bath at room temperature for 10 min until the MACl is completely dissolved. This was followed by adding 0.8343 g of $PbCl_2$ to 3 mL MACl/DMSO:DMF solution and it was stirred for 20 min until the solution became transparent. A PTFE syringe filter (0.45 µL) was used to filter $MAPbCl_3$ solutions; placed in a new vial and kept in an oil bath at 50 °C till $MAPbCl_3$ single crystal formed. After the single crystals of $MAPbCl_3$ perovskite had formed, they were removed from the vials and dried on both sides with cleanroom wipes and a nitrogen gun. All procedures were carried out in a glovebox under nitrogen.

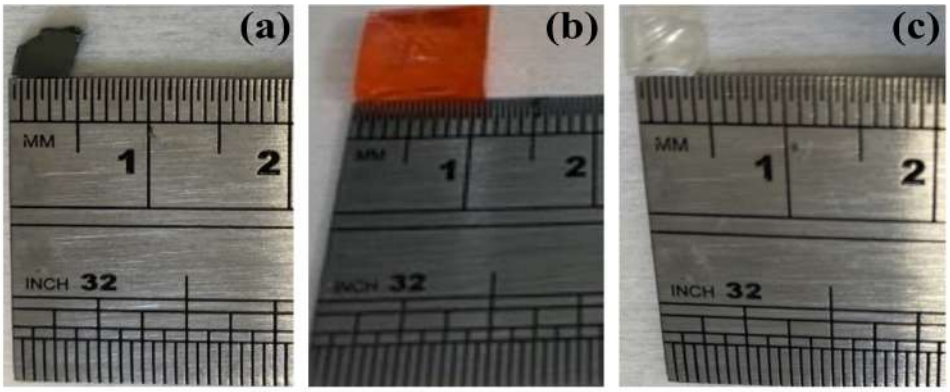

Figure 4.8 (a) $MAPbI_3$, (b) $MAPbBr_3$, and (c) $MAPbCl_3$ crystal growth by inverse temperature crystallization (ITC) method for nonlinear application.

4.4.2. Results and discussion of crystals grown using the ITC method

Figures 4.8 show the single crystal of $MAPbX_3$ synthesized using ITC method. In the precursor solution of the metal-halides perovskites, many individual crystals were formed, but all were too thick for *z*-scan measurement. A $MAPbI_3$ crystal was approximately 4x4 mm, as compared with a $MAPbBr_3$ crystal about 1x1 cm and a $MAPbCl_3$ crystal about 4x4 mm. A microscope images for each perovskite sample are shown in 4.9 a. It can be seen that in all cases, the single-crystal surfaces contain defects like holes and plane stepping. These defects again precluded the samples from *z*-scan interrogation. In order to improve the surface quality and reduce the sample thickness, Kemet PSU-M cloths, a chemical textile cloth of medium hardness, with a diameter of 15" and thickness of 380 mm, were used for chemical mechanical polishing with organic solvents such as DMF and DMSO. $MAPbX_3$ samples of the polished surfaces are presented in Figure 4.9b and it is clear that the polishing process produced some artefacts on the crystal surfaces (e.g. cracked or scratched surfaces). Owing to these results an alternative approach to crystal growth was examined.

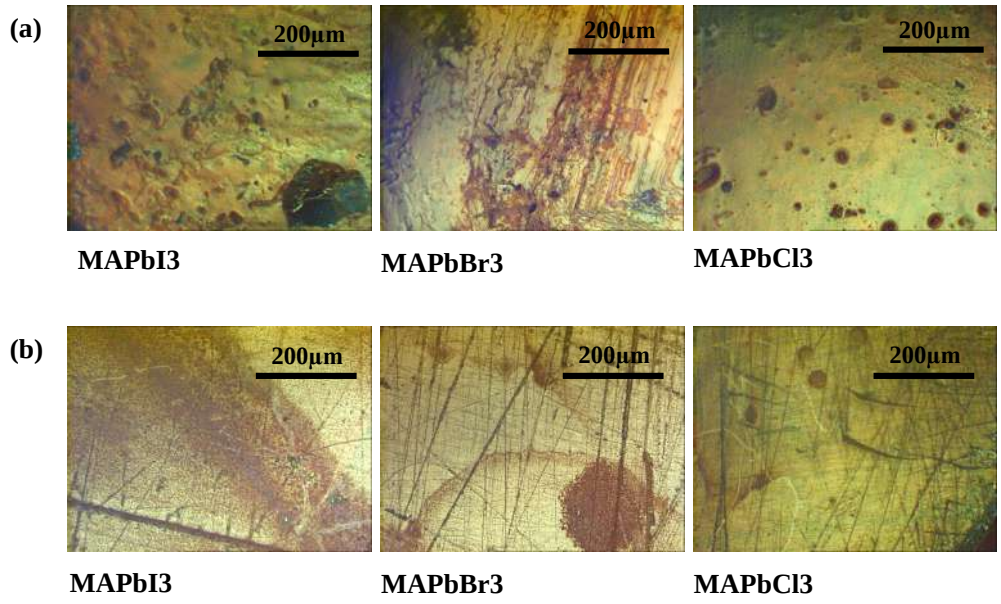

Figure 4.9 Microscopic images of metal-halide perovskites single crystal formed with the ITC method a) before and b) after chemical polishing using a Kemet PSU-M cloth.

4.4.3. Growth between silicon wafers.

In order to constrain the crystal growth in one direction and to grow crystals with smooth surfaces, crystal growth was promoted between two silicon wafers. Silicon wafers were selected for their smooth surfaces, as silicon wafers typically have a surface roughness of the order of 10 nm.

Preparation of silicon wafer and precursor solution.

Silicon wafers were used with a thickness of 0.68 mm and a diameter of 2.5 cm, they were cleaned with deionized water, acetone, and ethanol, and then dried using compressed air. For the perovskite solutions, the same procedures were followed as used in the ITC method.
Single crystals of $MAPbX_3$ (X = I, Br, Cl) between two silicon wafers, using a modified approach to that described by [151]. Typically, two silicon wafers were separated and aligned in parallel by two spacers of thin glass with a thickness of 200 µm to control the single crystal thickness.

Silicon wafer constrained growth of single crystal $MAPbI_3$

The synthesized MAI (1.59 g) was mixed with PbI_2 (4.61 g) in GBL (10 mL). The solution was stirred at 100 °C until totally dissolved and became transparent; filtered using a (0.45 µL) PTFE filter to produce clear solution. The silicon wafer slides were dipped into a 8 mL glass jar that was filled with the $MAPbI_3$ solution. After that, the glass jar was placed on a hot plate at 100 °C for perovskite solutions to start the crystalization. After the single crystals had formed between the silicon wafer, they were removed from the jar and dried using clean room wipes and a nitrogen gun.

Silicon wafer constrained growth of single crystal $MAPbBr_3$

A mixture of MABr (1.12 g) and $PbBr_2$ (3.67 g) was dissolved in 10 mL of DMF at room temperatur until totally dissolved and became transparent; then, filtered with a (0.45 µL) PTFE filter. A 8 mL glass jar filled with the $MAPbBr_3$ solution was used to dip the silicon wafers. The glass jar was then placed on a hotplate at 80 °C for $MAPbBr_3$ solutions to begin crystallizing. Once a single crystals had formed between the silicon wafers, they were removed from the jar and dried using clean room wipes and a nitrogen gun.

Silicon wafer constrained growth of single crystal $MAPbCl_3$

To prepare $MAPbCl_3$ single crystal between silicon wafers, 0.2228 g of MACl was added to 3.3 mL of DMSO:DMF (1:1) solution; put the mixture in an ultrasonic bath at room temperature for 10 min until the MACl is completely dissolved. This was followed by adding 0.8343 g of $PbCl_2$ to 3 mL MACl/DMSO:DMF solution and it was stirred for 20 min until the solution became transparent. A PTFE syringe filter (0.45 µL) was used to filter $MAPbCl_3$ solutions. For dipping the silicon wafers, a 8 mL jar containing the $MAPbCl_3$ solution was used. The glass jar was then placed on a hotplate at 60 °C for $MAPbCl_3$ solutions to begin crystallizing. The silicon wafers were removed from the jar once a single crystals had formed and the crystals dried using clean room wipes and a nitrogen gun. The method used to grow the single crystal between silicon wafer is shown in Figure 4.10.

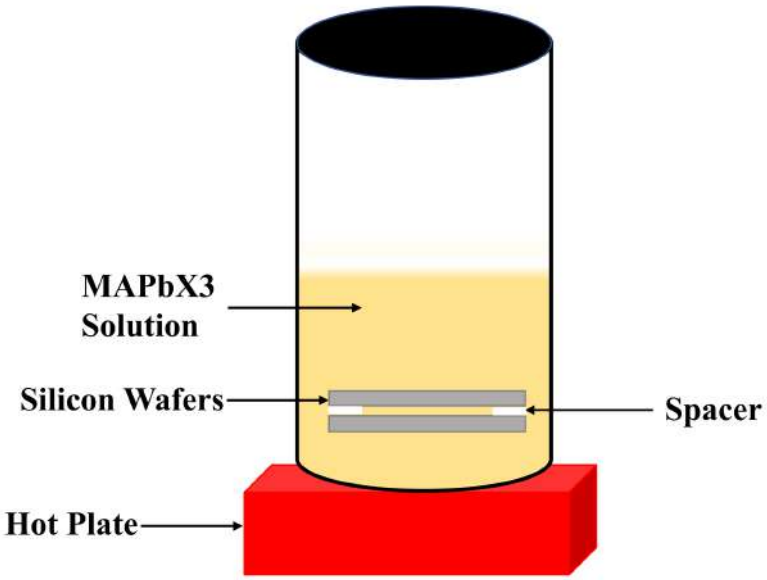

Figure 4.10 Schematic illustration of two silicon wafer separated by two spacers to form a single crystal.

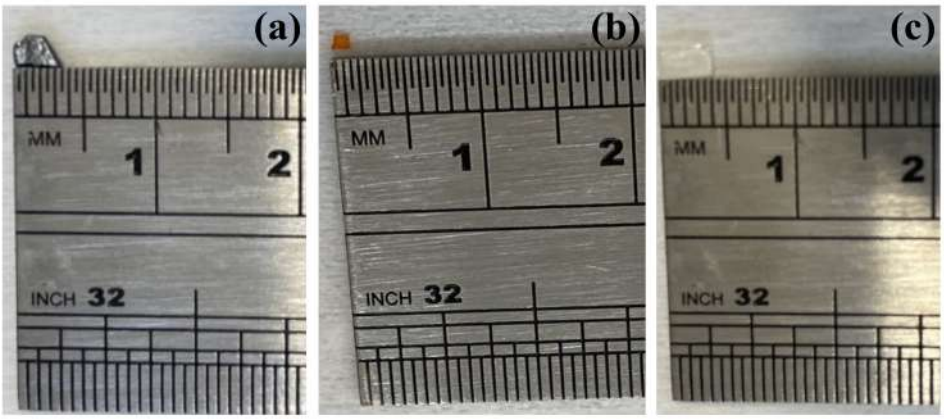

Figure 4.11 Growth of single crystal of metal-halide perovskites (a) $MAPbI_3$, (b) $MAPbBr_3$, and (c) $MAPbCl_3$ between two silicon wafers.

4.4.4. Results and discussion of crystals grown between silicon wafer

Figures 4.11 show the single crystals of $MAPbX_3$ synthesized using crystal growth between silicon wafer. The $MAPbI_3$ crystal was approximately 3x3 mm, whereas the $MAPbBr_3$ crystal was about 1x1 mm and the $MAPbCl_3$ crystal was approximately 4x4 mm. Considering that all crystals were thinner than the crystals formed by ITC but the quality of the surface was poor as shown in Figure 4.12a. Kemet PSU-M cloths were used to polish crystals surface, but it is clear that the process produced some scratches on the crystal surfaces that hindered with optical measurements as can be seen in Figure 4.12b, so we moved to grow the crystal using an IR-cell method in order to control the crystal thickness and obtain high surface quality.

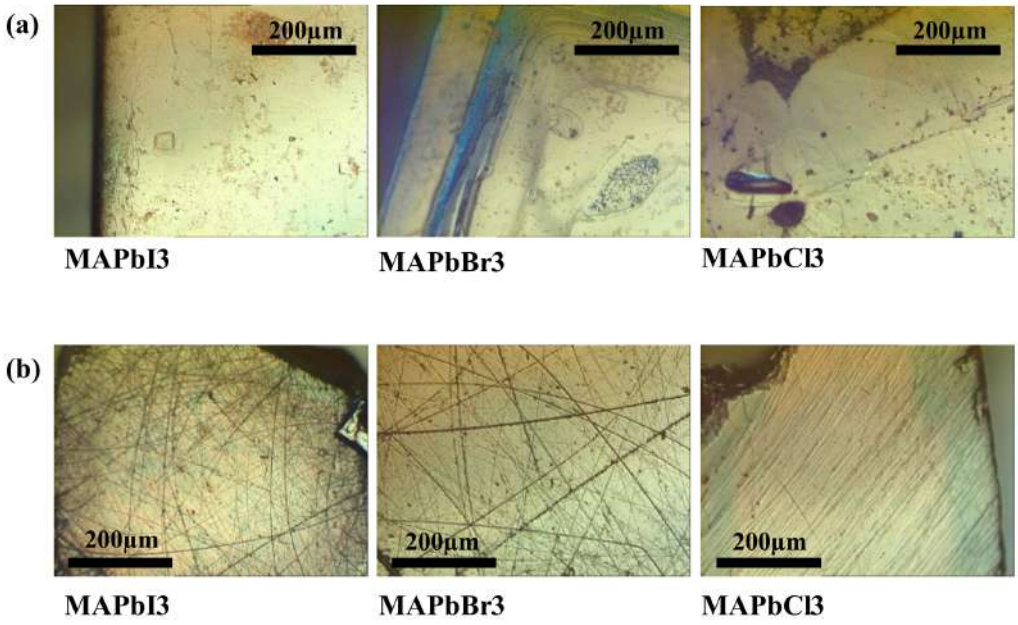

Figure 4.12 Microscope images of single crystal of metal-halide perovskites grown between silicon wafers, a) before chemical polishing, b) after chemical polishing with Kemet PSU-M cloth.

4.4.5. Growth in IR-cell

The main goal of this method was to control the crystal thickness and to improve the quality of the single crystal surface by keeping the perovskite solution fresh within the cell. This method was considered to be the most effective since it provided a smooth fresh surface without requiring chemical polishing, as shown in Figure 4.15.

IR-cell growth of single crystal $MAPbBr_3$

For the remainder of this study, the focus was put on growing high-quality $MAPbBr_3$ crystals as it grows from solution more readily and has greater potential for nonlinear optics applications owing to its wider bandgap than $MAPbI_3$ and stronger nonlinear response than $MAPbCl_3$. A mixture of MABr (2.24 g) and $PbBr_2$ (7.34 g) was dissolved in 20 mL of DMF at room temperature until they totally dissolved and the solution became transparent. The solution was then filtered with a (0.45 µL) PTFE filter.

As shown in Figure 4.13, two metal plates were used and position them in parallel, a silicon rubber spacer was used to separate them. For control of the thickness of the $MAPbBr_3$ single crystal inside the silicon rubber, we used a spacer thickness of 0.1 mm, as shown in Figure 4.14. The perovskite solution was poured into a syringe, and it was connected with a syringe pump. A

constant flow (0.1 cc/HR) of fresh solution was maintained using the syringe pump, which allowed one to attain single crystals from fresh perovskite solution. Tubes were used to connect the metal plates with the syringe pump. The metal plates were heated to crystallization temperature at 75 °C. Following the formation of the $MAPbBr_3$ single crystals; they were removed from the silicon rubber which was between the metal plates and dried with clean room wipes and a nitrogen gun. The structure and optical properties of $MAPbBr_3$ single crystal were investigated.

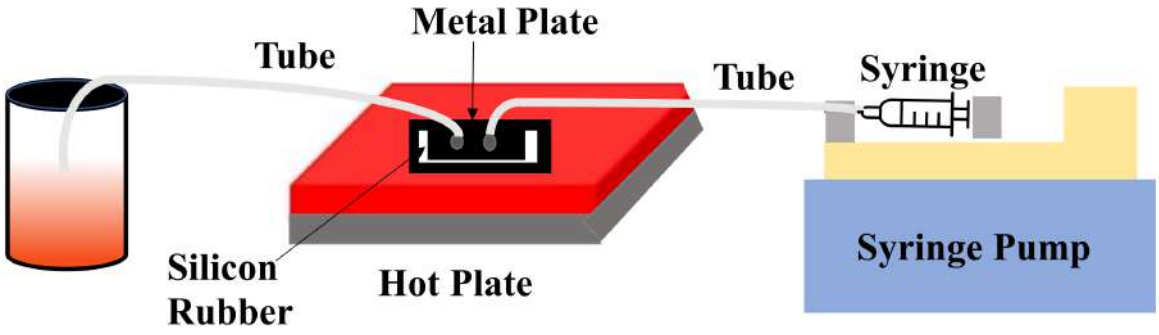

Figure 4.13 Growth in IR-cell scheme.

4.5. Results and discussion of crystals grown using IR-cell method

4.5.1. Structural characterization

Atomic force microscopy

Atomic force microscopy (AFM) measurement was performed on the sample's surface by using non-contact mode. The AFM of the $MAPbBr_3$ single crystal shows a smooth surface with a root mean square (RMS) roughness of about 6 nm as shown in Figure 4.16 and indicating that $MAPbBr_3$ has a high quality surface that will cause lower scattering during z-scan measurements.

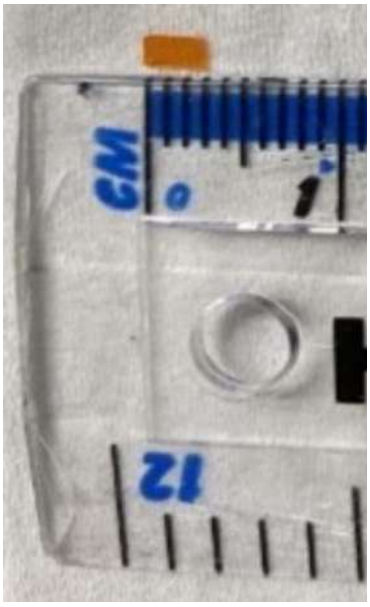

Figure 4.14 Image of $MAPbBr_3$ single crystal formed by IR-cell of liquid method with dimnation of 4×2 mm.

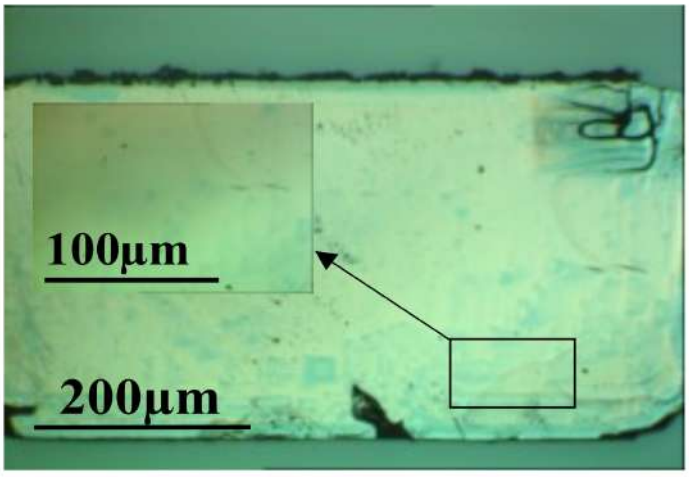

Figure 4.15 A microscope image of single crystal of $MAPbBr_3$ prepared by the IR-cell method with thickness of 100 µm and without chemical polishing.

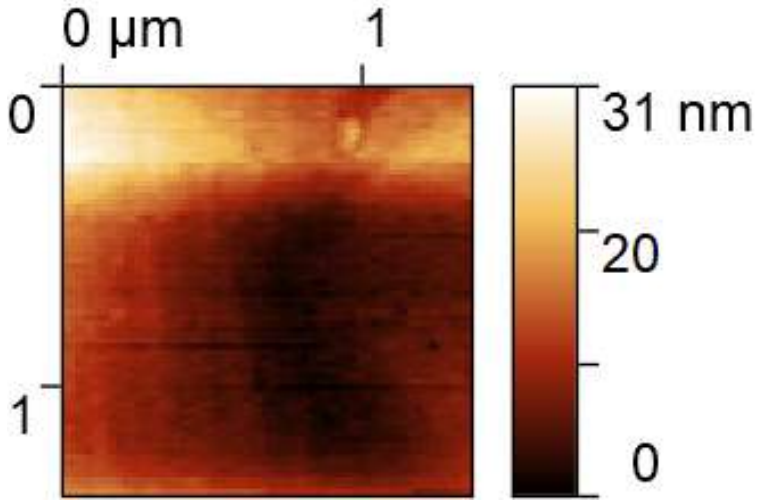

Figure 4.16 AFM image with line profile of $MAPbBr_3$ single crystal formed using IR-cell

X-ray diffraction (XRD)

X-ray diffraction (XRD) was performed on the single crystals to identify their phases and compare them with theoretical XRD spectra taken on a Bruker D8 Advance diffractometer in coupled $\theta/2\theta$ regime. For generating the X-rays, a copper (Cu) anode ceramic X-ray tube is used. At a wavelength of 1.5406 Å, the X-ray tube is operated at a voltage of 40 kV and a current of 40 mA. A monochromatic x-ray beam is produced by the optical mirror of dimensions up to 0.3 mm by 11 mm.

Figure 4.17 illustrates that $MAPbBr_3$ crystal is pure perovskite single crystal and only have two crystallographic planes (100) and (200), which indicates that it has a high crystallographic orientation. Furthermore, X-ray diffraction analysis of the $MAPbBr_3$ crystal confirmed a cubic diffraction pattern with the space group of (Pm-3m) which matched well with the existing standard database (COD ID # 4516751) and unit cell parameters (a = 5.943 Å) were found to be in agreement with previous reports [134].

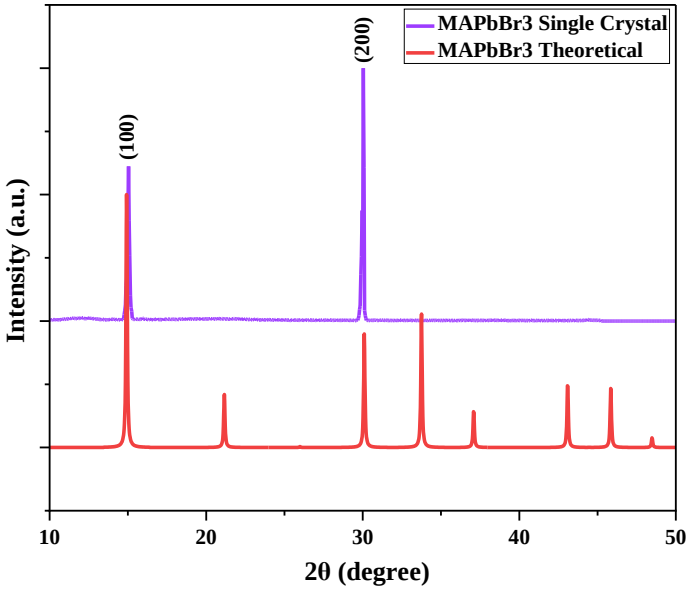

Figure 4.17 X-ray diffraction of $MAPbBr_3$ single crystal.

4.5.2. Optical characterization

UV-vis measurements

UV-vis absorption spectra were taken for $MAPbBr_3$ single crystal and this was used to create the Tauc plots shown in Figure 4.18. This research involved the recording of the UV-vis using a Shimadzu UV-1800 Spectroscope. The UV-vis measurements were carried out by following the steps below. Spectrum mode was selected for wavelength scanning over a continuous wide range, as the wavelength range was 200 to 800 nm, with a spectral resolution of 0.1 nm and medium scan speed. The baseline was removed using the software. The sample was placed in the sample compartment. Finally, spectral data collection was initiated. Measurements were performed at room temperature. The bandgap energy was determined for the sample using linear extrapolations to the x-axis intercept in Tauc plots. A linear fitting was applied only within the energy range 2.1-2.3 eV to estimate the band gap of the sample from these adsorptions. The $MAPbBr_3$ was measured to have a bandgap value of 2.18 eV. This value is close to those published in literature [83] [152], and it is equal to that measured on the spin-coated film.

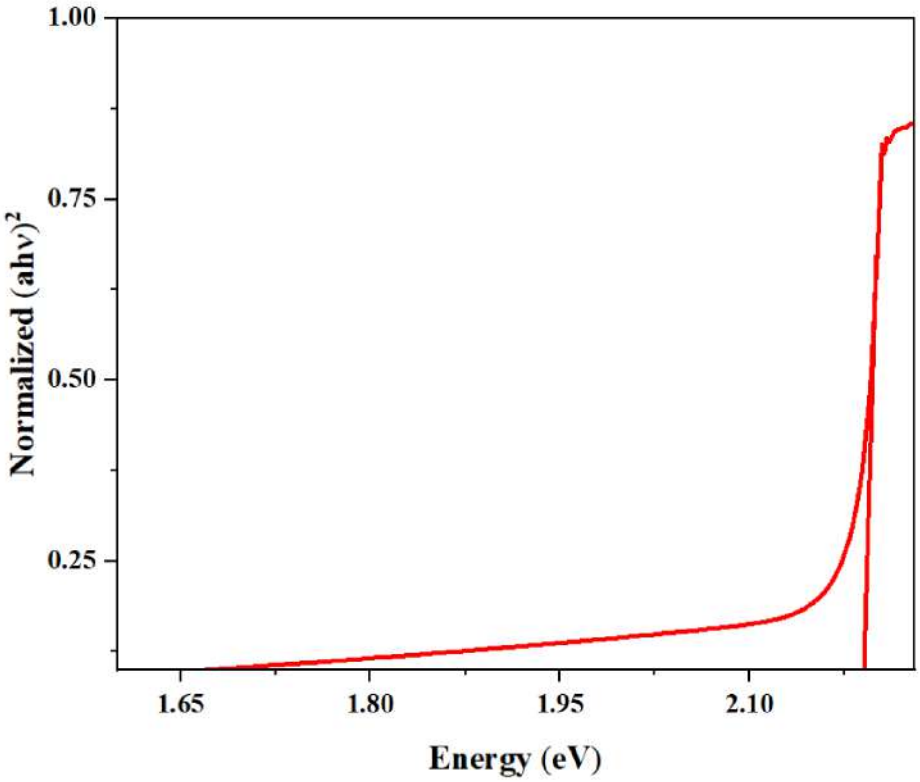

Figure 4.18 Tauc plots for $MAPbBr_3$ single crystal. solid lines represent the linear fit

z-scan measurements

Using the z-scan technique, the nonlinear optical response of $MAPbBr_3$ was measured with the same parameters used in section (3.6.2). $MAPbBr_3$ single crystal demonstrated a "peak-valley" trace from the closed-aperture z-scan measurement, as shown in 4.19 a. The value returned for the n_2 was $1.9 \times 10^{-18}\,m^2\,W^{-1}$. The traces obtained from the open-aperture z-scan for the $MAPbBr_3$ show a strong nonlinear absorption coefficient of $1.3 \times 10^{-11}\,m\,W^{-1}$ as shown in 4.19 b. Figure 4.19 shows that the data points do not follow the fitting line; this may be due to the poor quality of the measured region. The nonlinear refractive index and two photon absorption of the $MAPbBr_3$ film is slightly higher than about that of $MAPbBr_3$ single crystal and this is attributed to a better coupling between the laser and the randomly distributed crystallites. The values of nonlinear refractive index and two-photon absorption of $MAPbBr_3$ single crystal presented here differ from those published in literature [152] [153] [154] [83]. Differences in results are due to the shorter wavelength chosen and errors in the literature owing to poor laser parameter selection.

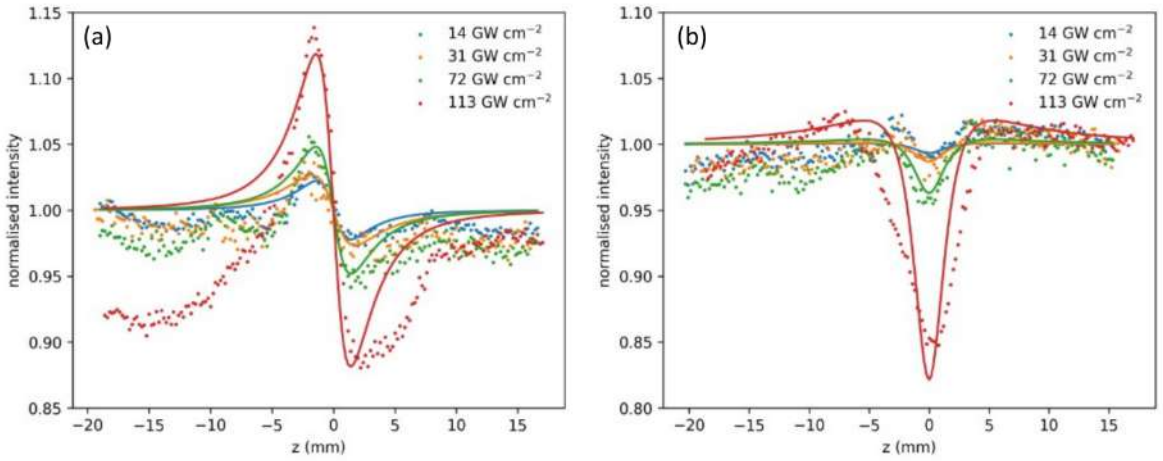

Figure 4.19 (a) Closed-aperture z-scan, (b) Open-aperture z-scan of $MAPbBr_3$ single crystal grown by the IR-cell method. Dots are the measured data and the lines represent the data fit.

4.6. Conclusion

The third-order nonlinear optical properties of metal-hailde perovskites films and single crystal are investigated in this chapter by using the z-scan technique. In comparison with $MAPbBr_3$ and $MAPbCl_3$, $MAPbI_3$ exhibits a high nonlinear refractive index. It is 2 times higher than $MAPbBr_3$ and 10 times higher than $MAPbCl_3$. This stronger response is believed to be caused by electrons being more susceptible to the incident laser. Moreover, the two photon absorption of $MAPbI_3$ is about 10 times higher than that of $MAPbBr_3$, while the $MAPbCl_3$ sample shows no evidence of multiphoton absorption, and the β was effectively zero the sample. A number of methods for growing single crystals with good optical properties were investigated and it was shown that growing crystals with confined geometries was the best method, this key result informs the later chapter on perovskite optical fibres.

Chapter 5. Third-order nonlinear response of metal-free perovskites films

5.1. Introduction

This chapter explores ABX_3 metal-free perovskite materials as a new class of materials for third-order nonlinear optical processes. Although several studies have demonstrated strong nonlinear response in metal-perovskites, [15] [16] [17] [18] [19] [20] [21] there are issues when applying these materials in nonlinear optics. Specifically, the narrow band gap of metal-perovskites (1.5 - 3 eV) [22] leads to high optical absorption, which restricts their uses in visible and UV regions. A narrow band gap also means a low laser damage threshold, which limits their practicality in nonlinear optics as high intensity light is typically required to operate in this regime. Additionally, the metal-perovskites with high optical performance are usually lead-based, which is toxic and non-environmental friendly. Therefore, it is reasonable to look for alternative materials that are more suitable for nonlinear optics. One potential replacement for metal- perovskites is metal-free perovskites. The metal-free perovskites also have the ABX_3 configuration, only the B site is occupied by NH_4 in this case. For the A site, many organic molecules have been identified to be suitable in the perovskite framework, [23] with the interests in DABCO (*N*-*N*′- diazabicyclo[2.2.2]octonium, $C_6H_{12}N_2$) and its derivative Methyl-DABCO (*N*-methyl-*N*′- diazabicyclo[2.2.2]octonium, $C_7H_{15}N_2$) are the highest. To further simplify their long compound names, DNX and MDNX, where X is the halide (I, Br, Cl), will be used to represent DABCO-NH_4X_3 and Methyl-DABCO-NH_4X_3 respectively. Various aspects of the metal-free perovskites have been studied [24] [25] [26] [27] [28] [29] [30] [31] and theoretical calculations have predicted these materials possess wide band gaps [32]. Along with their organic nature, metal-free perovskites pose as a solution to the narrow band gap and toxic issues of hybrid perovskites. The aim here is to investigate the third-order nonlinear response of a range of compounds in this metal-free perovskites family, with different combinations of cations

(DABCO and Methyl-DABCO) and halides (iodide, bromide and chloride), in order to understand the their influences on the nonlinear properties of these materials.

5.2. Metal-free perovskites thin films

5.2.1. Preparation of crystal deposition source

1,4-Diazabicyclo[2.2.2]octane (DABCO), Ammonium iodide(NH_4I), Ammonium bromide (NH_4Br), Ammonium chloride (NH_4Cl), hydroiodic acid (HI), hydrobromic acid (HBr),and hydrochloric acid (HCl) (57% w/w stabilized with 1.5% H_3PO_3) were purchased from Tokyo Chemical Industry (TCI) and used as received. N-Methyl-1,4 diazabicyclo[2.2.2]octan-1-ium (Methyl-DABCO) iodide was synthesized as described else where [155] [156].

N-Methyl-1,4-diazabicyclo[2.2.2]octan-1-ium Ammonium iodide (MDNI)

10.2 g portions of Methyl-DABCO iodide and 5.75 g of NH_4I were dissolved in 26 mL of DI water and magnetic stirring; added dropwise 26 mL of 57% w/w hydroiodic acid HI (with 1.5% hypophosphorous acid). Heated up at 90 °C cooling the pale yellow solution to room temperature resulted in the precipitation of a white polycrystalline material. Washing with Et_2O and drying in a vacuum gave MDNI as a white crystalline solid in 70% yield.

N-Methyl-1,4-diazabicyclo[2.2.2]octan-1-ium Ammonium bromide (MDNBr)

10.2 g portions of Methyl-DABCO bromide and 5.75 g of NH_4Br were dissolved in 26 mL of DI water and magnetic stirring; added dropwise 26 mL of 57% w/w hydrobromic acid HBr (with 1.5% hypophosphorous acid). Heated up at 90 °C cooling the pale yellow solution to room temperature resulted in the precipitation of a white polycrystalline material. Washing with Et_2O and drying in a vacuum gave MDNBr as a white crystalline solid in 70% yield.

4-diazabicyclo[2.2.2]octan-1-ium Ammonium iodide (DNI)

11.2 g of DABCO and 14.5 g of NH_4I were dissolved with 90 mL of DI water and magnetic stirring. Added dropwise 50 mL of HI; heated the solution at 95 °C cooling the pale yellow solution to room temperature resulted in the precipitation of a white polycrystalline material. Washing with Et_2O and drying in a vacuum gave DNI as a white crystalline solid in 0.45% yield.

4-diazabicyclo[2.2.2]octan-1-ium Ammonium bromide (DNBr)

11.2 g of DABCO and 14.5 g of NH_4Br were dissolved with 90 mL of DI water and magnetic stirring. Added dropwise 50 mL of HBr; heated the solution at 95 °C cooling the pale yellow solution to room temperature resulted in the precipitation of a white polycrystalline material. Washing with Et_2O and drying in a vacuum gave DNBr as a white crystalline solid in 0.61% yield.

4-diazabicyclo[2.2.2]octan-1-ium Ammonium bromide (DNC)

11.2 g of DABCO and 14.5 g of NH_4Cl were dissolved with 90 mL of DI water and magnetic stirring. Added dropwise 50 mL of HCl; heated the solution at 95 °C cooling the pale yellow solution to room temperature resulted in the precipitation of a white polycrystalline material. Washing with Et_2O and drying in a vacuum gave DNC as a white crystalline solid in 0.78% yield.

5.2.2. Evaporation of metal-free perovskites thin films

Metal-free perovskites films were evaporated in a thermal evaporator as shown in Figure 5.1. In a quartz crucible, 50 mg of metal-free perovskites powders were added and placed into a tungsten basket heater. From the source, the substrates were placed face down at a distance of 30 cm. The chamber was pumped down to 10^{-6} mbar, and the pressure was maintained above 1×10^{-5} mbar during evaporation.

During this study, thermogravimetric analysis (TGA) and differential scanning calorimetry (DSC) measurements were carried out in order to evaluate the thermal stability of metal-free perovskites materials and to identify the ideal range of evaporation temperatures. The evaporation temperature for DNI, MDNI was 165 °C, while for DNBr, MDNBr was 155 °C and 150 °C, and it was 140 °C for DNC, while the evaporation time were 60 min for all films.

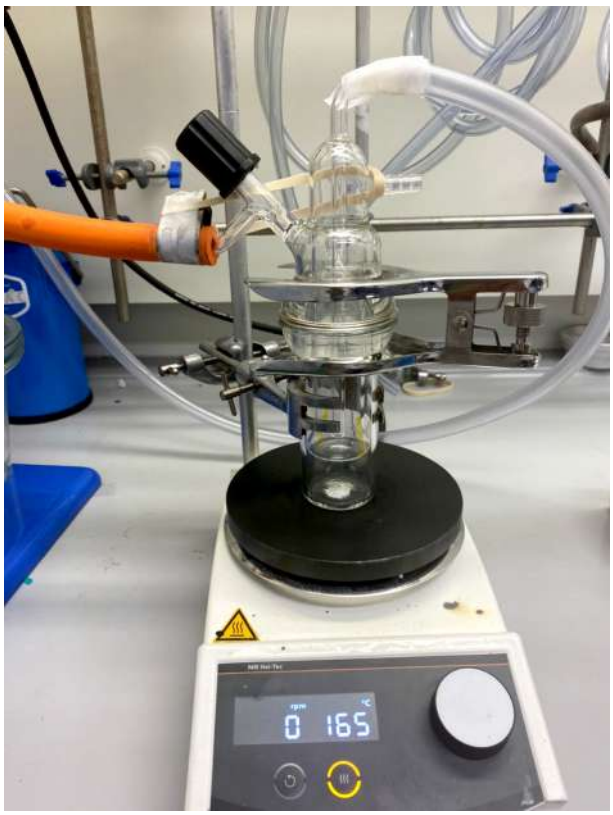

Figure 5.1 Evaporation Setup.

5.3. Results and discussion of metal-free perovskites thin films

In this work, the powders were first synthesized and then deposited onto a substrate as a thin film with a thickness of around 500 nm. The powders were prepared by cooling an equimolar saturated solution which was composed of the requisite cations (iodides, bromides, chlorides) as well as hydroiodic, hydrobromic, and hydrochloric acid. In this regard, this method for film deposition has been simplified in a way that is far simpler and easier to manage than the well-established and much more complex dual-source evaporation procedure required for the deposition of the state-of-the-art lead-based perovskites [157] [158]. Moreover, this simple deposition method provides highly transparent films without pinholes, as shown in Figure 5.2.

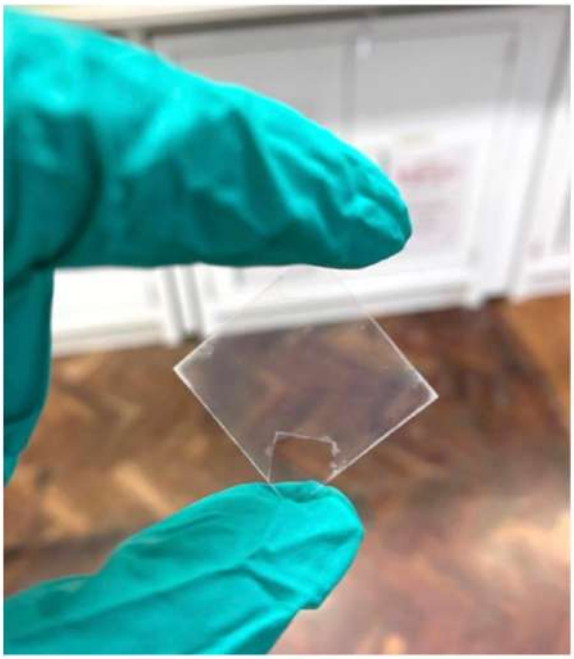

Figure 5.2 Metal-free perovskites film deposited on a substrate with a 500 nm thickness.

Thermogravimetric analysis (TGA) and Differential Scanning Calorimetry(DSC)

Thermogravimetric analysis (TGA) and differential scanning calorimetry (DSC) measurements results were presented in Figure 5.3. At temperatures above 198 °C, DNI shows the onset of thermal decomposition with the first DSC peak at 235 °C. In the case of DNBr, the phase transition occurs above the decomposition onset temperature of 143 °C with the first DSC peak at 339.4 °C, while in the case of DNC the phase transition occurs above the decomposition onset temperature of 153 °C with the first DSC peak at 313.1 °C. In order to avoid secondary phases appearing in the evaporated films, the temperature of the source material was kept below 165 °C. The evaporation temperature chosen for each material in this work was the lowest temperature at which the evaporation began. However, although the evaporation temperatures of DNBr 155 °C and DNC 140 °C were 10 to 25 °C lower than that of DNI 165 °C. When temperatures rise over 168 °C, MDNI begins to decompose with its first DSC peak occurring at 257 °C. In the case of MDNBr, the phase transition occurs above the decomposition onset temperature of 171 °C with the first DSC peak at 251 °C as shown in Figure 5.4. For avoiding the appearance of secondary phases, we kept the source material temperature below 165 °C. The evaporation temperature of MDNBr (150 °C) were 10 °C lower than that of MDNI (165 °C).

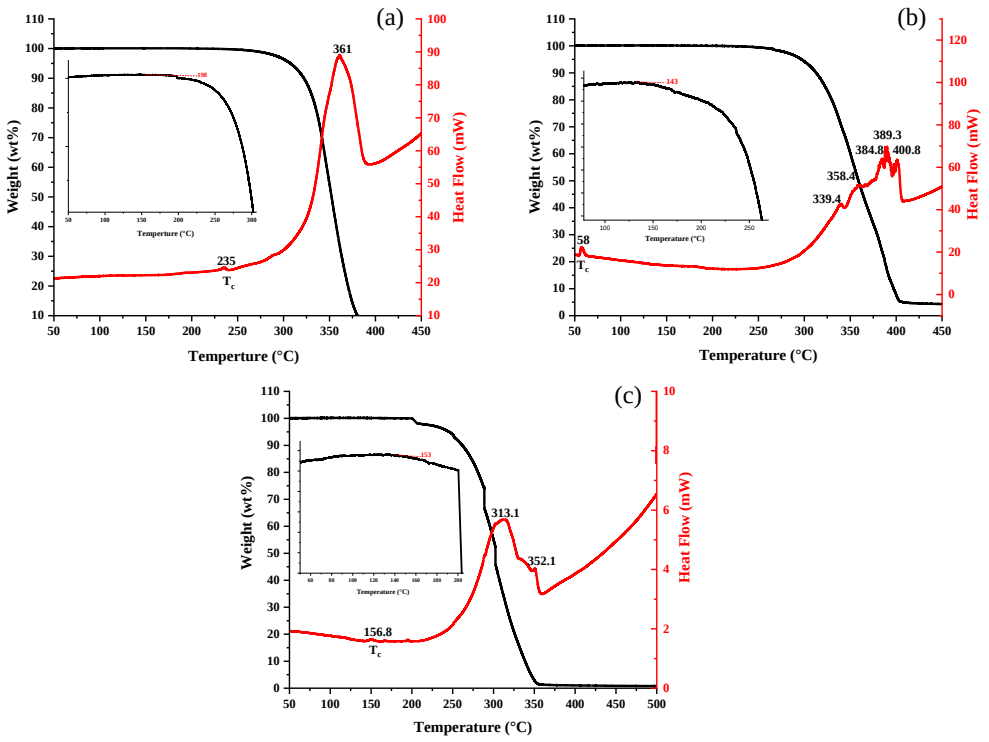

Figure 5.3 TGA and DSC for evaporated films of (a) DNI, (b) DNBr, and (c) DNC.

5.3.1. Structural characterizations

Atomic force microscopy

The surface texture of the evaporated films was investigated by atomic force microscopy (AFM); usig non-contact mode. DNI exhibits a smooth surface with a root mean square (RMS) roughness of about 10 nm, while DNBr and DNC have a slightly rougher surface with a RMS value of 46 and 52 nm as shown in Figure 5.5. The mean grain size measured from the AFM images was that 170 nm, 210 nm, and 230 nm for DNI, DNBr, and DNC respectively. The grain

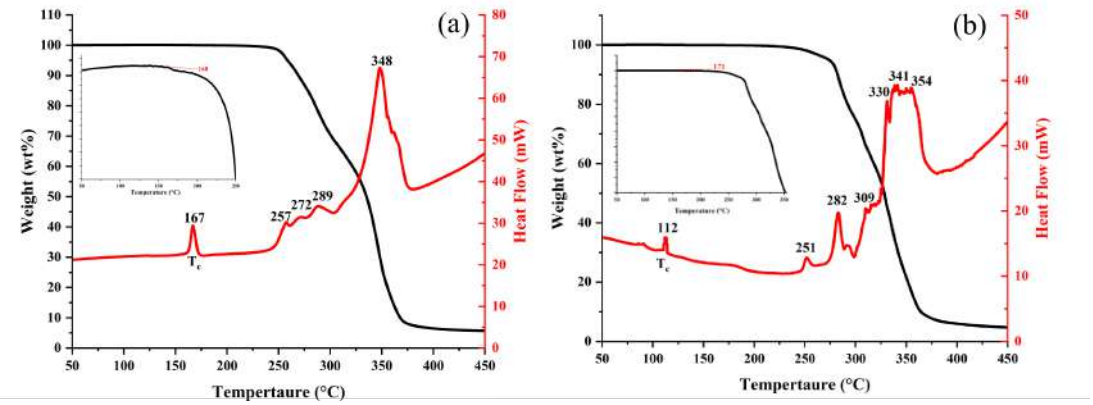

Figure 5.4 TGA and DSC for evaporated films of (a) MDNI and (b) MDNBr.

size of inorganic-organic perovskites films produced by thermal evaporation is typically controlled by the substrate temperature. However, the understanding of the effect is still under debate, with some studies demonstrated low substrate temperature led to large grain size while some showed the opposite [159–161]. The substrate temperature for evaporation in this study was kept at room temperature and the only difference between the evaporation of different materials was the evaporation temperature.

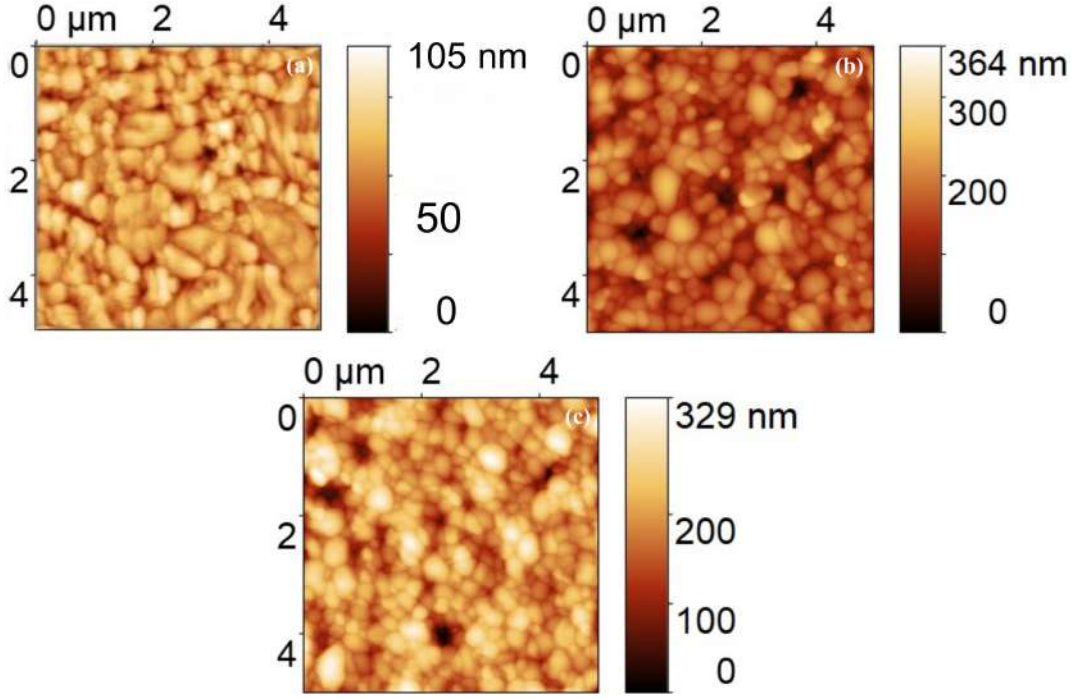

Figure 5.5 AFM images for evaporated films of (a) DNI, (b) DNBr, and (c) DNC.

X-ray diffraction (XRD)

The metal-free perovskites films were deposited on thin silica substrates by single source evaporation of prefabricated crystalline powders as mentioned in section 5.2. The diffraction pattern of metal-free perovskites films indicated ordered materials were formed on the substrate, where the reflections of DNI correspond to a hexagonal structure while DNBr, and DNC have a trigonal structure. The diffraction pattern for the synthesized films and powders and the theoretical diffraction patterns, which were calculated using the crystal data [23] are shown in Figure 5.6. No secondary phase was detected from the diffraction pattern of the evaporated films. Secondary phase is a common concern in thermal evaporation of metal halide inorganic-organic perovskites because the vapor pressure of the organic compound is generally much higher than its inorganic counterpart [162] [163] [164]. On the contrary, there is no inorganic compound in

the metal-free perovskites, it is less likely to suffer from the same problem during single source thermal evaporation.

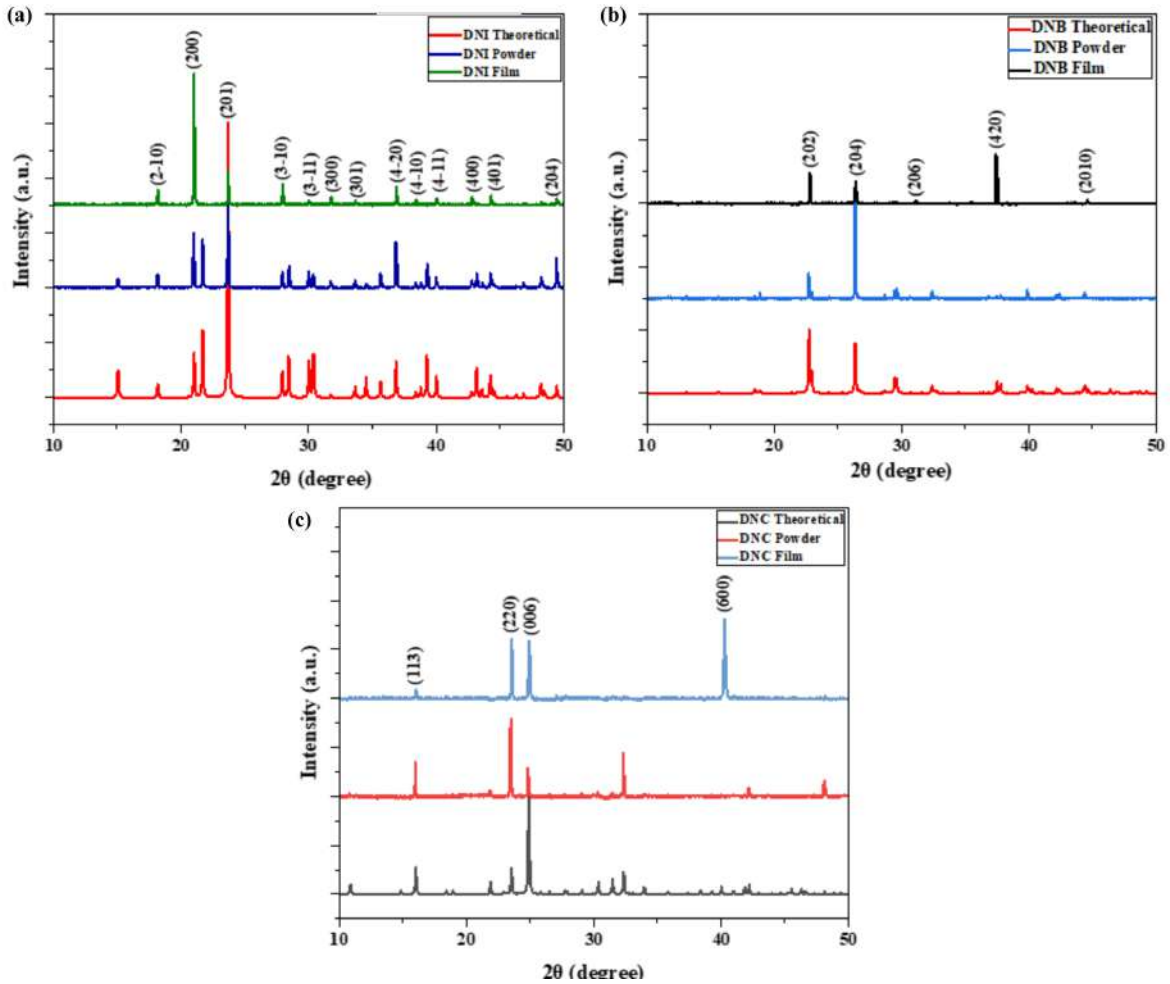

Figure 5.6 X-ray difffraction patterns for evaporated films of (a) DNI, (b) DNBr, and (c) DNC.

5.3.2. Optical characterizations

z-scan measurements

The third-order nonlinear refractive index (n_2) and two-photon absorption coefficient (β) were determined using standard z-scan technique. The closed-aperture z-scan measurement of DNI, DNBr, and DNC are presented in Figure 5.7, and all materials demonstrated a 'peak-valley' trace from the closed-aperture. The nonlinear refractive index values returned for the n_2 were $3 \times 10^{-18}\,\mathrm{m^2\,W^{-1}}1$ for the DNI, $4.3 \times 10^{-18}\,\mathrm{m^2\,W^{-1}}$ for the DNBr, and $4.6 \times 10^{-18}\,\mathrm{m^2\,W^{-1}}$for the DNC (Table 5.1) [165]. These materials were found to have nonlinear refractive index values similar to each other and their third nonlinear magnitude lower than that of metal-halide perovskites. The materials have different crystal structures, but we

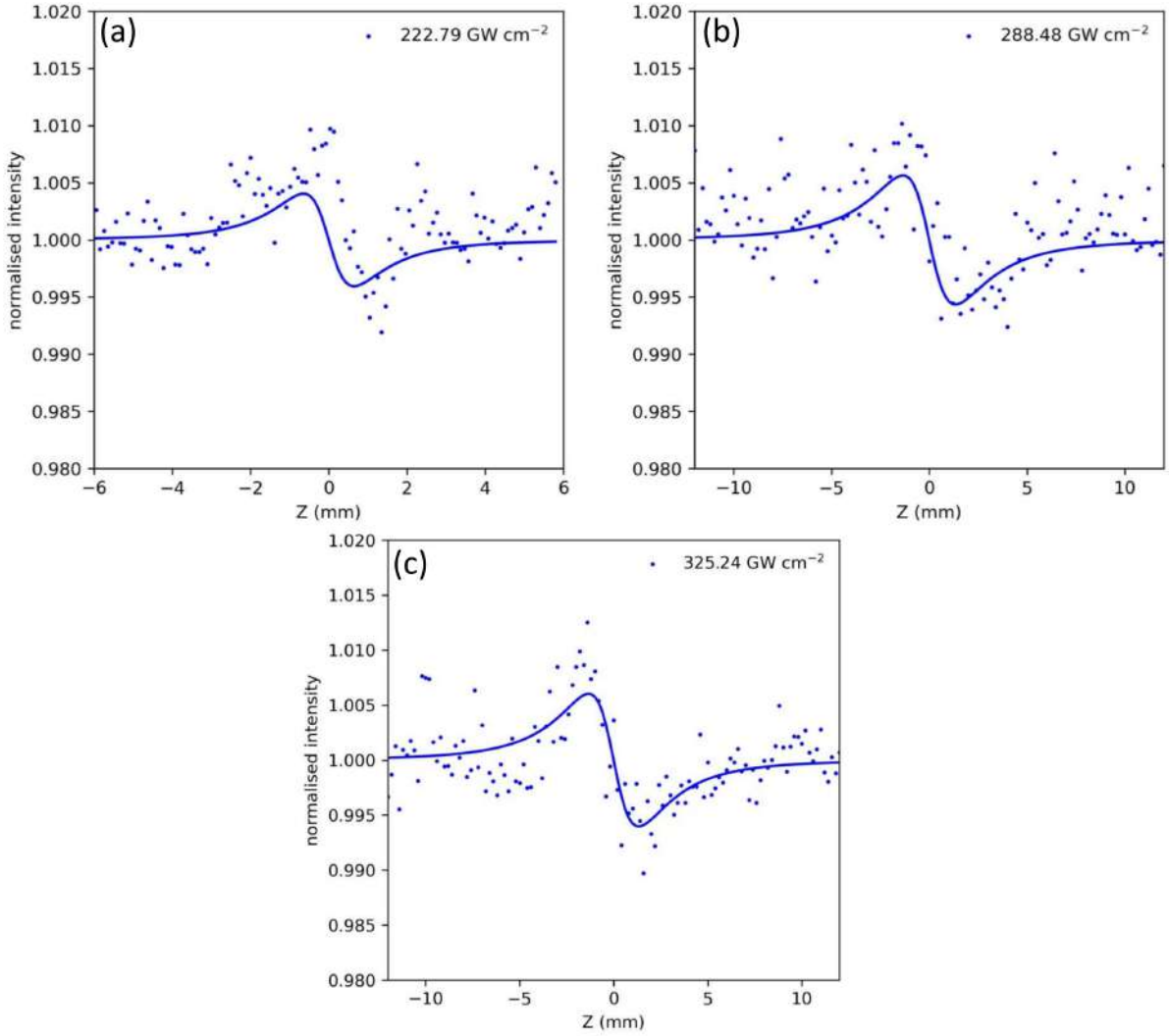

Figure 5.7 Closed-aperture z-scan of (a) DNI, (b) DNBr and (c) DNC. Dots are the measured data and the lines represent the data fit.

were not able to see large differences in nonlinear response. So we have added methyl groups to the materials structure to study how they affect the nonlinear properties.

The traces obtained from the open-aperture z-scan for all materials were straight lines, indicating that there was no two-photon absorption at the wavelength of 1060 nm as shown in Figure 5.8. This is due to the wide band gap of these metal-free perovskites, which were determined by UV-vis spectrophotometry as shown in Figure 5.9 and DNBr stands out with a wide band gap of 5.85 eV, which is significantly higher than the others. A previously report showed that the band gap of DNI, DNBr and DNC is 4.71, 5.25 and 5.89 eV respectively [31], whereas in this work the band gap measured for DNI, DNBr, and DNC is 4.97, 5.85 and 5.08 eV. The difference between the values is probably due to the sample preparation method and sample thickness. DNI

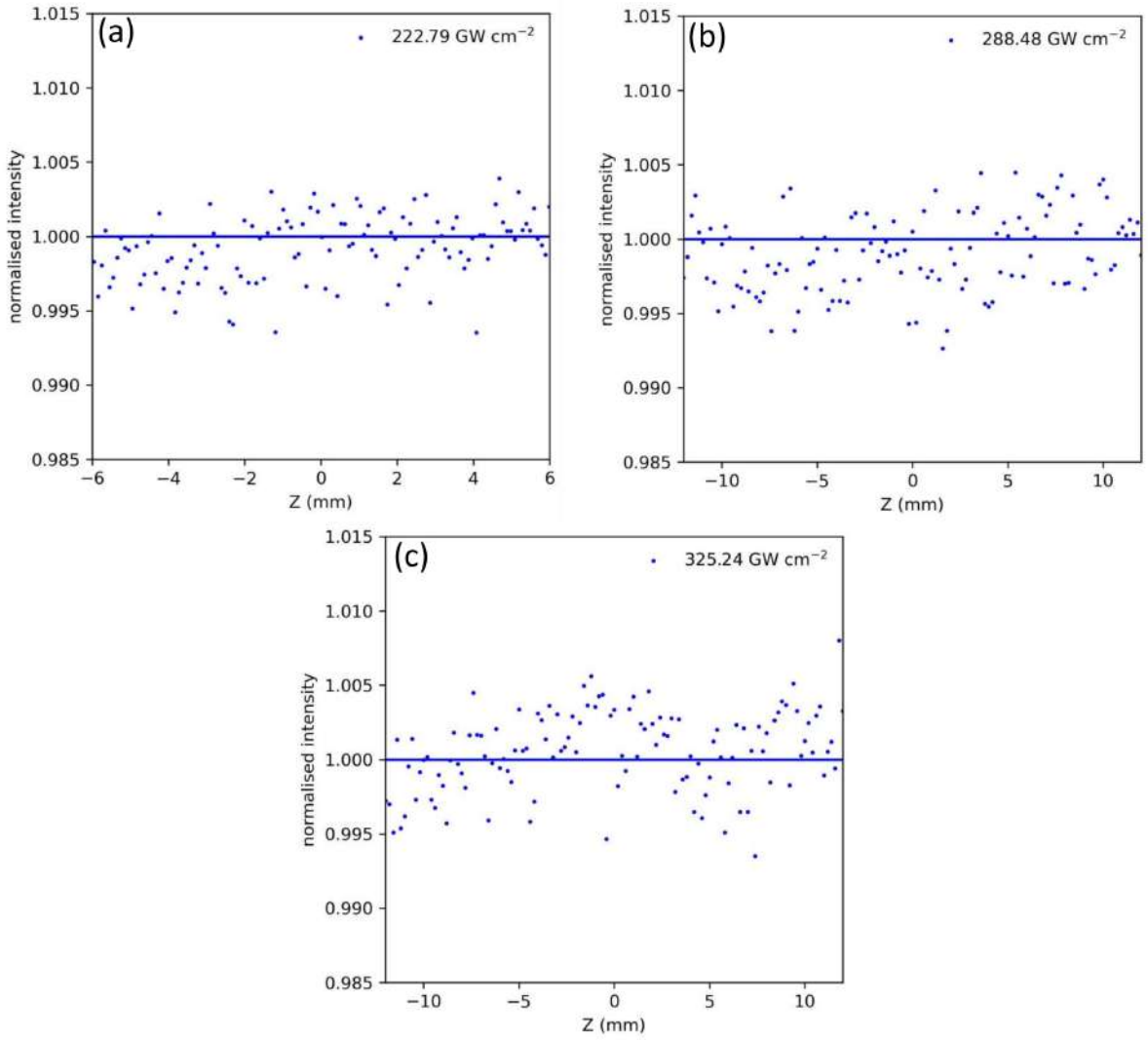

Figure 5.8 Opened-aperture z-scan of (a) DNI, (b) DNBr and (c) DNC. Dots are the measured data and the lines represent the data fit.

was linearly fitted within the energy range 4.7-5 eV, whereas DNBr and DNC were linearly fitted within the energy range 5.5-5.9 eV and 4.5-5.1 eV, respectively.

A bulk crystal has a higher possibility of containing defects than a thin film, which may explain the lower measured values. The wide band gap nature of these materials suggests that they can operate in a wide range of wavelengths without suffering from two-photon absorption, which is the common cause of low figure of merit for third-order nonlinear optics (Equation 4.2). For example, $MAPbI_3$ and $MAPbBr_3$ exhibit a high third-order nonlinear refractive index of $5.8 \times 10^{-17}\,m^2\,W^{-1}$ and $3.8 \times 10^{-17}\,m^2\,W^{-1}$ but the figure of merit is as low as 0.05 and 0.35 because of their high two-photon absorption $1.2 \times 10^{-9}\,m\,W^{-1}$ and $5.3 \times 10^{-10}\,m\,W^{-1}$. The bandgap energy was determined for the sample using linear extrapolations to the x-axis intercept in Tauc plots.

Materials	n_2 ($m^2 W^{-1}$)	β ($m W^{-1}$)	FOM_{nl}	Band gap (eV)
DNI (DABCO-NH_4I_3)	3×10^{-18}	1×10^{-13}	>28	4.97
DNBr (DABCO-NH_4Br_3)	4.3×10^{-18}	1×10^{-13}	>40	5.85
DNC (DABCO-NH_4Cl_3)	4.6×10^{-18}	1×10^{-13}	>43	5.08

Table 5.1 Optical properties of metal-free perovskites

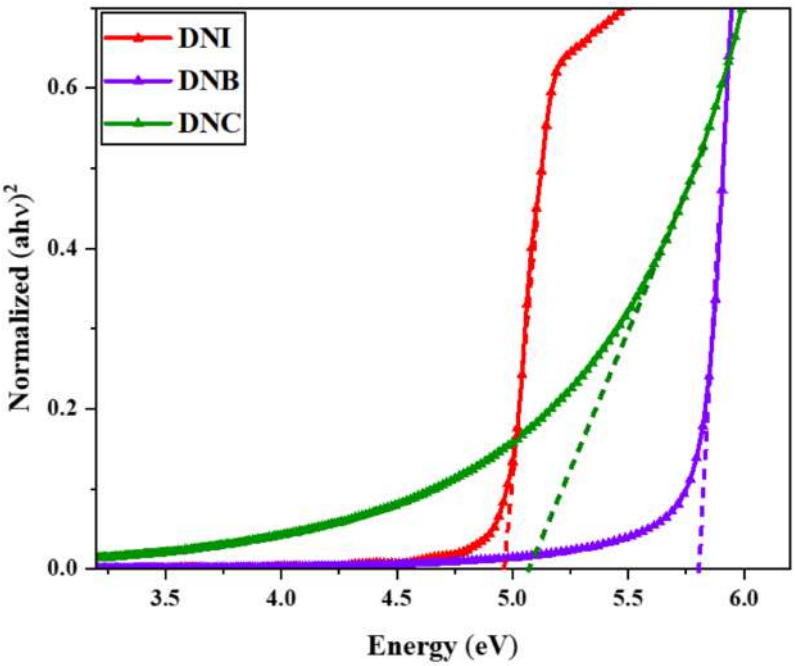

Figure 5.9 Tauc plots for DNI, DNBr and DNC. Dashed lines represent the linear fit.

5.4. The role of methyl group in metal-free perovskites for nonlinear optics

A polar cation is incorporated into the nonpolar DABCO-NH_4I_3 (DNI) and DABCO-NH_4Br_3 (DNBr) systems to produce methylDABCO (MDNI) and (MDNBr), changing the structure from hexagonal perovskites to a trigonal perovskites in both with ammonium halide octahedra, which results in high third order nonlinearity. It is found that the methyl group (-CH_3) in Methyl-DABCO is responsible for the distortion of the perovskites structure, which expectedly leads to the strong third order nonlinear response.

5.5. Results and discussion

5.5.1. Structural characterizations

Atomic force microscopy

The surface texture of the evaporated films were investigated by atomic force microscopy (AFM) usig non-contact mode. A smooth surface is typically desirable for optical measurement as it minimizes the scattering of the incident light. Both DNI and MDNI exhibits a smooth surface with root mean square (RMS) roughness of about 10 nm, while DNBr and MDNBr have a slightly rougher surface with a RMS value of 46 and 68 nm respectively (Figure 5.10). The high roughness of MDNBr is believed to be originated from the grain boundary. The mean grain size measured from the AFM images was that 170 nm in both DNI, and MDNI, films produced very similar results. According to this, the quality of deposition doesn't seem to be influenced by the cation. The mean grain size for DNBr was about 210 nm, while in case of MDNBr, the grain size was about 1.67 μm. Such large grain size corroborates with the XRD data (Figure 5.11), which shows a highly ordered 200 orientation.

X-ray diffraction (XRD)

Figure 5.11 shows how the deposited films were analyzed by X-ray diffraction (XRD) to identify the material phase. The results were compared to the deposited materials and theoretical XRD spectra, which were calculated using the crystal data [23].

The diffraction pattern of metal-free perovskite films indicated ordered materials were formed on the substrate, where the reflections of DNI corresponds to a hexagonal structure while MDNI,

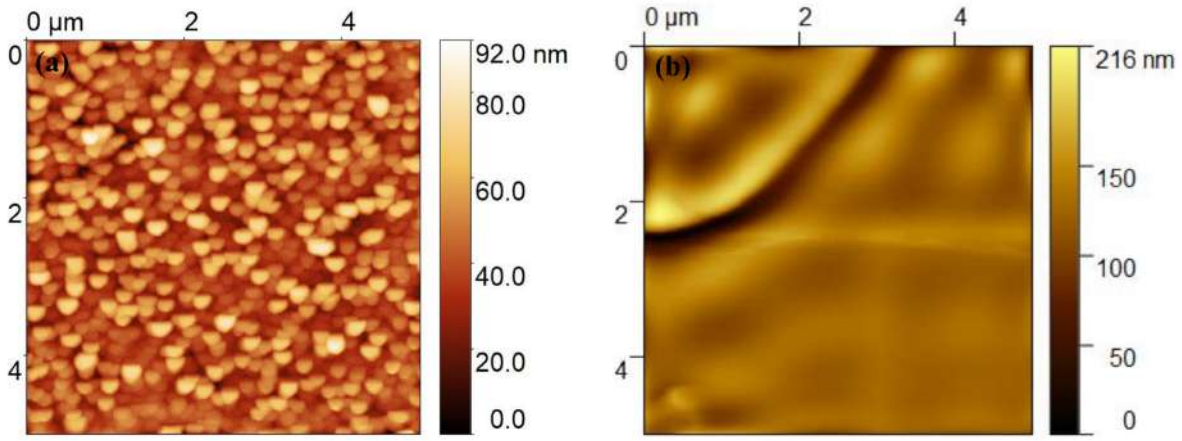

Figure 5.10 AFM image of the as-evaporated (a)MDNI, (b) MDNBr films.

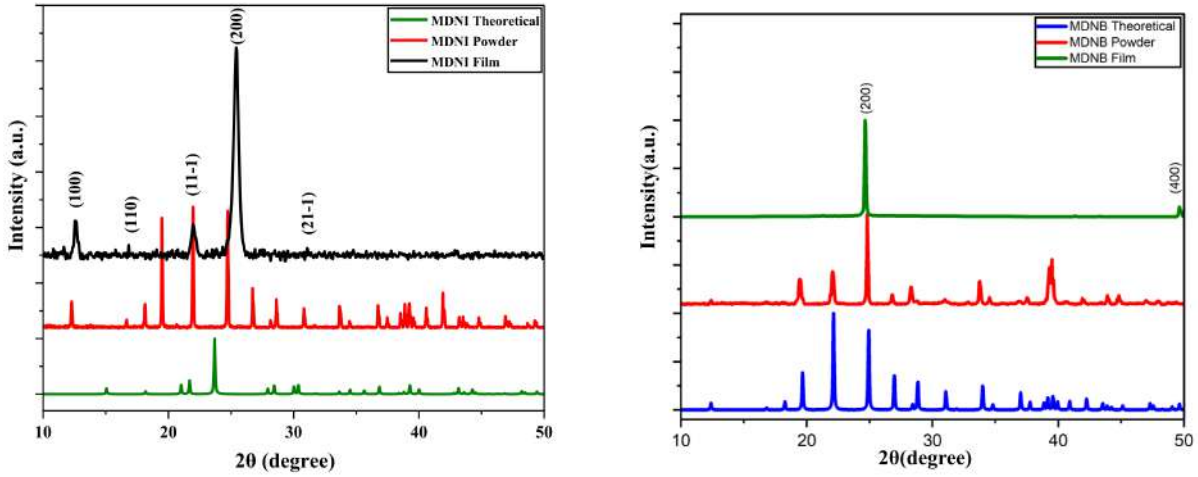

Figure 5.11 XRD pattern of MDNI and MDNB produced by evaporation, and the corresponding with the source powder and theoretical spectra.

DNBr and MDNBr has a trigonal structure. No secondary phase was detected from the diffraction pattern of the evaporated films. One the other hand, MDNI shows (100), (11-1) and (200) reflections, with (200) the strongest. The missing of (11-1) reflection in the diffraction pattern of MDNBr film suggests that the crystals may not be oriented favourably for nonlinear response. It is worth mentioning that while a 2% compressive strain was reported for MDNI film, [165] there was a 1% tensile strain detected in MDNBr film along the (100) plane as shown in Figure 5.12. However, the origin of the strains remained unknown at this stage as the glass substrate was employed in the experiment and there should be no lattice mismatch between the substrate and film, which is the typical cause of compressive/tensile strain. On the other hand, there is no strain found in both evaporated DNI and DNBr films.

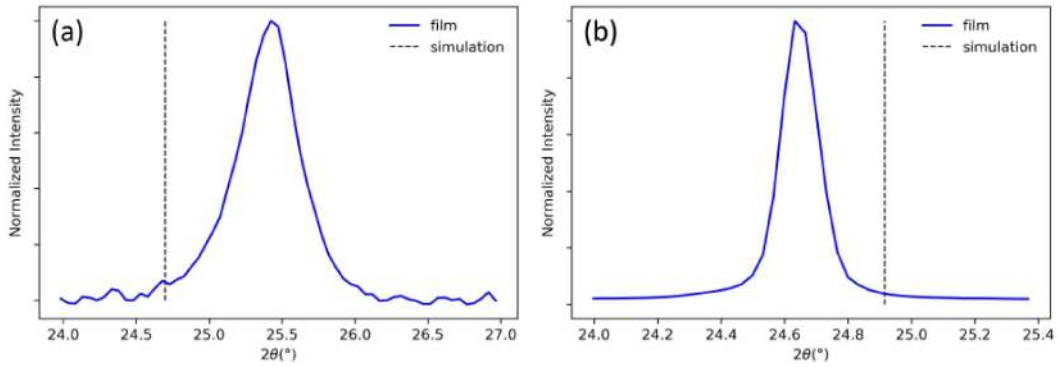

Figure 5.12 Angle position of (200) plane and the simulated angle position for (a) MDNI and (b) MDNBr.

5.5.2. Optical characterizations

UV-vis measurements

Figure 5.13 shows the Tauc plots generated from the UV-vis absorption spectra of these materials. DNBr stands out with a wide band gap of 5.85 eV, which is significantly higher than the others (4.97 - 5.12 - 5.02 eV, Table 5.2). MDNI was linearly fitted within the energy range 5-5.2 eV, whereas MDNBr was linearly fitted within the energy range 5-5.1 eV. Variations in halogen substitutions and methyl substitutions can explain the differences in band gaps between materials. The alterations in the chemical compounds can change the energy levels of the conduction and valence bands, resulting in varying band widths. A previous report showed that the band gap of DNI and DNBr is 4.71 and 5.25 eV respectively [31], whereas here the band gap measured for DNI and DNBr is 4.97 and 5.85 eV. The difference between the values is probably due to the sample preparation method and thickness. Here, the materials were first synthesized and then deposited onto a substrate as a thin film with a thickness of around 500 nm. The band gap of MDNI and MDNBr to be 6.47 and 7.02 eV respectively [32], which is higher than the measured values, 5.12 and 5.02 eV.

Here. It is possible that the defects in the evaporated films lead to slightly narrower band gap in the experiment.

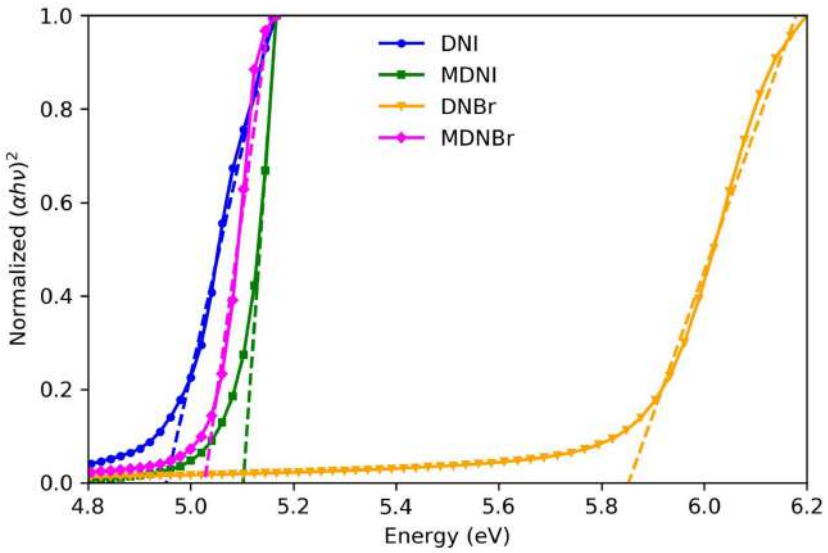

Figure 5.13 Tauc plots for DNI, MDNI, DNBr and MDNBr. Dashed lines represent the linear fit.

z-scan measurements

All materials demonstrated a 'peak-valley' trace from the closed-aperture z-scan measurementas shown in Figure 5.14. The nonlinear refractive index of MDNI was found to be the highest among the studied materials, with $5.7 \times 10^{-17}\,\mathrm{m^2\,W^{-1}}$. When considering the materials with the same halide, the nonlinear refractive index of MDNI is about 20 times higher than that of DNI, while MDNBr is about 6 times higher than DNBr (Table 5.2). It is clear that the incorporation of methyl group in the cation site of the perovskite can enhance the nonlinearity of the materials. DABCO is a non-polar molecule with D_{3h} point group, when a methyl group is added to one of the nitrogen atom in DABCO, it transforms to a polar point group C_{3v} with lower symmetry. This symmetry-breaking strategy was originally developed for achieving ferroelectric response in inorganic-organic perovskites [166] and was later adopted in all-organic perovskites [23]. It is believed that the dipole moment and the distortion of the hexaiodide/hexabromide octahedra result in the enhanced nonlinear responses.

As confirmed by diffraction patterns, DNI belongs to non-polar space groups, which explains why their nonlinear responses are low. When replacing DABCO with Methyl-DABCO, the crystal structure changes to polar space group $R3$ in MDNI.

The traces obtained from the open-aperture z-scan for all materials were straight as shown in Figure 5.16, and the two photon absorption (β) was effectively zero for all materials. This is expected as the very wide band gap of this material generally means that no two-photon

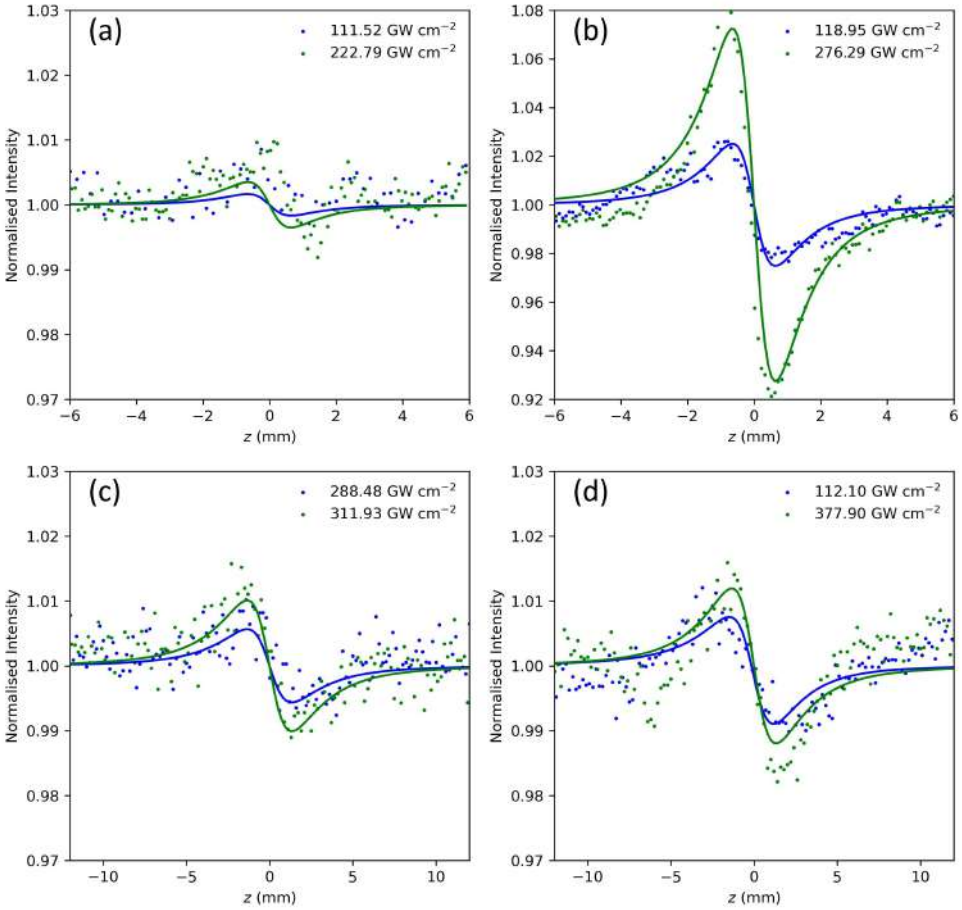

Figure 5.14 Closed-aperture z-scan of (a) DNI, (b) MDNI, (c) DNBr and (d) MDNBr. Dots are the measured data and the lines represent the data fit.

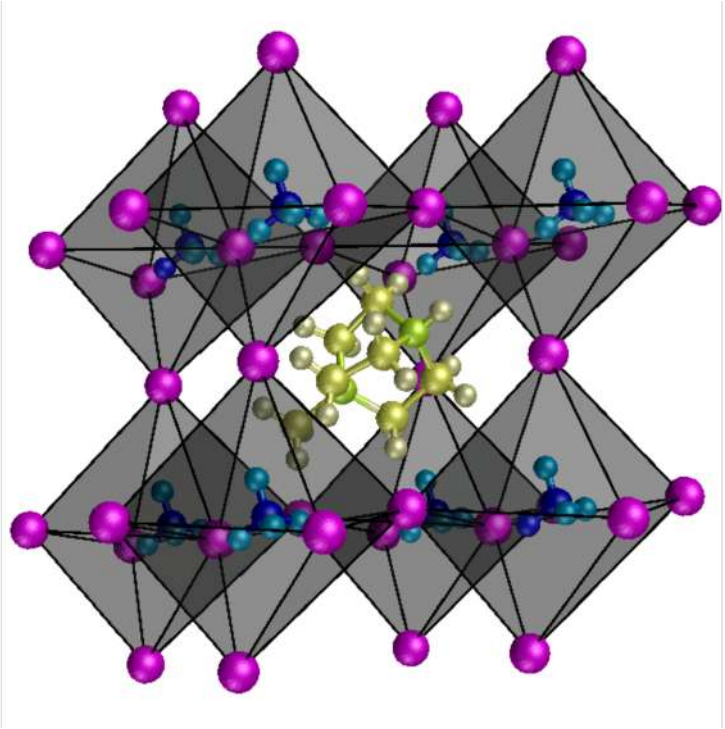

Figure 5.15 Crystal structure of MDNI.

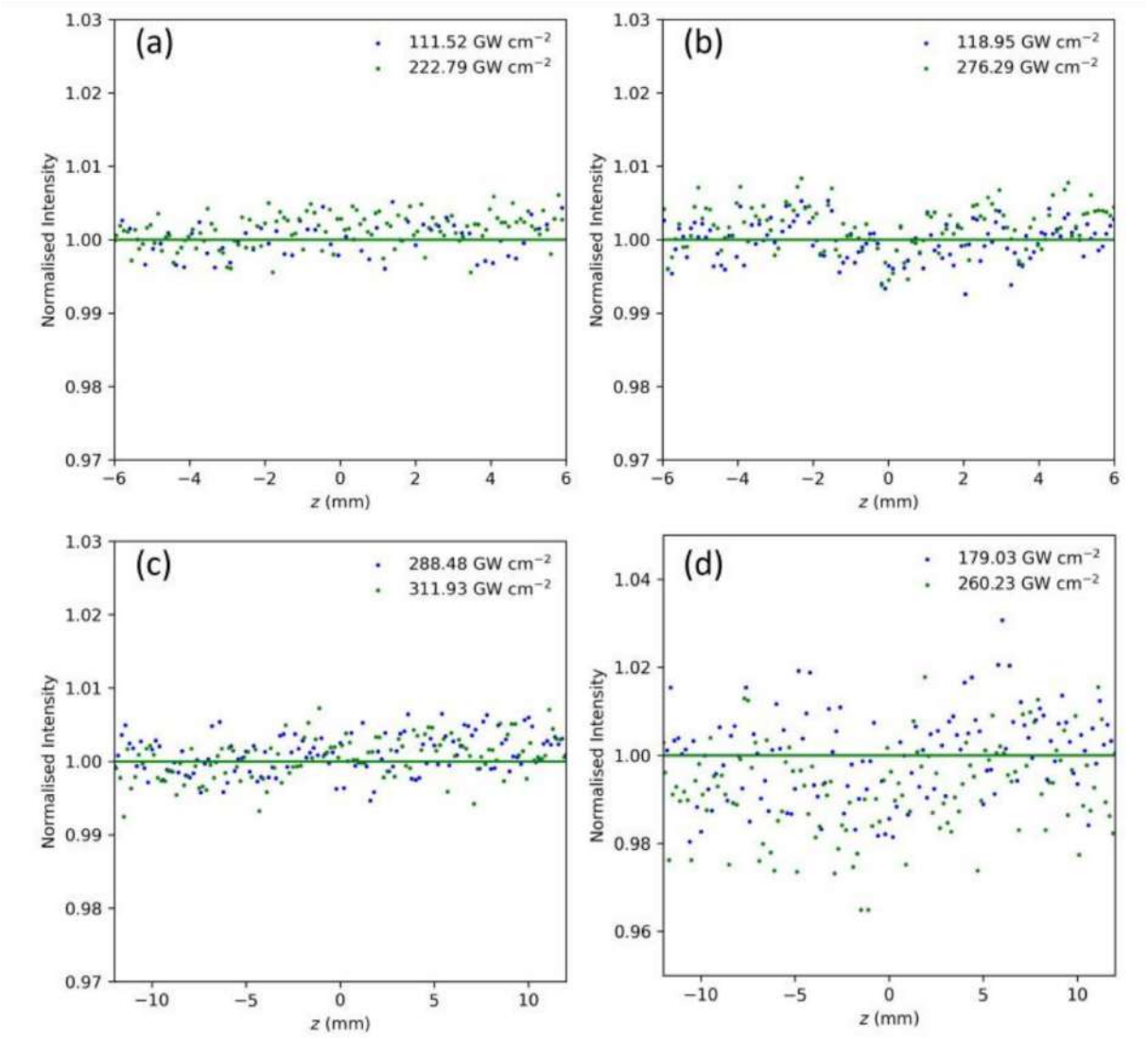

Figure 5.16 Open-aperture z-scan of (a) DNI, (b) MDNI, (c) DNBr and (d) MDNBr. Dots are the measured data and the lines represent the data fit.

absorption is expected above an excitation wavelength of 500 nm, thus allowing it to be used for frequency conversions in the visible region. As a result, the figure of merit (FOM$_{nl}$) for all materials measured is high (Table 5.2), the resolution limit of our instrument for β was set to 1×10^{-13} m W^{-1} ; therefore, these values are the lower bound.

Materials	n_2 ($m^2 W^{-1}$)	β ($m W^{-1}$)	FOM_{nl}	Band gap (eV)
DNI (DABCO-NH_4I_3)	3×10^{-18}	1×10^{-13}	>28	4.97
MDNI (Methyl-DABCO-NH_4I_3)	5.7×10^{-17}	1×10^{-13}	>537	5.12
DNBr (DABCO-NH_4Br_3)	4.3×10^{-18}	1×10^{-13}	>40	5.85
MDNBr (Methyl-DABCO-NH_4Br_3)	2.7×10^{-17}	1×10^{-13}	>254	5.02

Table 5.2 Optical properties of metal-free perovskites

5.6. Conclusions

The purpose of this chapter is to introduce, for the first time, the concept of metal-free perovskites as a class of material for nonlinear optical processes of third order. According to our results, the DNC crystal has a high intrinsic third-order nonlinearity. The results show that MDNX exhibit a high nonlinear refractive index than DNX, MDNI is 20 times higher than DNI and MDNBr is 6 times higher than DNBr. This provides further evidence supporting that the strong nonlinear optical response is originated from the distortion of the hexaiodide/hexabromide octahedra, which is induced by the dipole moment of Methyl-DABCO molecule. Furthermore, the optical absorption spectrum confirm their wide band gap nature (4.97 - 5.85 eV). This suggests that metal-free perovskites are of high potential in nonlinear optical applications, particularly in the visible and ultraviolet region. Along with their non-toxic property and easy solution processing, metal-free perovskites open the door for environmental friendly, inexpensive and efficient nonlinear optics.

Chapter 6. Perovskite Optical Fibre

Semiconductor core optical fibers have excellent electro-optical and nonlinear properties in a waveguiding architecture. Despite silica fibres remaining the most popular optical fibre, they have some disadvantages, such as low nonlinear optical coefficients, low electronic properties [167], and a limited transparency window. Because of these shortcomings, the search for new materials for optical fibre platforms has increased. Other glasses have become an interesting alternative to silica for the core material for certain applications. This is owing to the fact that they can have a transparency window extending into the mid-infrared and high optical nonlinearities [168] [169]. In terms of nonlinear optics applications, chalcogenide glasses are an excellent candidate as they have strong third-order nonlinear properties, but the application of these glasses has so far been limited by some issues like low chemical stability, low glass transition temperature and undergo thermal degradation when working with high optical power [170] [171] [172] [173] [174].

In recent years, semiconductor photonics has attracted considerable attention, and the compelling prospect of exploiting the exceptional optoelectronic properties of materials directly within the glass fibre geometry [175] [176]. Thus, the semiconducting optoelectronic fibre has emerged as a strong candidate for optoelectronic applications. fibres with semiconductor elements are defined as having one semiconductor element or more, usually in the core or cladding, along the path of optical waves transmitted in the fibre. In addition to their exceptional optical and electronic properties, these materials can have high nonlinear optical properties, which make them ideal for fibre-based all-optical signal processing and frequency generation. Optical fiber is one of the most significant dielectric waveguides. The planar dielectric waveguides can be manufactured using newly developed wet coating solutions [177]. A number of applications are possible for this technology, including monolayer antireflection (AR)coatings on silicon and multilayer complex AR coatings for specific wavelengths.

fibre core	n_2 ($m^2 W^{-1}$)	Band gap (eV)	ref
Silicon	1.8×10^{-17}	1.12	[183]
$MAPBr_3$	3.8×10^{-17}	2.18	[140]
MDNI	5.7×10^{-17}	5.12	[140]

Table 6.1 Semiconductor core fibre properties

In recent years, silicon photonics has received much attention due to the technology's potential applications from optical interconnects to biosensing [178]. It has been measured that the nonlinear refractive index of standard silica fibres is about $2.6 \times 10^{-20}\,m^2W^{-1}$, while that of crystalline silicon is $1.8 \times 10^{-17}\,m^2W^{-1}$ [179], showing that nonlinearities are a hundred times greater in silicon than in silica.

There have been several studies carried out on silicon core fibres (SCFs) that have shown it has nonlinear optical effects like multiphoton absorption [180], and four-wave mixing [181] [182]. The goal of this chapter is to produce an optical fibre with a perovskite (MDNI, $MAPbBr_3$) as the core. Perovskites exhibit a direct bandgap and a low defect density, which makes them highly efficient for emitting light. The single crystal form of perovskites has many advantages such as an intrinsic grain boundary-free structure, a longer carrier diffusion length, and enhanced environmental stability, resulting in improved optoelectronic device performance. Furthermore, single-crystal perovskite holds great promise for nonlinear optics and detectors because of their optoelectronic and nonlinear optical properties [116] [117] [117]. In addition, the nonlinear refractive index for conventional silica optical fibre is 1000 times lower than the nonlinear refractive index for $MAPbBr_3$ and MDNI, presenting the opportunity for efficient nonlinear devices. Furthermore, as silicon has a relatively narrow bandgap (Table 6.1), it cannot operate efficiently in the infrared band, so to move to infrared or even the UV region, a material with a wide bandgap would be needed. This is the reason that $MAPbBr_3$ and MDNI are potential materials for optical fibre platform.

6.1. Results and discussion of the perovskite optical fibre

6.2. Fabrication of the perovskite optical fibre

6.2.1. $MAPbBr_3$ solution and fabrication procedures of the capillary.

We proposed an inverse temperature crystallization method for the growth of $MAPbBr_3$ perovskite optical fibres. $MAPbBr_3$ crystal optical fibres were synthesized with 0.164 g of MABr and 0.536 g of $PbBr_2$ was dissolved in 1 mL of DMF by magnetic stirring at room temperature. The solution was filtered using a 0.45 µL polytetrafluoroethylene (PTFE) filter to produce a clear solution. 35 mm long capillary with cladding diameter of 145 µm and 5 µm diameter pore was dipped into the $MAPbBr_3$ solution. The optical fibre was heated from room temperature to 60 °C, then increased 10 °C every 12 h until it reached 100 °C.

6.2.2. Materials characterisation

Microscopic characterisation

Figure 6.1 shows a microscope image for filled $MAPbBr_3$ core fibre. $MAPbBr_3$ crystal inside the core is millimetres in length, which is not sufficient to measure transmission loss. It is believed that the small crystal was caused by using inverse temperature crystallization method, which was unsuccessful and it has been proven to be not effective. Solvent transport problems associated with inverse temperature crystallization restrict the length that the crystal can grow with a small core. The MDNI fibre was grown from a more traditional solution-cooling based crystallisation. This should permit core material to grow with orders of magnitude smaller dimensions without modifying or replacing silica capillaries with alternatives that are less compatible with optical fibre networks.

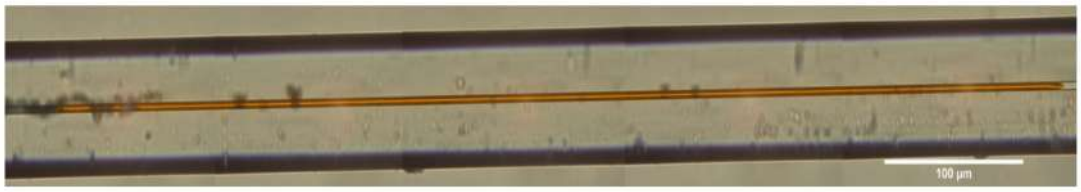

Figure 6.1 Microscopp image for filled $MAPbBr_3$ core fibre.

6.2.3. MDNI solution and fabrication procedures for the capillary

MDNI crystal optical fibres were synthesized with an MDNI solution that was prepared by dissolving 0.2 g of MDNI powder in 0.16 mL of DI water using magnetic stirring and placing it on the hotplate at 95 °C. A capillary with the desired inner dimensions (core-size) was placed into the solutions and allowed to be filled via capillary action. The solution was filtered using a 0.45 µL filter to produce a crystal clear solution. The tubes were then introduced into a homemade 'temperature-controlled oven' consisting of two metal plates and a spacer that was pre-warmed to 95 °C. For 24 hours, the filled capillaries were held at 95 °C in the oven to redissolve any crystals that formed during setup, and to initiate crystal growth at the edge of the capillary through evaporation. The fibre was then cooled down slowly from 95 °C to room temperature at a rate of 0.5 °C h^{-1} for the crystal's growth inside as shown in Figure 6.2. Capillary tubes exhibit higher concentrations at the edges, as water slowly evaporates, nucleating the crystal and promoting its slow growth. Depending on the capillary's core diameter, the cross-section of the perovskite fibre core can differ. Optical fibres with large and small core sizes were used to grow perovskite. Figure 6.3 a-b illustrate longitudinal sections of fibres with MDNI core diameters of (a) a 25 µm and (b) 5 µm, respectively.

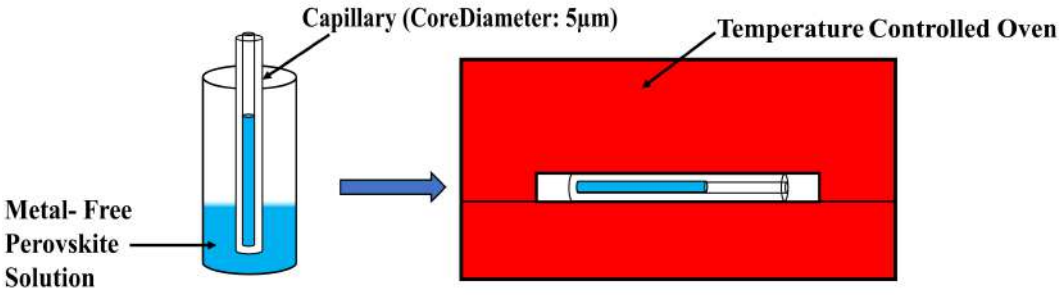

Figure 6.2 Fabrication of fibre scheme.

The end faces of the optical fibres can be polished using standard polishing papers to improve coupling efficiency in optical transmission measurements and for low-loss input and output light. Polishing papers were used from coarse grits to fine grits of 9 µm down to 0.3 µm, successive steps were taken to polish the fibre until the surface appeared perfectly smooth under the microscope. Figure 6.4 are microscope images of the polished 250 µm. The resulting fibre is difficult to polish and delamination of core material at the core/cladding interface was prevalent. Figure 6.5 shows a 5 µm MDNI core optical fibre in (a) reflection and (b) transmission light. It

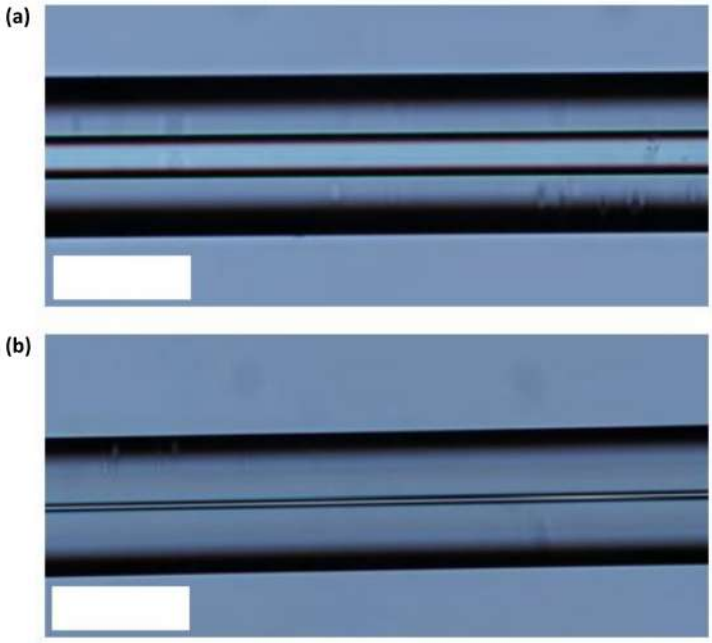

Figure 6.3 (a) A microscopic image of a 25 µm MDNI core fiber, scale bar 100 µm. (b) A microscopic image of a 5 µm MDNI core fiber, scale bar 100 µm.

has been found that when the optical fibre core diameter decreases, the perovskite fibre grows inside the core and the polishing process is less prone to sidewall delamination. In addition, optical images for polished cross sections of MDNI fibre of 5 µm indicates no air holes in the core/cladding, which allows accurate measurement of optical transmission. Since air holes create spots with a very high refractive index contrast, which subsequently produces a strong scattering of light as it passes through the MDNI core.

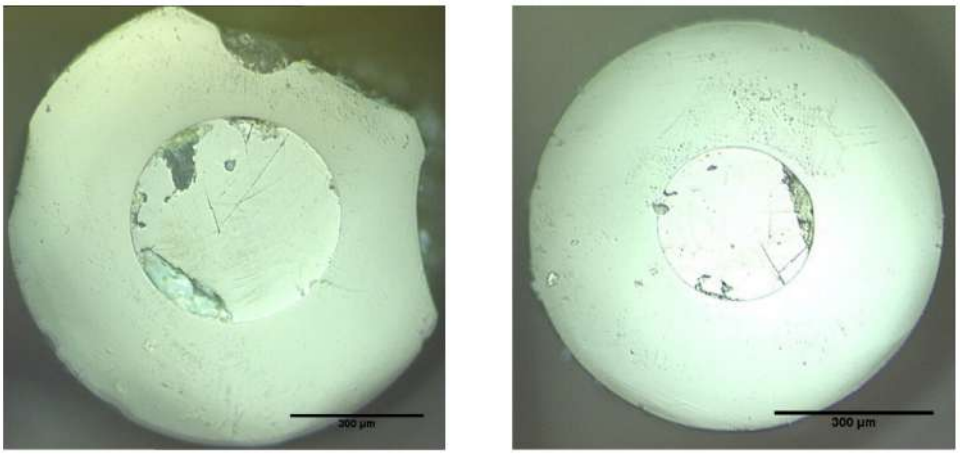

Figure 6.4 Images of the MDNI microscope after polishing with a larger size of core.

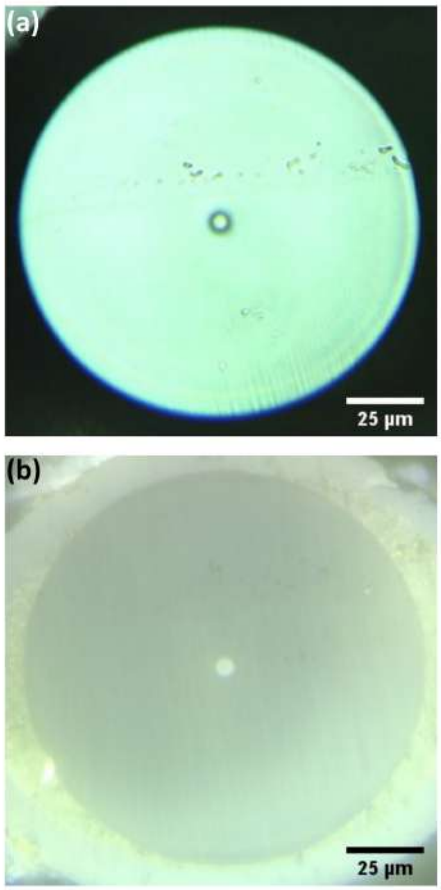

Figure 6.5 An optical images for polished cross-sections of MDNI fibre in (a) reflection and (b) transmission light.

6.3. Core material characterisation of MDNI optical fibres

Raman spectroscopy

Raman spectroscopy was conducted on the 5 µm MDNI fibre by shining a 532 nm laser through the fibre cladding onto the core and collecting the scattered light, and this spectrum was compared to that of a single crystal of MDNI as shown in Figure 6.6a. In the MDNI fibre as well as the single crystal, the low-frequency Raman modes between 80 cm^{-1} and 400 cm^{-1}, are assigned to the lattice modes, which have a broad weak signal due to the dynamic disorder of the organic ions [184]. The strong sharp peaks that appear between 600 cm^{-1} and 1200 cm^{-1} indicate that crystallinity of the core material is high, as revealed by the comparison between the MDNI single crystal and the MDNI core fiber. Lorentzian fitting of the peak at 696 $cm^{-1}$for each spectrum shows that the full-widths at half-maxima of MDNI core fiber and MDNI single crystal sample are similar, which measured to be 3.11 cm^{-1} and 3.1 cm^{-1}, respectively as shown in Figure 6.6b. The MDNI optical fiber appears to be highly crystalline based on this

result. As high crystallinity is further evidenced by the symmetry of the peak, asymmetry is a sign that there is a high concentration of crystalline defects.

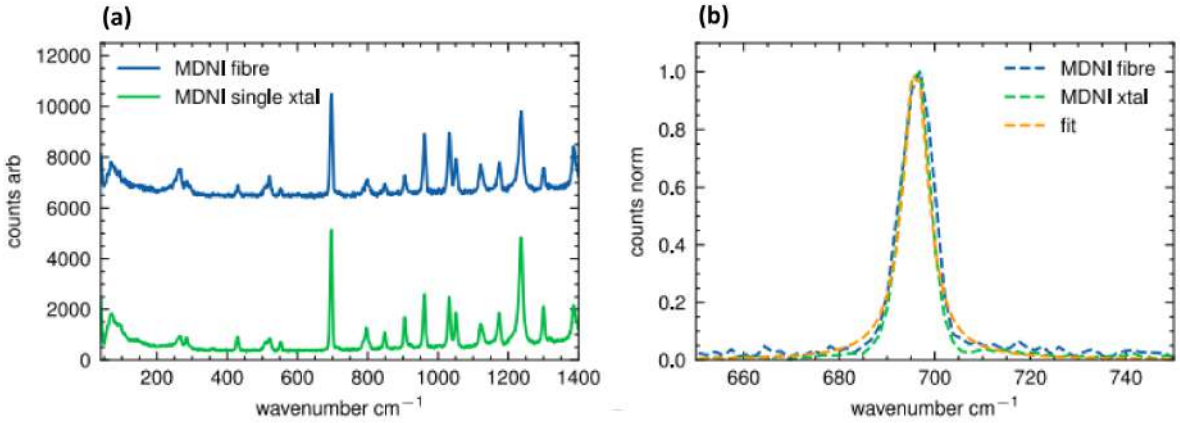

Figure 6.6 a Raman spectra of MDNI optical fiber.

6.3.1. XRD of core material

The crystal was mounted in a Lindemann tube. MDNI core sample data was collected using an Oxford Cryosystems low-temperature device operated at T= 100(2) K and a Rigaku FRE+ equipped with VHF Varimax confocal mirrors, an AFC12 goniometer, and a HyPix 6000 detector diffractometer. The MDNI core fibre of 5 µm was analyzed using X-ray diffraction in order to determine the purity of the phase and degree of crystallinity. The data has been compared with the standard database and powder pattern to confirm the crystal structure, Results of the X-ray diffraction on the MDNI core optical fibre are shown in Figure 6.7. These results clearly prove that the core is pollycrystalline MDNI with no other phases. In addition, the narrow peak width indicates a high degree of crystallinity. The structure was determined to be trigonal in the R_3 (No. 146) space group with a lattice parameter of a = 9.7018(2) Å, b = 9.7018(2) Å, and c = 13.4526(4) Å, which consistent with that expected for MDNI [185].

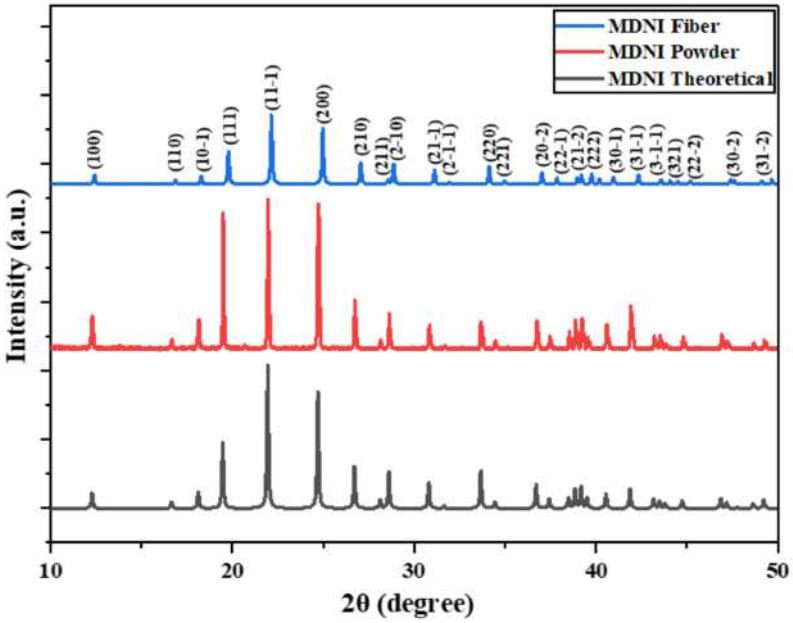

centering

Figure 6.7 X-ray diffraction spectrum for the MDNI core optical fibre with core size about 5 µm.

6.3.2. Optical Characterisation

Optical transmission set-up

The optical transmission loss was measured at 1550 nm with the set-up designed for fibre length-dependent loss measurements, which is represented in Figure 6.8. The loss measurement was done using the cutback method. A continuous wave laser source, which yielded an average power of P_{in}= 9.05 mW was used. A continuous-wave laser instead of a pulse laser source in order to prevent damage to the surface sample that may result from the high power of pulse lasers and to suppress any nonlinearity. The selected wavelength is launched into the MDNI core using a 40x microscope objective lens with a NA = 0.74, which corresponds to a spot size of about 5 µm that matches the core diameter of the fibre. The numerical aperture must match the MDNI core fibre or be smaller to achieve optimal coupling and minimize the excitation in the cladding. The numerical aperture is set at this value to maximize the collection of input power. It is important to have a small core size in order for there to be light transmission and that the intensity of the light is high enough to be able to be excited by the nonlinearity of the core materials. The light reflected from the sample surface is directed towards the infrared camera through a beam splitter located in front of the input lens. This allows the sample surface to be observed. During the experiment, the output is collected and directed into an infrared camera by

a 10x microscope objective lens. Once the coupling has been optimized, output powers were measured using the power meter, and this process was repeated at different lengths of fibre.

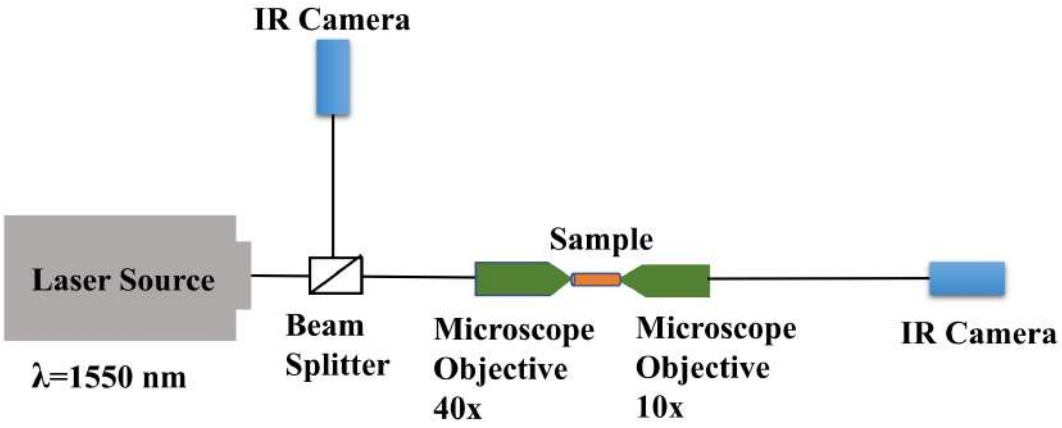

Figure 6.8 Schematic of optical transmission set-up used for transmission loss measurements.

Perovskite optical fibre characterisation

Infrared and visible images of the transmitted light through 1 cm length of the 5 µm MDNI optical fibre were taken and are shown in Figure 6.9. The wavelengths used for these measurements were 633 nm and 1550 nmrespectively. As a result, MDNI optical fibre is capable of high bandwidth.

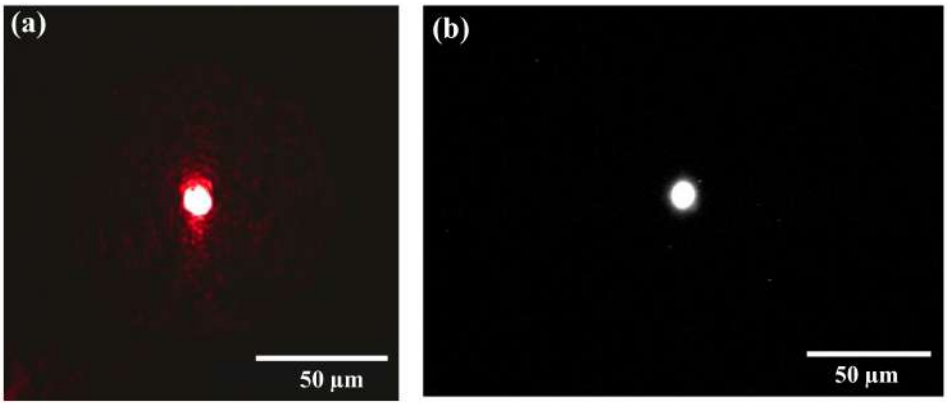

Figure 6.9 Output images of 5 µm core MDNI fibre transmission using (a) visible light at 633 nm, (b) an infrared light at 1550 nm.

Optical characterization of MDNI optical fibre of 5 µm at telecommunications wavelength 1550 nm has been conducted. The refractive index of the core material is n_1 = 1.58 at 1550 nm and the V -number given by

$$V = \frac{2\pi}{\lambda} a \sqrt{(n_{core})^2 - (n_{cladding})^2} \tag{6.1}$$

is 6.48, Where λ is the operating wavelength, a is the radius of the MDNI core (2.5 µm) and the cladding refractive index is $n_2 = 1.44$. When V = 6.48, the MDNI fibre can support six LP modes since $\Delta n \ll 1$ are low order modes. Simulations were undertaken to see which modes are guided as shown in Figure 6.10. For the fiber simulation, Comsol's finite element method was chosen. Mode analyses are performed on circular dielectric layer structures using this method. In order to describe the layers, an outer diameter as well as real and imaginary parts of the refractive index are given for each layer. In the available materials section, MDNI material was shown. In the simulation parameters section 1.55 µm was used for the operating wavelength and 6.48 was used as the number of modes that should be searched for.

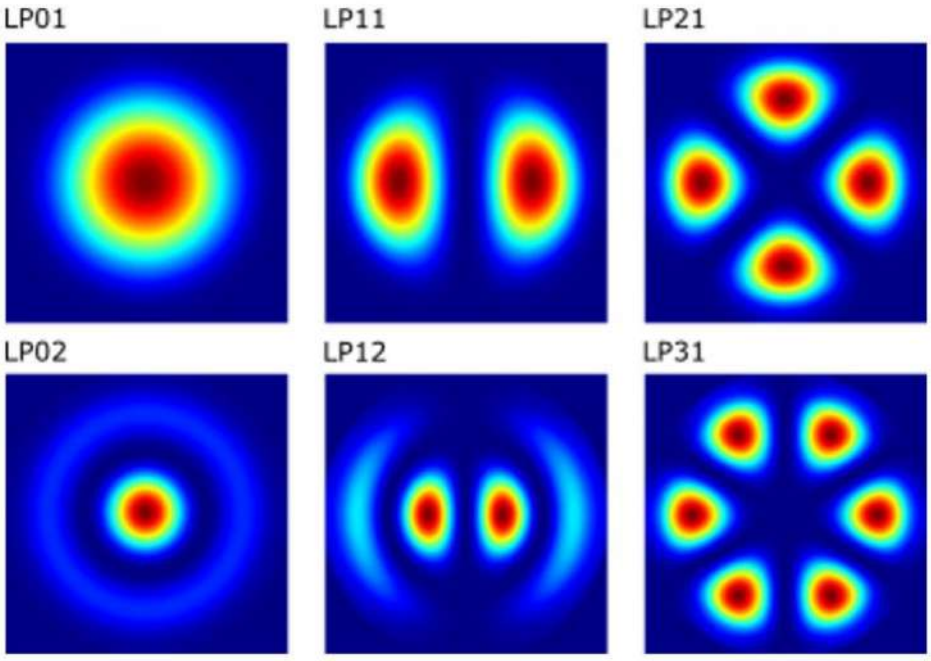

Figure 6.10 A mode profile of 5 µm MDNI core optical fibre at a wavelength of 1550 nm. A frame with a size of 8 microns by 8 microns is used.

Near-field modes in fiber were visualized using an infrared camera. LP01, LP11, and LP21 modes are experimentally imaged in Figures 6.11 a,b,c that are well matched with the simulated modes of the same fibre as shown in Figures 6.11 d,e,f. When the input beam is launched off-axis to the core, higher order modes are isolated only and the coupling occurs predominantly into the fundamental LP01 mode.

The simulation is used to get the optimize design for the waveguide for the MDNI optical fiber. The dispersion measurements can reveal that how optical signals are distorted as they travel across optical fibres. Figure 6.12 a shows the dispersion vs core radius for SMF-28 and MDNI

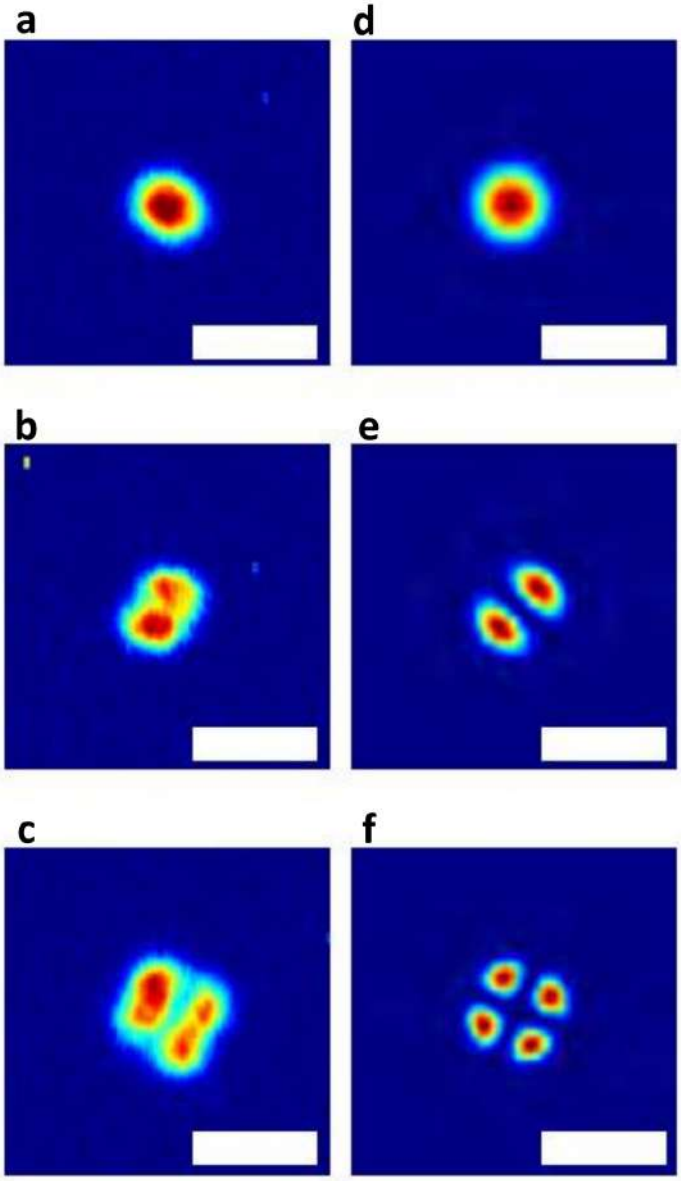

Figure 6.11 A mode profile of 5 µm MDNI core optical fibre at a wavelength of 1550 nm, it include LP01 mode **a** (experimental) and **d** (numerical simulation), the LP11 mode **b** (experimental) and **e** (numerical simulation), and the LP21 mode **c** (measured) and **f** (numerical simulation), with scale bars of 10 µm

fiber. The dispersion is measured in ps/(nm)(km). The range is given from -1000 to 500 ps/nm.km. The core radius is in µm and the range is between -1.8 to 5.5 µm. From the Figure 6.12 a, the dispersion is zero at 1 µm. At the larger diameters from 1 to 5 µm the dispersion is still not extremely high. Because of the low dispersion of light waves, optical fibers perform well and the wave is not affected by any variations in its actual propagation through the fiber. From Figure 6.12 b we can see the effective index of the mode for a particular core diameter, showing that the fibre supports just a few modes and is single mode only for a 1.7 µm core diameter.

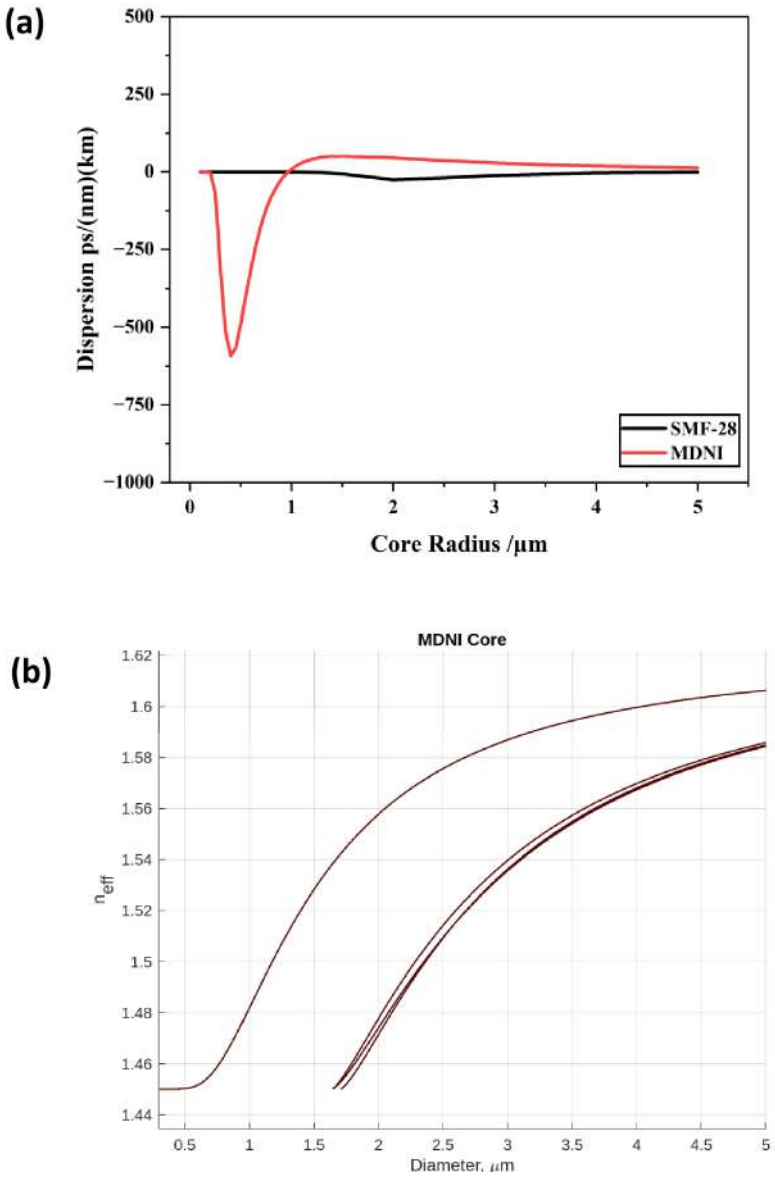

Figure 6.12 (a) Dispersion vs core radius for SMF-28 and MDNI, (b) Effective refractive index vs diameter for MDNI at 5 µm

6.4. Cutback method

A cutback method can be applied to determine the total attenuation of an optical fibre. These measurements provide the highest level of accuracy and resolution. In order to perform cutback measurements, there are four steps involved; the first step is to measure the transmission on a long length of fibre under test, and the second requires that the test fibre be cut back by a known length. The third is to repeat the measurement on the shorter length of the fibre. The measurement should then be repeated to get an accurate value. The loss of the fibre is given by

the equation

$$\alpha(dB/km) = 10\frac{1}{z}\log(\frac{P_0}{P_z}) \tag{6.2}$$

Where P_0 is the optical power at the origin ($z = 0$) and P_z is the optical power at distance z.

Transmission Loss

Having a low loss is crucial for optical fibre, either for signal transmission or for achieving nonlinear effects. As demonstrated in silicon core fibre, where a low loss of less than 1 dB/cm is required for a 10 mm long fibre to show nonlinear effect (spectral broadening and/or modulations [112] [186]. The measured transmission loss of MDNI fibre is about 10 dB/cm, which is significantly higher than the requirement, and therefore no nonlinear effect can, yet, be observed. It has been found that the value of transmission loss presented here differs from the value found in literature [187]. The high loss is believed to be due to the scattering and absorption at the grain boundaries and the defects in the MDNI crystal. Also, given the high loss, a much longer crystal might be needed in order to achieve the nonlinear effects. However, using the current fabrication method, the longest crystal that could be grown is about 1 - 3 cm. Further improvement on the fabrication method or crystal growth would be needed.
As MDNI is soluble in water, there is concern that the MDNI would degrade during the polishing because of the moisture in air. There was no observable degradation on the MDNI surface after polishing and the surface quality remained comparable after each step of the cutback method. However, in the case of using a capillary with a larger core (as shown earlier in this chapter), there are voids in the crystal and between the crystal-cladding interface.

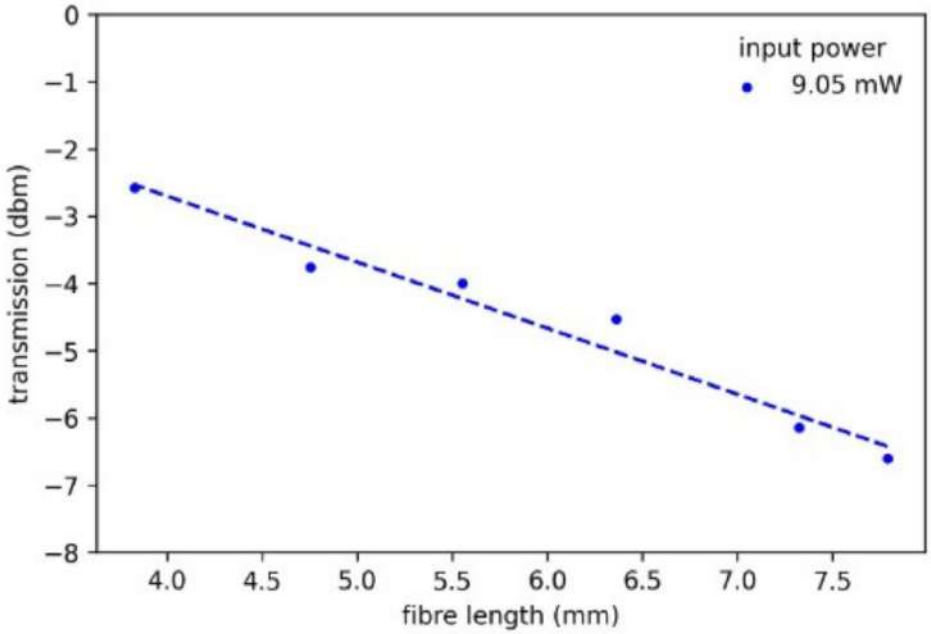

Figure 6.13 The transmission loss for MDNI fibre using the standard cutback method.

6.5. Conclusions

This chapter discusses the growth of $MAPbBr_3$ and MDNI crystals within capillaries in order to create an optical fibre-like waveguide. According to our results, the MDNI fibre has high transmission losses. It has been measured that the transmission loss of MDNI fibre is approximately 10 dB/cm, which is significantly higher than the requirement, and therefore no nonlinear effects can be observed, such as spectral broadening. In order to explain the high loss, it is believed that there is scattering and absorption at the grain boundaries of the MDNI crystals, as well as defects within the crystals. On the other hand, in the case of $MAPbBr_3$ are millimetres in length, which is not sufficient to measure transmission loss.

Chapter 7. Conclusion and Future work

7.1. Conclusion

The third-order nonlinear properties of a range of hybrid and metal-free perovskites have been characterised using the z-scan technique. The nonlinear responses of hybrid perovskites have been studied extensively. This study revealed that perovskite crystal with larger anion demonstrates a stronger third-order nonlinear response, and it is believed that the electrons are more susceptible to the incident laser leading to a stronger response.

Although lead-based hybrid perovskites possess strong nonlinear responses, their toxic nature makes them undesirable, particularly from the environmental point of view. Also, their narrow band gaps contribute to the high nonlinear absorption, which reduces their overall performance for nonlinear applications. Metal-free perovskites have been identified as excellent alternatives. These materials retain the ABX_3 structure, with both A and B sites occupied by molecular cations and X is the halides. DABCO-NH_3-X_3 and MDABCO-NH3-X3 are of interest in this study. This group of materials possess optical band gap of above 5 eV, which is significantly higher than that of typical hybrid perovskites and therefore minimises the nonlinear absorption. In addition, MDABCO-$NH3_3$-I_3 and MDABCO-NH_3-Br_3 demonstrated comparable nonlinear response to $MAPbBI_3$, in the order of $10 \times 10^{-17}\,m^2\,W^{-1}$. It is believed that the incorporation of MDABCO molecules induces distortions in the perovskite structure and leads to a strong nonlinear response. Considering the nonlinear figure of merit, MDABCO-NH_3-I_3 is nearly 10000 times higher than that of $MAPbI_3$ and indicates their high potential for nonlinear applications.

In an attempt to emulate the highly successful semiconductor-core optical fibre, MDNI crystals have been grown in a capillary to form MDNI-core fibre. However, due to the high transmission loss of about 10 dB/cm, no nonlinear effects have been observed. The high loss is believed to be originated from the scattering and absorption at the grain boundaries. MAPbBr3 fibre have also

been tried but the length of the crystal is limited in the millimetre range, which is not sufficient for measuring the loss

7.2. Future work

In this thesis, we investigate the third-order nonlinear properties of metal halide and metal-free perovskites using standard z-scan techniques. In chapter 4,5, the third-order nonlinear properties of a range of metal halide and metal-free perovskites have been characterised using the standard z-scan technique. In the case of metal halide perovskite, the results of this study showed that perovskite crystals with iodide as an anion demonstrate a stronger third-order nonlinear response, while in the case of metal-free perovskite the perovskite crystals where chloride is the anion display a stronger third-order nonlinear response. Future work will focus on methods of improving the nonlinearity of perovskite materials, for example by changing the cations in the perovskite structure, such as caesium (Cs), formamidinium (FA), or methylammonium (MA), which could be of interest. There will be a wide range of C_sPbX_3, $FAPbX_3$, and $MAPbX_3$ families for which optical properties have been fabricated, which greatly increases the probability of improved nonlinearity since the metal cation size is important in governing regularities of the formation of perovskites. In chapter 6, we discussed how perovskites grow in capillaries to create waveguides that resemble optical fibres. The results of this study showed that MDNI crystals can be grown in a capillary to form MDNI-core fibre. However, improvement in losses is required for efficient nonlinear optics applications. The next phase of research should focus on improving the crystal quality of the perovskites as grown in the capillaries. There are a number of ways of post-processing semiconductor optical fibres that might be investigated for example recrystallization using laser annealing, which can yield fibres with minimal optical losses.

References

[1] Hui-Seon Kim, Sang Hyuk Im, and Nam-Gyu Park. Organolead halide perovskite: new horizons in solar cell research. *The Journal of Physical Chemistry C*, 118(11):5615–5625, 2014.

[2] Tanghao Liu, Ke Chen, Qin Hu, Rui Zhu, and Qihuang Gong. Inverted perovskite solar cells: progresses and perspectives. *Advanced Energy Materials*, 6(17):1600457, 2016.

[3] Thomas W Kasel, Zeyu Deng, Austin M Mroz, Christopher H Hendon, Keith T Butler, and Pieremanuele Canepa. Metal-free perovskites for non linear optical materials. *Chemical Science*, 10(35):8187–8194, 2019.

[4] John M Senior and M Yousif Jamro. *Optical fiber communications: principles and practice*. Pearson Education, 2009.

[5] Rod Bottom. Thermogravimetric analysis. *Principles and applications of thermal analysis*, 1(906):87–118, 2008.

[6] César Leyva-Porras, Pedro Cruz-Alcantar, Vicente Espinosa-Solís, Eduardo Martínez-Guerra, Claudia I Piñón-Balderrama, Isaac Compean Martínez, and María Z Saavedra-Leos. Application of differential scanning calorimetry (dsc) and modulated differential scanning calorimetry (mdsc) in food and drug industries. *Polymers*, 12(1):5, 2019.

[7] Yuliang Wang, Tongda Lu, Xiaolai Li, and Huimin Wang. Automated image segmentation-assisted flattening of atomic force microscopy images. *Beilstein journal of nanotechnology*, 9(1):975–985, 2018.

[8] Patrycja Makuła, Michał Pacia, and Wojciech Macyk. How to correctly determine the band gap energy of modified semiconductor photocatalysts based on uv–vis spectra, 2018.

[9] Youliang Jin, Baoan Song, Zhitai Jia, Yinan Zhang, Changgui Lin, Xunsi Wang, and Shixun Dai. Improvement of swanepoel method for deriving the thickness and the optical properties of chalcogenide thin films. *Optics express*, 25(1):440–451, 2017.

[10] Sjoerd A. Veldhuis, Pablo P. Boix, Natalia Yantara, Mingjie Li, Tze Chien Sum, Nripan Mathews, and Subodh G. Mhaisalkar. Perovskite materials for light-emitting diodes and lasers. *Advanced Materials*, 28(32):6804–6834, 2016.

[11] Mahshid Ahmadi, Ting Wu, and Bin Hu. A review on organic–inorganic halide perovskite photodetectors: Device engineering and fundamental physics. *Advanced Materials*, 29(41):1605242, sep 2017.

[12] Zijun Yi, Najib Haji Ladi, Xuxia Shai, Hao Li, Yan Shen, and Mingkui Wang. Will organic–inorganic hybrid halide lead perovskites be eliminated from optoelectronic applications? *Nanoscale Adv.*, 1:1276–1289, 2019.

[13] Ajay Kumar Jena, Ashish Kulkarni, and Tsutomu Miyasaka. Halide perovskite photovoltaics: Background, status, and future prospects. *Chemical Reviews*, 119(5):3036–3103, mar 2019.

[14] Qing Zhang, Qiuyu Shang, Rui Su, T. Thu Ha Do, and Qihua Xiong. Halide perovskite semiconductor lasers: Materials, cavity design, and low threshold. *Nano Letters*, 21(5):1903–1914, 2021. PMID: 33435686.

[15] Basanth S. Kalanoor, Laxman Gouda, Ronen Gottesman, Shay Tirosh, Eynav Haltzi, Arie Zaban, and Yaakov R. Tischler. Third-order optical nonlinearities in organometallic methylammonium lead iodide perovskite thin films. *ACS Photonics*, 3(3):361–370, 2016.

[16] Rui Zhang, Jiandong Fan, Xing Zhang, Haohai Yu, Huaijin Zhang, Yaohua Mai, Tianxiang Xu, Jiyang Wang, and Henry J. Snaith. Nonlinear optical response of organic–inorganic halide perovskites. *ACS Photonics*, 3(3):371–377, 2016.

[17] Isaac Suárez, Marta Vallés-Pelarda, Andrés F. Gualdrón-Reyes, Iván Mora-Seró, A. Ferrando, Humberto Michinel, José Ramón Salgueiro, and Juan P. Martínez Pastor. Outstanding nonlinear optical properties of methylammonium- and cs-pbx3 (x = br, i, and br–i) perovskites: Polycrystalline thin films and nanoparticles. *APL Mater.*, 7(4):041106, 2019.

[18] Jialiang Xu, Xinyue Li, Jianbo Xiong, Chunqing Yuan, Sergey Semin, Theo Rasing, and Xian-He Bu. Halide perovskites for nonlinear optics. *Advanced Materials*, 32(3):1806736, mar 2019.

[19] Hamad Syed, Wenchi Kong, Venkatesh Mottamchetty, Kwang Jin Lee, Weili Yu, Venugopal Rao Soma, Jianjun Yang, and Chunlei Guo. Giant nonlinear optical response in triple cation halide mixed perovskite films. *Advanced Optical Materials*, 8(7):1901766, 2020.

[20] Yixuan Zhou, Yuanyuan Huang, Xinlong Xu, Zeyu Fan, Jacob B. Khurgin, and Qihua Xiong. Nonlinear optical properties of halide perovskites and their applications. *Applied Physics Reviews*, 7(4):041313, 2020.

[21] Weili Shen, Jun Chen, Jinqiang Wu, Xiaoming Li, and Haibo Zeng. Nonlinear optics in lead halide perovskites: Mechanisms and applications. *ACS Photonics*, 8(1):113–124, dec 2021.

[22] Aurélien M. A. Leguy, Pooya Azarhoosh, M. Isabel Alonso, Mariano Campoy-Quiles, Oliver J. Weber, Jizhong Yao, Daniel Bryant, Mark T. Weller, Jenny Nelson, Aron Walsh, Mark van Schilfgaarde, and Piers R. F. Barnes. Experimental and theoretical optical properties of methylammonium lead halide perovskites. *Nanoscale*, 8:6317–6327, 2016.

[23] Heng-Yun Ye, Yuan-Yuan Tang, Peng-Fei Li, Wei-Qiang Liao, Ji-Xing Gao, Xiu-Ni Hua, Hu Cai, Ping-Ping Shi, Yu-Meng You, and Ren-Gen Xiong. Metal-free three-dimensional perovskite ferroelectrics. *Science*, 361(6398):151–155, 2018.

[24] Hui Wang, Huihui Liu, Zeyu Zhang, Zihan Liu, Zhenlong Lv, Tongwei Li, Weiwei Ju, Haisheng Li, Xiaowu Cai, and Han Han. Large piezoelectric response in a family of metal-free perovskite ferroelectric compounds from first-principles calculations. *npj Computational Materials*, 5(1):17, Feb 2019.

[25] Michael G. Ehrenreich, Zhixin Zeng, Stefan Burger, Mark R. Warren, Michael W. Gaultois, Jin-Chong Tan, and Gregor Kieslich. Mechanical properties of the ferroelectric metal-free perovskite [mdabco](nh4)i3. *Chem. Commun.*, 55:3911–3914, 2019.

[26] Jian-Jun Wang, Daniel Fortino, Bo Wang, Xinye Zhao, and Long-Qing Chen. Extraordinarily large electrocaloric strength of metal-free perovskites. *Advanced Materials*, 32(7):1906224, 2020.

[27] Xin Song, Qingyue Cui, Yucheng Liu, Zhuo Xu, Hagai Cohen, Chuang Ma, Yuanyuan Fan, Yunxia Zhang, Haochen Ye, Zhanhui Peng, Ruipeng Li, Yonghua Chen, Jianpu Wang, Huaming Sun, Zhou Yang, Zhike Liu, Zupei Yang, Wei Huang, Gary Hodes, Shengzhong (Frank) Liu, and Kui Zhao. Metal-free halide perovskite single crystals with very long charge lifetimes for efficient x-ray imaging. *Advanced Materials*, 32(42):2003353, 2020.

[28] Xin Song, Gary Hodes, Kui Zhao, and Shengzhong (Frank) Liu. Metal-free organic halide perovskite: A new class for next optoelectronic generation devices. *Advanced Energy Materials*, 11(11):2003331, 2021.

[29] Jie Bie, Dai-Bei Yang, Ming-Gang Ju, Qiang Pan, Yu-Meng You, Wei Fa, Xiao Cheng Zeng, and Shuang Chen. Molecular design of three-dimensional metal-free a(nh4)x3 perovskites for photovoltaic applications. *JACS Au*, 1(4):475–483, 2021.

[30] Rongzhen Gao, Xiaoming Shi, Jing Wang, Guangzu Zhang, and Houbing Huang. Designed giant room-temperature electrocaloric effects in metal-free organic perovskite [mdabco](nh4)i3 by phase–field simulations. *Advanced Functional Materials*, 31(38):2104393, 2021.

[31] Qingyue Cui, Xin Song, Yucheng Liu, Zhuo Xu, Haochen Ye, Zhou Yang, Kui Zhao, and Shengzhong (Frank) Liu. Halide-modulated self-assembly of metal-free perovskite single crystals for bio-friendly x-ray detection. *Matter*, 4(7):2490–2507, 2021.

[32] Thomas W. Kasel, Zeyu Deng, Austin M. Mroz, Christopher H. Hendon, Keith T. Butler, and Pieremanuele Canepa. Metal-free perovskites for non linear optical materials. *Chem. Sci.*, 10:8187–8194, 2019.

[33] Ziyong Cheng and Jun Lin. Layered organic–inorganic hybrid perovskites: structure, optical properties, film preparation, patterning and templating engineering. *CrystEngComm*, 12(10):2646–2662, 2010.

[34] Nada F Atta, Ahmed Galal, and Ekram H El-Ads. Perovskite nanomaterials–synthesis, characterization, and applications. *Perovskite Materials–Synthesis, Characterisation, Properties, and Applications; Pan, L., Ed*, pages 107–151, 2016.

[35] Aurélien MA Leguy, Yinghong Hu, Mariano Campoy-Quiles, M Isabel Alonso, Oliver J Weber, Pooya Azarhoosh, Mark Van Schilfgaarde, Mark T Weller, Thomas Bein, Jenny Nelson, et al. Reversible hydration of ch3nh3pbi3 in films, single crystals, and solar cells. *Chemistry of Materials*, 27(9):3397–3407, 2015.

[36] Qi Wang, Bo Chen, Ye Liu, Yehao Deng, Yang Bai, Qingfeng Dong, and Jinsong Huang. Scaling behavior of moisture-induced grain degradation in polycrystalline hybrid perovskite thin films. *Energy & Environmental Science*, 10(2):516–522, 2017.

[37] Ming-Gang Ju, Min Chen, Yuanyuan Zhou, Jun Dai, Liang Ma, Nitin P Padture, and Xiao Cheng Zeng. Toward eco-friendly and stable perovskite materials for photovoltaics. *Joule*, 2(7):1231–1241, 2018.

[38] Aslihan Babayigit, Anitha Ethirajan, Marc Muller, and Bert Conings. Toxicity of organometal halide perovskite solar cells. *Nature materials*, 15(3):247–251, 2016.

[39] Cherie R Kagan, David B Mitzi, and Christos D Dimitrakopoulos. Organic-inorganic hybrid materials as semiconducting channels in thin-film field-effect transistors. *Science*, 286(5441):945–947, 1999.

[40] Konstantinos Chondroudis and David B Mitzi. Electroluminescence from an organic-inorganic perovskite incorporating a quaterthiophene dye within lead halide perovskite layers. *Chemistry of materials*, 11(11):3028–3030, 1999.

[41] Nobuhiko Sarukura, Hidetoshi Murakami, Elmer Estacio, Shingo Ono, Riadh El Ouenzerfi, Marilou Cadatal, Takeshi Nishimatsu, Noriaki Terakubo, Hiroshi Mizuseki, Yoshiyuki Kawazoe, et al. Proposed design principle of fluoride-based materials for deep ultraviolet light emitting devices. *Optical Materials*, 30(1):15–17, 2007.

[42] Priyanka Roy, Numeshwar Kumar Sinha, Sanjay Tiwari, and Ayush Khare. A review on perovskite solar cells: Evolution of architecture, fabrication techniques, commercialization issues and status. *Solar Energy*, 198:665–688, 2020.

[43] Caleb C Boyd, Rongrong Cheacharoen, Tomas Leijtens, and Michael D McGehee. Understanding degradation mechanisms and improving stability of perovskite photovoltaics. *Chemical reviews*, 119(5):3418–3451, 2018.

[44] Dong Myung Jang, Kidong Park, Duk Hwan Kim, Jeunghee Park, Fazel Shojaei, Hong Seok Kang, Jae-Pyung Ahn, Jong Woon Lee, and Jae Kyu Song. Reversible halide exchange reaction of organometal trihalide perovskite colloidal nanocrystals for full-range band gap tuning. *Nano letters*, 15(8):5191–5199, 2015.

[45] Jin Hyuck Heo, Sang Hyuk Im, Jun Hong Noh, Tarak N Mandal, Choong-Sun Lim, Jeong Ah Chang, Yong Hui Lee, Hi-jung Kim, Arpita Sarkar, Md K Nazeeruddin, et al. Efficient inorganic–organic hybrid heterojunction solar cells containing perovskite compound and polymeric hole conductors. *Nature photonics*, 7(6):486–491, 2013.

[46] Akihiro Kojima, Kenjiro Teshima, Yasuo Shirai, and Tsutomu Miyasaka. Organometal halide perovskites as visible-light sensitizers for photovoltaic cells. *Journal of the American Chemical Society*, 131(17):6050–6051, 2009.

[47] Woon Seok Yang, Byung-Wook Park, Eui Hyuk Jung, Nam Joong Jeon, Young Chan Kim, Dong Uk Lee, Seong Sik Shin, Jangwon Seo, Eun Kyu Kim, Jun Hong Noh, et al. Iodide management in formamidinium-lead-halide–based perovskite layers for efficient solar cells. *Science*, 356(6345):1376–1379, 2017.

[48] Ronald G Larson and Timothy J Rehg. Spin coating. In *Liquid film coating*, pages 709–734. Springer, 1997.

[49] Nam Joong Jeon, Jun Hong Noh, Young Chan Kim, Woon Seok Yang, Seungchan Ryu, and Sang Il Seok. Solvent engineering for high-performance inorganic–organic hybrid perovskite solar cells. *Nature materials*, 13(9):897–903, 2014.

[50] Kira L Gardner, Jeffrey G Tait, Tamara Merckx, Weiming Qiu, Ulrich W Paetzold, Lucinda Kootstra, Manoj Jaysankar, Robert Gehlhaar, David Cheyns, Paul Heremans, et al. Nonhazardous solvent systems for processing perovskite photovoltaics. *Advanced Energy Materials*, 6(14):1600386, 2016.

[51] Fei Huang, Mengjie Li, Peter Siffalovic, Guozhong Cao, and Jianjun Tian. From scalable solution fabrication of perovskite films towards commercialization of solar cells. *Energy & Environmental Science*, 12(2):518–549, 2019.

[52] Yue Zhang, Haiming Zhang, Xiaohui Zhang, Lijuan Wei, Biao Zhang, Yuxuan Sun, Guangyuan Hai, and Yujie Li. Major impediment to highly efficient, stable and low-cost perovskite solar cells. *Metals*, 8(11):964, 2018.

[53] Yehao Deng, Edwin Peng, Yuchuan Shao, Zhengguo Xiao, Qingfeng Dong, and Jinsong Huang. Scalable fabrication of efficient organolead trihalide perovskite solar cells with doctor-bladed active layers. *Energy & Environmental Science*, 8(5):1544–1550, 2015.

[54] Qiufeng Ye, Yang Zhao, Shaiqiang Mu, Fei Ma, Feng Gao, Zema Chu, Zhigang Yin, Pingqi Gao, Xingwang Zhang, and Jingbi You. Cesium lead inorganic solar cell with efficiency beyond 18% via reduced charge recombination. *Advanced materials*, 31(49):1905143, 2019.

[55] Qingfeng Dong, Yanjun Fang, Yuchuan Shao, Padhraic Mulligan, Jie Qiu, Lei Cao, and Jinsong Huang. Electron-hole diffusion lengths> 175 μm in solution-grown ch3nh3pbi3 single crystals. *Science*, 347(6225):967–970, 2015.

[56] Junyu Li, Yu Gu, Zeyao Han, Jiaxin Liu, Yousheng Zou, and Xiaobao Xu. Further advancement of perovskite single crystals. *The Journal of Physical Chemistry Letters*, 13(1):274–290, 2022.

[57] Dong Shi, Valerio Adinolfi, Riccardo Comin, Mingjian Yuan, Erkki Alarousu, Andrei Buin, Yin Chen, Sjoerd Hoogland, Alexander Rothenberger, Khabiboulakh Katsiev, et al. Low trap-state density and long carrier diffusion in organolead trihalide perovskite single crystals. *Science*, 347(6221):519–522, 2015.

[58] Zhipeng Lian, Qingfeng Yan, Qianrui Lv, Ying Wang, Lili Liu, Lijing Zhang, Shilie Pan, Qiang Li, Liduo Wang, and Jia-Lin Sun. High-performance planar-type photodetector on (100) facet of mapbi3 single crystal. *Scientific reports*, 5(1):1–10, 2015.

[59] Yangyang Dang, Yian Zhou, Xiaolong Liu, Dianxing Ju, Shengqing Xia, Haibing Xia, and Xutang Tao. Formation of hybrid perovskite tin iodide single crystals by top-seeded solution growth. *Angewandte Chemie International Edition*, 55(10):3447–3450, 2016.

[60] Otakar Sohnel, Petr Novotny, and Zdenek Solc. Densities of aqueous solutions of 18 inorganic substances. *Journal of Chemical and Engineering Data*, 29(4):379–382, 1984.

[61] Makhsud I Saidaminov, Ahmed L Abdelhady, Banavoth Murali, Erkki Alarousu, Victor M Burlakov, Wei Peng, Ibrahim Dursun, Lingfei Wang, Yao He, Giacomo Maculan, et al. High-quality bulk hybrid perovskite single crystals within minutes by inverse temperature crystallization. *Nature communications*, 6(1):1–6, 2015.

[62] Wen-Guang Li, Hua-Shang Rao, Bai-Xue Chen, Xu-Dong Wang, and Dai-Bin Kuang. A formamidinium–methylammonium lead iodide perovskite single crystal exhibiting exceptional optoelectronic properties and long-term stability. *Journal of Materials Chemistry A*, 5(36):19431–19438, 2017.

[63] Xin Wang, Yin Huang, Wei Lei, Qing Li, Xiaobing Zhang, Qasim Khan, and Baoping Wang. Asymmetrical photodetection response of methylammonium lead bromide perovskite single crystal. *Crystal Research and Technology*, 52(9):1700115, 2017.

[64] Shan-Shan Rong, M Bilal Faheem, and Yan-Bo Li. Perovskite single crystals: Synthesis, properties, and applications. *Journal of Electronic Science and Technology*, 19(2):100081, 2021.

[65] Yubin Fan, Yuhan Wang, Nan Zhang, Wenzhao Sun, Yisheng Gao, Cheng-Wei Qiu, Qinghai Song, and Shumin Xiao. Resonance-enhanced three-photon luminesce via lead halide perovskite metasurfaces for optical encoding. *Nature communications*, 10(1):1–8, 2019.

[66] Isaac Suárez, Marta Vallés-Pelarda, Andrés F Gualdrón-Reyes, Iván Mora-Seró, Albert Ferrando, Humberto Michinel, José Ramón Salgueiro, and Juan P Martínez Pastor. Outstanding nonlinear optical properties of methylammonium-and cs-pbx3 (x= br, i, and br–i) perovskites: Polycrystalline thin films and nanoparticles. *APL Materials*, 7(4):041106, 2019.

[67] Fabio Luiz Sant'Anna Cuppo, Antonio Martins Figueiredo Neto, Sergio Leonardo Gómez, and Peter Palffy-Muhoray. Thermal-lens model compared with the sheik-bahae formalism in interpreting z-scan experiments on lyotropic liquid crystals. *JOSA B*, 19(6):1342–1348, 2002.

[68] Rui Zhang, Jiandong Fan, Xing Zhang, Haohai Yu, Huaijin Zhang, Yaohua Mai, Tianxiang Xu, Jiyang Wang, and Henry J Snaith. Nonlinear optical response of organic–inorganic halide perovskites. *ACS Photonics*, 3(3):371–377, 2016.

[69] Basanth S Kalanoor, Laxman Gouda, Ronen Gottesman, Shay Tirosh, Eynav Haltzi, Arie Zaban, and Yaakov R Tischler. Third-order optical nonlinearities in organometallic methylammonium lead iodide perovskite thin films. *Acs Photonics*, 3(3):361–370, 2016.

[70] Rashid A Ganeev, Konda Srinivasa Rao, Zhi Yu, Weili Yu, Chaonan Yao, Yue Fu, Ke Zhang, and Chunlei Guo. Strong nonlinear absorption in perovskite films. *Optical Materials Express*, 8(6):1472–1483, 2018.

[71] Weiwei Liu, Jun Xing, Jiaxin Zhao, Xinglin Wen, Kai Wang, Peixiang Lu, and Qihua Xiong. Giant two-photon absorption and its saturation in 2d organic–inorganic perovskite. *Advanced optical materials*, 5(7):1601045, 2017.

[72] Zimu Wei, Dengyang Guo, Jos Thieme, Claudine Katan, Valentina M Caselli, Jacky Even, and Tom J Savenije. The importance of relativistic effects on two-photon absorption spectra in metal halide perovskites. *Nature communications*, 10(1):1–8, 2019.

[73] Jun Yi, Lili Miao, Jie Li, Wei Hu, Chujun Zhao, and Shuangchun Wen. Third-order nonlinear optical response of ch 3 nh 3 pbi 3 perovskite in the mid-infrared regime. *Optical Materials Express*, 7(11):3894–3901, 2017.

[74] Pengfei Li, Yao Chen, Tieshan Yang, Ziyu Wang, Han Lin, Yanhua Xu, Lei Li, Haoran Mu, Bannur Nanjunda Shivananju, Yupeng Zhang, et al. Two-dimensional ch3nh3pbi3 perovskite nanosheets for ultrafast pulsed fiber lasers. *ACS applied materials & interfaces*, 9(14):12759–12765, 2017.

[75] Janusz Szeremeta, Magda A Antoniak, Dominika Wawrzyńczyk, Marcin Nyk, and Marek Samoć. The two-photon absorption cross-section studies of cspbx3 (x= i, br, cl) nanocrystals. *Nanomaterials*, 10(6):1054, 2020.

[76] Sijin Liu, Guixiang Chen, Yunyun Huang, Sai Lin, Yijun Zhang, Meiling He, Weidong Xiang, and Xiaojuan Liang. Tunable fluorescence and optical nonlinearities of all inorganic colloidal cesium lead halide perovskite nanocrystals. *Journal of Alloys and Compounds*, 724:889–896, 2017.

[77] Qiuju Han, Wenzhi Wu, Weilong Liu, Qingxin Yang, and Yanqiang Yang. Two-photon absorption and upconversion luminescence of colloidal cspbx3 quantum dots. *Optical Materials*, 75:880–886, 2018.

[78] Lan Yang, Ke Wei, Zhongjie Xu, Feiming Li, Runze Chen, Xin Zheng, Xiangai Cheng, and Tian Jiang. Nonlinear absorption and temperature-dependent fluorescence of perovskite fapbbr 3 nanocrystal. *Optics Letters*, 43(1):122–125, 2018.

[79] Wei-Yun Liang, Fangzhou Liu, Yu-Jung Lu, Jasminka Popović, Aleksandra Djurišić, and Hyeyoung Ahn. High optical nonlinearity in low-dimensional halide perovskite polycrystalline films. *Optics Express*, 28(17):24919–24927, 2020.

[80] S Mirershadi, Sohrab Ahmadi-Kandjani, Anna Zawadzka, H Rouhbakhsh, and Bouchta Sahraoui. Third order nonlinear optical properties of organometal halide perovskite by means of the z-scan technique. *Chemical Physics Letters*, 647:7–13, 2016.

[81] Justin C Johnson, Zhen Li, Paul F Ndione, and Kai Zhu. Third-order nonlinear optical properties of methylammonium lead halide perovskite films. *Journal of Materials Chemistry C*, 4(22):4847–4852, 2016.

[82] Wen-Gao Lu, Cheng Chen, Dengbao Han, Linhua Yao, Junbo Han, Haizheng Zhong, and Yongtian Wang. Nonlinear optical properties of colloidal ch3nh3pbbr3 and cspbbr3 quantum dots: A comparison study using z-scan technique. *Advanced Optical Materials*, 4(11):1732–1737, 2016.

[83] Felix Ochieng Saouma, Dae Young Park, Sung Hyuk Kim, Mun Seok Jeong, and Joon Ik Jang. Multiphoton absorption coefficients of organic–inorganic lead halide perovskites ch3nh3pbx3 (x= cl, br, i) single crystals. *Chemistry of Materials*, 29(16):6876–6882, 2017.

[84] Qi Wei, Bin Du, Bo Wu, Jia Guo, Ming jie Li, Jianhui Fu, Zhipeng Zhang, Jianwei Yu, Tianyu Hou, Guichuan Xing, et al. Two-photon optical properties in individual organic–inorganic perovskite microplates. *Advanced Optical Materials*, 5(24):1700809, 2017.

[85] Aamir Mushtaq, Dushyant Kushavah, Supriya Ghosh, and Suman Kalyan Pal. Nonlinear optical properties of benzylamine lead (ii) bromide perovskite microdisks in femtosecond regime. *Applied Physics Letters*, 114(5):051902, 2019.

[86] Yuhang He, Rui Su, Yuanyuan Huang, Yixuan Zhou, Qiyi Zhao, Jacob B Khurgin, Qihua Xiong, and Xinlong Xu. High-order shift current induced terahertz emission from inorganic cesium bromine lead perovskite engendered by two-photon absorption. *Advanced Functional Materials*, 29(40):1904694, 2019.

[87] Ke Wei, Zhongjie Xu, Runze Chen, Xin Zheng, Xiangai Cheng, and Tian Jiang. Temperature-dependent excitonic photoluminescence excited by two-photon absorption in perovskite cspbbr 3 quantum dots. *Optics letters*, 41(16):3821–3824, 2016.

[88] Yue Wang, Xiaoming Li, Xin Zhao, Lian Xiao, Haibo Zeng, and Handong Sun. Nonlinear absorption and low-threshold multiphoton pumped stimulated emission from all-inorganic perovskite nanocrystals. *Nano letters*, 16(1):448–453, 2016.

[89] Katturi Naga Krishnakanth, Sudipta Seth, Anunay Samanta, and Soma Venugopal Rao. Broadband femtosecond nonlinear optical properties of cspbbr 3 perovskite nanocrystals. *Optics Letters*, 43(3):603–606, 2018.

[90] Jingzhou Li, Hongxing Dong, Bin Xu, Saifeng Zhang, Zhiping Cai, Jun Wang, and Long Zhang. Cspbbr 3 perovskite quantum dots: saturable absorption properties and passively q-switched visible lasers. *Photonics Research*, 5(5):457–460, 2017.

[91] Zhiyuan Gu, Kaiyang Wang, Wenzhao Sun, Jiankai Li, Shuai Liu, Qinghai Song, and Shumin Xiao. Two-photon pumped ch3nh3pbbr3 perovskite microwire lasers. *Advanced Optical Materials*, 4(3):472–479, 2016.

[92] Zhengzheng Liu, Zhiping Hu, Zeyu Zhang, Juan Du, Jie Yang, Xiaosheng Tang, Weimin Liu, and Yuxin Leng. Two-photon pumped amplified spontaneous emission and lasing from formamidinium lead bromine nanocrystals. *Acs Photonics*, 6(12):3150–3158, 2019.

[93] Andrea Rubino, Tahiyat Huq, Jakub Dranczewski, Gabriel Lozano, Mauricio E Calvo, Stefano Vezzoli, Hernán Míguez, and Riccardo Sapienza. Efficient third harmonic generation from fapbbr 3 perovskite nanocrystals. *Journal of Materials Chemistry C*, 8(45):15990–15995, 2020.

[94] Chenjing Quan, Xiao Xing, Sihao Huang, Mengfeifei Jin, Tongchao Shi, Zeyu Zhang, Weidong Xiang, Zhanshan Wang, and Yuxin Leng. Nonlinear optical properties of cspbcl x br 3-x nanocrystals embedded glass. *Photonics Research*, 9(9):1767–1774, 2021.

[95] Junzi Li, Can Ren, Xin Qiu, Xiaodong Lin, Rui Chen, Cheng Yin, and Tingchao He. Ultrafast optical nonlinearity of blue-emitting perovskite nanocrystals. *Photonics Research*, 6(6):554–559, 2018.

[96] Kazuhiko Ogusu and Kenta Shinkawa. Optical nonlinearities in silicon for pulse durations of the order of nanoseconds at 1.06 μm. *Optics Express*, 16(19):14780–14791, 2008.

[97] Colin A Bremner, Michael Simpson, and William TA Harrison. New molecular perovskites: cubic c4n2h12 nh4cl3 h2o and 2-h hexagonal c6n2h14 nh4cl3. *Journal of the American Chemical Society*, 124(37):10960–10961, 2002.

[98] Heng-Yun Ye, Yuan-Yuan Tang, Peng-Fei Li, Wei-Qiang Liao, Ji-Xing Gao, Xiu-Ni Hua, Hu Cai, Ping-Ping Shi, Yu-Meng You, and Ren-Gen Xiong. Metal-free three-dimensional perovskite ferroelectrics. *Science*, 361(6398):151–155, 2018.

[99] Yuen-Ron Shen. Principles of nonlinear optics. 1984.

[100] E Cumberbatch. Self-focusing in non-linear optics. *IMA Journal of Applied Mathematics*, 6(3):250–262, 1970.

[101] MR Rashidian Vaziri. Comment on "nonlinear refraction measurements of materials using the moiré deflectometry". *Optics Communications*, 357:200–201, 2015.

[102] Maria Göppert-Mayer. Über elementarakte mit zwei quantensprüngen. *Annalen der Physik*, 401(3):273–294, 1931.

[103] Richard L Sutherland. *Handbook of nonlinear optics*. CRC press, 2003.

[104] Cid B De Araújo, Anderson SL Gomes, and Georges Boudebs. Techniques for nonlinear optical characterization of materials: a review. *Reports on progress in physics*, 79(3):036401, 2016.

[105] Robert W Boyd. *Nonlinear optics*. Academic press, 2020.

[106] Marc Levenson. *Introduction to nonlinear laser spectroscopy 2e*. Elsevier, 2012.

[107] DS Chemla. Non-linear optical properties of condensed matter. *Reports on Progress in Physics*, 43(10):1191, 1980.

[108] RK Jain and MB Klein. Degenerate four-wave mixing near the band gap of semiconductors. *Applied Physics Letters*, 35(6):454–456, 1979.

[109] Yanpeng Zhang and Min Xiao. *Multi-wave mixing processes*. Springer, 2009.

[110] RK Jain. Degenerate four-wave mixing in semiconductors: application to phase conjugation and to picosecond-resolved studies of transient carrier dynamics. *Optical Engineering*, 21(2):212199, 1982.

[111] Govind P Agrawal. Population pulsations and nondegenerate four-wave mixing in semiconductor lasers and amplifiers. *JOSA B*, 5(1):147–159, 1988.

[112] J Ballato, T Hawkins, P Foy, R Stolen, B Kokuoz, M Ellison, C McMillen, J Reppert, AM Rao, M Daw, et al. Silicon optical fiber. *Optics express*, 16(23):18675–18683, 2008.

[113] Pier JA Sazio, Adrian Amezcua-Correa, Chris E Finlayson, John R Hayes, Thomas J Scheidemantel, Neil F Baril, Bryan R Jackson, Dong-Jin Won, Feng Zhang, Elena R Margine, et al. Microstructured optical fibers as high-pressure microfluidic reactors. *Science*, 311(5767):1583–1586, 2006.

[114] John Ballato, Thomas Hawkins, Paul Foy, Colin McMillen, Laura Burka, Jason Reppert, Ramakrishna Podila, AM Rao, and Robert R Rice. Binary iii-v semiconductor core optical fiber. *Optics express*, 18(5):4972–4979, 2010.

[115] Justin R Sparks, Rongrui He, Noel Healy, Mahesh Krishnamurthi, Anna C Peacock, Pier JA Sazio, Venkatraman Gopalan, and John V Badding. Zinc selenide optical fibers. *Advanced Materials*, 23(14):1647–1651, 2011.

[116] Christian Wehrenfennig, Giles E Eperon, Michael B Johnston, Henry J Snaith, and Laura M Herz. High charge carrier mobilities and lifetimes in organolead trihalide perovskites. *Advanced materials*, 26(10):1584–1589, 2014.

[117] Dong Yang, Ruixia Yang, Kai Wang, Congcong Wu, Xuejie Zhu, Jiangshan Feng, Xiaodong Ren, Guojia Fang, Shashank Priya, and Shengzhong Frank Liu. High efficiency planar-type perovskite solar cells with negligible hysteresis using edta-complexed sno 2. *Nature communications*, 9(1):1–11, 2018.

[118] Frank Czerwinski. Thermal stability of aluminum alloys. *Materials*, 13(15):3441, 2020.

[119] Peter Eaton and Paul West. *Atomic force microscopy*. Oxford university press, 2010.

[120] Kishan K Sinha. Artifacts in afm, 2009.

[121] J Tauc, Radu Grigorovici, and Anina Vancu. Optical properties and electronic structure of amorphous germanium. *Physica status solidi (b)*, 15(2):627–637, 1966.

[122] EA Davis and NFf Mott. Conduction in non-crystalline systems v. conductivity, optical absorption and photoconductivity in amorphous semiconductors. *Philosophical magazine*, 22(179):0903–0922, 1970.

[123] PAUL Kubelka and F Munk. A contribution to the optics of pigments. *Z. Tech. Phys*, 12(593):193, 1931.

[124] Rosendo López and Ricardo Gómez. Band-gap energy estimation from diffuse reflectance measurements on sol–gel and commercial tio2: a comparative study. *Journal of sol-gel science and technology*, 61(1):1–7, 2012.

[125] Sébastien Josset, Olivier Muller, Loïc Schmidlin, Vincent Pichot, and Denis Spitzer. Nonlinear optical properties of detonation nanodiamond in the near infrared: Effects of concentration and size distribution. *Diamond and related materials*, 32:66–71, 2013.

[126] Mansoor Sheik-Bahae, Ali A Said, T-H Wei, David J Hagan, and Eric W Van Stryland. Sensitive measurement of optical nonlinearities using a single beam. *IEEE journal of quantum electronics*, 26(4):760–769, 1990.

[127] David Milam. Review and assessment of measured values of the nonlinear refractive-index coefficient of fused silica. *Applied optics*, 37(3):546–550, 1998.

[128] Govind P Agrawal. Induced focusing of optical beams in self-defocusing nonlinear media. *Physical review letters*, 64(21):2487, 1990.

[129] J Miguel Hickmann, ASL Gomes, and Cid B de Araújo. Observation of spatial cross-phase modulation effects in a self-defocusing nonlinear medium. *Physical review letters*, 68(24):3547, 1992.

[130] DV Petrov, ASL Gomes, and Cid B de Araújo. Reflection of a gaussian beam from a saturable absorber. *Optics communications*, 123(4-6):637–641, 1996.

[131] Gerardo Gordillo, Oscar G Torres, Maria Camila Abella, Julian C Peña, and Ophyr Virguez. Improving the stability of mapbi3 films by using a new synthesis route. *Journal of materials research and technology*, 9(6):13759–13769, 2020.

[132] AK Al-Mousoi, MS Mehde, and AM Al-Gebori. Annealing temperature effects on the performance of the perovskite solar cells. In *IOP conference series: materials science and engineering*, volume 757, page 012039. IOP Publishing, 2020.

[133] OV Oyelade, OK Oyewole, YA Olanrewaju, R Ichwani, R Koech, DO Oyewole, SA Adeniji, DM Sanni, J Cromwell, RA Ahmed, et al. Understanding the effects of annealing temperature on the mechanical properties of layers in fai-rich perovskite solar cells. *AIP Advances*, 12(2):025104, 2022.

[134] Wenshen Song, Guang-Yu Guo, Su Huang, Lan Yang, and Li Yang. First-principles studies of second-order nonlinear optical properties of organic-inorganic hybrid halide perovskites. *Physical Review Applied*, 13(1):014052, 2020.

[135] Mihaela Dinu, Francesco Quochi, and Hugo Garcia. Third-order nonlinearities in silicon at telecom wavelengths. *Applied physics letters*, 82(18):2954–2956, 2003.

[136] Alan D Bristow, Nir Rotenberg, and Henry M Van Driel. Two-photon absorption and kerr coefficients of silicon for 850–2200 nm. *Applied Physics Letters*, 90(19):191104, 2007.

[137] Ting Wang, Xin Gai, Wenhou Wei, Rongping Wang, Zhiyong Yang, Xiang Shen, Steve Madden, and Barry Luther-Davies. Systematic z-scan measurements of the third order nonlinearity of chalcogenide glasses. *Optical Materials Express*, 4(5):1011–1022, 2014.

[138] Albert Ferrando, Juan P Martinez Pastor, and Isaac Suarez. Toward metal halide perovskite nonlinear photonics. *The journal of physical chemistry letters*, 9(18):5612–5623, 2018.

[139] Marco Caputo, Nicola Cefarin, Andrea Radivo, Nicola Demitri, Lara Gigli, Jasper R Plaisier, Mirco Panighel, Giovanni Di Santo, Sacha Moretti, Angelo Giglia, et al. Electronic structure of mapbi3 and mapbcl3: Importance of band alignment. *Scientific reports*, 9(1):1–11, 2019.

[140] Dumitru Sirbu, Hei Chit Leo Tsui, Naseem Alsaif, Susana Iglesias-Porras, Yifeng Zhang, Ming Wang, Mingzhen Liu, Anna C Peacock, Pablo Docampo, and Noel Healy. Wide-band-gap metal-free perovskite for third-order nonlinear optics. *ACS photonics*, 8(8):2450–2458, 2021.

[141] Tiantian Zuo, Xuexia He, Peng Hu, and Hui Jiang. Organic-inorganic hybrid perovskite single crystals: Crystallization, molecular structures, and bandgap engineering. *ChemNanoMat*, 5(3):278–289, 2019.

[142] Yucheng Liu, Yunxia Zhang, Kui Zhao, Zhou Yang, Jiangshan Feng, Xu Zhang, Kang Wang, Lina Meng, Haochen Ye, Ming Liu, et al. A 1300 mm2 ultrahigh-performance digital imaging assembly using high-quality perovskite single crystals. *Advanced materials*, 30(29):1707314, 2018.

[143] Hua-Shang Rao, Bai-Xue Chen, Xu-Dong Wang, Dai-Bin Kuang, and Cheng-Yong Su. A micron-scale laminar mapbbr 3 single crystal for an efficient and stable perovskite solar cell. *Chemical Communications*, 53(37):5163–5166, 2017.

[144] Makhsud I Saidaminov, Valerio Adinolfi, Riccardo Comin, Ahmed L Abdelhady, Wei Peng, Ibrahim Dursun, Mingjian Yuan, Sjoerd Hoogland, Edward H Sargent, and Osman M Bakr. Planar-integrated single-crystalline perovskite photodetectors. *Nature communications*, 6(1):1–7, 2015.

[145] Haiming Zhu, Yongping Fu, Fei Meng, Xiaoxi Wu, Zizhou Gong, Qi Ding, Martin V Gustafsson, M Tuan Trinh, Song Jin, and XY Zhu. Lead halide perovskite nanowire lasers with low lasing thresholds and high quality factors. *Nature materials*, 14(6):636–642, 2015.

[146] Sjoerd A Veldhuis, Pablo P Boix, Natalia Yantara, Mingjie Li, Tze Chien Sum, Nripan Mathews, and Subodh G Mhaisalkar. Perovskite materials for light-emitting diodes and lasers. *Advanced materials*, 28(32):6804–6834, 2016.

[147] Yasuhiro Yamada, Takumi Yamada, Le Quang Phuong, Naoki Maruyama, Hidetaka Nishimura, Atsushi Wakamiya, Yasujiro Murata, and Yoshihiko Kanemitsu. Dynamic optical properties of ch3nh3pbi3 single crystals as revealed by one-and two-photon excited photoluminescence measurements. *Journal of the American Chemical Society*, 137(33):10456–10459, 2015.

[148] Daniel Niesner, Max Wilhelm, Ievgen Levchuk, Andres Osvet, Shreetu Shrestha, Miroslaw Batentschuk, Christoph Brabec, and Thomas Fauster. Giant rashba splitting in ch 3 nh 3 pbbr 3 organic-inorganic perovskite. *Physical review letters*, 117(12):126401, 2016.

[149] Michael A Becker, Roman Vaxenburg, Georgian Nedelcu, Peter C Sercel, Andrew Shabaev, Michael J Mehl, John G Michopoulos, Samuel G Lambrakos, Noam Bernstein, John L Lyons, et al. Bright triplet excitons in caesium lead halide perovskites. *Nature*, 553(7687):189–193, 2018.

[150] Hao-Ping Hsu, Liang-Chen Li, Muthaiah Shellaiah, and Kien Wen Sun. Structural, photophysical, and electronic properties of ch3nh3pbcl3 single crystals. *Scientific reports*, 9(1):1–14, 2019.

[151] Yucheng Liu, Yunxia Zhang, Zhou Yang, Dong Yang, Xiaodong Ren, Liuqing Pang, and Shengzhong Liu. Thinness-and shape-controlled growth for ultrathin single-crystalline perovskite wafers for mass production of superior photoelectronic devices. *Advanced materials*, 28(41):9204–9209, 2016.

[152] Christian Kriso, Markus Stein, Tobias Haeger, Neda Pourdavoud, Marina Gerhard, Arash Rahimi-Iman, Thomas Riedl, and Martin Koch. Nonlinear refraction in ch 3 nh 3 pbbr 3 single crystals. *Optics letters*, 45(8):2431–2434, 2020.

[153] Grant Walters, Brandon R Sutherland, Sjoerd Hoogland, Dong Shi, Riccardo Comin, Daniel P Sellan, Osman M Bakr, and Edward H Sargent. Two-photon absorption in organometallic bromide perovskites. *ACS nano*, 9(9):9340–9346, 2015.

[154] Tzu-Chiao Wei, Sudha Mokkapati, Ting-You Li, Chun-Ho Lin, Gong-Ru Lin, Chennupati Jagadish, and Jr-Hau He. Nonlinear absorption applications of ch3nh3pbbr3 perovskite crystals. *Advanced Functional Materials*, 28(18):1707175, 2018.

[155] Aleksey Vasilev, Todor Deligeorgiev, Nikolai Gadjev, and Karl-Heinz Drexhage. Synthesis of novel monomeric and homodimeric cyanine dyes based on oxazolo[4,5-b]pyridinium and quinolinium end groups for nucleic acid detection. *Dyes and Pigments*, 66(2):135–142, 2005.

[156] Atanas Kurutos, Iva Orehovec, Dijana Saftić, Lucija Horvat, Ivo Crnolatac, Ivo Piantanida, and Todor Deligeorgiev. Cell penetrating, mitochondria targeting multiply charged dabco-cyanine dyes. *Dyes and Pigments*, 158:517–525, 2018.

[157] Mingzhen Liu, Michael B Johnston, and Henry J Snaith. Efficient planar heterojunction perovskite solar cells by vapour deposition. *Nature*, 501(7467):395–398, 2013.

[158] Ashish Dubey, Nirmal Adhikari, Sally Mabrouk, Fan Wu, Ke Chen, Shangfeng Yang, and Qiquan Qiao. A strategic review on processing routes towards highly efficient perovskite solar cells. *Journal of Materials Chemistry A*, 6(6):2406–2431, 2018.

[159] Ranjith Kottokkaran, Harshavardhan A. Gaonkar, Hisham A. Abbas, Max Noack, and Vikram Dalal. Performance and stability of co-evaporated vapor deposited perovskite solar cells. *Journal of Materials Science: Materials in Electronics*, 30(6):5487–5494, Mar 2019.

[160] Kilian B. Lohmann, Jay B. Patel, Mathias Uller Rothmann, Chelsea Q. Xia, Robert D. J. Oliver, Laura M. Herz, Henry J. Snaith, and Michael B. Johnston. Control over crystal size in vapor deposited metal-halide perovskite films. *ACS Energy Letters*, 5(3):710–717, 2020.

[161] Marcel Roß, Lidón Gil-Escrig, Amran Al-Ashouri, Philipp Tockhorn, Marko Jošt, Bernd Rech, and Steve Albrecht. Co-evaporated p-i-n perovskite solar cells beyond 20% efficiency: Impact of substrate temperature and hole-transport layer. *ACS Applied Materials & Interfaces*, 12(35):39261–39272, 2020.

[162] Xiao Chen, Yoon Myung, Arashdeep Thind, Zhengning Gao, Bo Yin, Meikun Shen, Sung Beom Cho, Peifu Cheng, Bryce Sadtler, Rohan Mishra, and Parag Banerjee. Atmospheric pressure chemical vapor deposition of methylammonium bismuth iodide thin films. *J. Mater. Chem. A*, 5:24728–24739, 2017.

[163] Camilo Otalora, Mónica A. Botero, Maria. A. Mantilla, Johann. F. Petit, Rogelio Ospina, and Gerardo Gordillo. Hybrid perovskite films deposited by thermal evaporation from a single source. *Journal of Materials Science: Materials in Electronics*, 32(9):12151–12163, May 2021.

[164] Florent Sahli, Nathanaël Miaz, Niccolò Salsi, Cédric Bucher, Aymeric Schafflützel, Quentin Guesnay, Léo Duchêne, Björn Niesen, Christophe Ballif, and Quentin Jeangros. Vapor transport deposition of methylammonium iodide for perovskite solar cells. *ACS Applied Energy Materials*, 4(5):4333–4343, 2021.

[165] Dumitru Sirbu, Hei Chit Leo Tsui, Naseem Alsaif, Susana Iglesias-Porras, Yifeng Zhang, Ming Wang, Mingzhen Liu, Anna C. Peacock, Pablo Docampo, and Noel Healy. Wide-band-gap metal-free perovskite for third-order nonlinear optics. *ACS Photonics*, 8(8):2450–2458, 2021.

[166] Wan-Ying Zhang, Yuan-Yuan Tang, Peng-Fei Li, Ping-Ping Shi, Wei-Qiang Liao, Da-Wei Fu, Heng-Yun Ye, Yi Zhang, and Ren-Gen Xiong. Precise molecular design of high-tc 3d organic–inorganic perovskite ferroelectric: [mehdabco]rbi3 (mehdabco = n-methyl-1,4-diazoniabicyclo[2.2.2]octane). *Journal of the American Chemical Society*, 139(31):10897–10902, 2017.

[167] Govind P Agrawal. *Fiber-optic communication systems*, volume 222. John Wiley & Sons, 2012.

[168] L Wetenkamp, GF West, and H Többen. Optical properties of rare earth-doped zblan glasses. *Journal of non-crystalline solids*, 140:35–40, 1992.

[169] Jas S Sanghera, L Brandon Shaw, and Ishwar D Aggarwal. Chalcogenide glass-fiber-based mid-ir sources and applications. *IEEE Journal of selected topics in quantum electronics*, 15(1):114–119, 2009.

[170] Benjamin J Eggleton, Barry Luther-Davies, and Kathleen Richardson. Chalcogenide photonics. *Nature photonics*, 5(3):141–148, 2011.

[171] Nadia Giovanna Boetti, Diego Pugliese, Edoardo Ceci-Ginistrelli, Joris Lousteau, Davide Janner, and Daniel Milanese. Highly doped phosphate glass fibers for compact lasers and amplifiers: a review. *Applied Sciences*, 7(12):1295, 2017.

[172] Xiushan Zhu and N Peyghambarian. High-power zblan glass fiber lasers: review and prospect. *Advances in OptoElectronics*, 2010, 2010.

[173] Laurent Calvez. Chalcogenide glasses and glass-ceramics: Transparent materials in the infrared for dual applications. *Comptes Rendus Physique*, 18(5-6):314–322, 2017.

[174] Fuxi Gan. Optical properties of fluoride glasses: a review. *Journal of non-crystalline solids*, 184:9–20, 1995.

[175] Mehmet Bayindir, Fabien Sorin, Ayman F Abouraddy, Jeff Viens, Shandon D Hart, John D Joannopoulos, and Yoel Fink. Metal–insulator–semiconductor optoelectronic fibres. *Nature*, 431(7010):826–829, 2004.

[176] Brian L Scott, Ke Wang, Vincent Caluori, and Gary Pickrell. Fabrication of silicon optical fiber. *Optical Engineering*, 48(10):100501, 2009.

[177] BE Yoldas and TW O'Keeffe. Antireflective coatings applied from metal–organic derived liquid precursors. *Applied Optics*, 18(18):3133–3138, 1979.

[178] Richard Soref. The past, present, and future of silicon photonics. *IEEE Journal of selected topics in quantum electronics*, 12(6):1678–1687, 2006.

[179] HK Tsang and Y Liu. Nonlinear optical properties of silicon waveguides. *Semiconductor Science and Technology*, 23(6):064007, 2008.

[180] P Mehta, N Healy, TD Day, JR Sparks, PJA Sazio, JV Badding, and AC Peacock. All-optical modulation using two-photon absorption in silicon core optical fibers. *Optics express*, 19(20):19078–19083, 2011.

[181] L Shen, N Healy, L Xu, HY Cheng, TD Day, JHV Price, JV Badding, and AC Peacock. Four-wave mixing and octave-spanning supercontinuum generation in a small core hydrogenated amorphous silicon fiber pumped in the mid-infrared. *Optics Letters*, 39(19):5721–5724, 2014.

[182] Dong Wu, Li Shen, Haonan Ren, Joseph Campling, Thomas W Hawkins, John Ballato, Ursula J Gibson, and Anna C Peacock. Net optical parametric gain in a submicron silicon core fiber pumped in the telecom band. *APL Photonics*, 4(8):086102, 2019.

[183] Jeremy J Low, Michael L Kreider, Drew P Pulsifer, Andrew S Jones, and Tariq H Gilani. Band gap energy in silicon. *American Journal of Undergraduate Research*, 7(1):27–32, 2008.

[184] Xin Song, Qian Li, Jiang Han, Chuang Ma, Zhuo Xu, Haojin Li, Peijun Wang, Zhou Yang, Qingyue Cui, Lili Gao, et al. Highly luminescent metal-free perovskite single crystal for biocompatible x-ray detector to attain highest sensitivity. *Advanced Materials*, 33(36):2102190, 2021.

[185] Michael G Ehrenreich, Zhixin Zeng, Stefan Burger, Mark R Warren, Michael W Gaultois, Jin-Chong Tan, and Gregor Kieslich. Mechanical properties of the ferroelectric metal-free perovskite [mdabco](nh 4) i 3. *Chemical Communications*, 55(27):3911–3914, 2019.

[186] Subhasis Chaudhuri, Justin R Sparks, Xiaoyu Ji, Mahesh Krishnamurthi, Li Shen, Noel Healy, Anna C Peacock, Venkatraman Gopalan, and John V Badding. Crystalline silicon optical fibers with low optical loss. *ACS Photonics*, 3(3):378–384, 2016.

[187] Yongfeng Zhou, Michael A Parkes, Jinshuai Zhang, Yufei Wang, Michael Ruddlesden, Helen H Fielding, and Lei Su. Single-crystal organometallic perovskite optical fibers. *Science Advances*, 8(38):eabq8629, 2022.